STRUCTURAL HEALTH MONITORING OF THE TRAFFIC BRIDGE IN SASKATOON USING STRAIN GAUGES

A Thesis

Submitted to the College of Graduate Studies and Research

In Partial Fulfillment of the Requirements

for the

Masters of Science in Engineering

in the

Department of Civil and Geological Engineering

University of Saskatchewan

Saskatoon, SK

By

Alison B. MacLeod

PERMISSION TO USE

The author has agreed that the library, University of Saskatchewan, may make this thesis freely available for inspection. Permission for extensive copying of this thesis for scholarly purposes is permitted by the author, and may be granted by the professors who supervised the thesis work recorded herein or, in their absence, by the head of the Department or the Dean of the College of Engineering. It is understood that due recognition must be given to the author and to the University of Saskatchewan for any use of the material in this thesis. Copying or publication or any other use of the thesis for financial gain without approval by the University of Saskatchewan and the author's written permission is prohibited.

Requests for permission to copy or make any other use of material in this thesis in whole or part should be addressed to:

Head of Department of Civil & Geological Engineering
University of Saskatchewan
Engineering Building
57 Campus Drive
Saskatoon, Saskatchewan
Canada, S7N 5A9

ABSTRACT

The steel through-truss Traffic Bridge, located in Saskatoon, Saskatchewan is over one hundred years old. The bridge has been subject to ongoing maintenance throughout its service life. However, inspection reports from 2005 and 2006 highlighted the severe deterioration experienced primarily by the steel members immediately above and below the deck surface. These reports prompted the City of Saskatoon (COS) to implement a rehabilitation project that involved the installation of a post-tensioning system to relieve the badly corroded bottom chord members of the axial loads due to the self-weight of the structure, in 2006. Due to the severe deterioration and the structural modifications that the Traffic Bridge has endured, a limited scope structural health monitoring (SHM) system, based on strain measurements, was implemented to reduce some of the uncertainty regarding the active load paths occurring at the deck level.

The objectives of the SHM study were to obtain more information regarding the actual load paths and ascertain possible types of structural redundancy, to determine how to best model this type of structure, and to find ways to track ongoing deterioration using instrumentation. The SHM study involved controlled truck loading scenarios to permit measurement of the load paths and provide data to compare the measured results to a finite element (FE) model of the instrumented span. In addition, random loading scenarios were used to capture the vertical dynamic response of the structure in order to further refine the FE model.

This study focused on the response of one-half of one interior span. A total of 72 strain gauges were installed. The downstream truss was highly instrumented at ten locations, three members of the upstream truss were instrumented to measure the distribution, and the floor joists in the downstream lane were instrumented to establish possible redundancy paths.

Using an FE model in combination with the measured strain data, it was found that redundant load paths only existed at the level of the deck. The bottom chord members experienced non-zero strains once the control vehicle was past the span, possibly indicating some level of redundancy. The members believed to relieve a portion of the bottom chord tensile forces included the car joists, edge joists, and the timber deck. The

amount of force transferred from the bottom chord to the deck members was found by FE analysis to be highly related to the lateral stiffness of the floor beams.

The FE model was adjusted to match the measured results by modifying various modelling parameters. The most important features of the model were that all deck elements were modelled to be located at the elevation of the bottom chord, that the lateral stiffness of the floor beams was reduced by 50% to best represent the transfer of forces to deck elements, and that the stiffness of bottom chord members was reduced to 80% of their pristine values. In combination with calibrated modification factors applied to the measured values, this FE model is believed to be a useful tool to represent the behaviour of the structure to assist in detecting further damage by modelling the strain differential between members, and components of members.

ACKNOWLEDGEMENTS

I would like to express my gratitude to my supervisors: Dr. Bruce Sparling and Dr. Leon Wegner. Together, they have been supportive throughout the duration of my studies. Their extensive knowledge and expertise has provided me with exceptional guidance, criticism, and encouragement.

My advisory committee: Dr. Lisa Feldman and Dr. Mohamed Boulfiza have provided tremendous support, advice and encouragement throughout the duration of my enrolment as a graduate student. I would like to also thank Mr. Brennan Pokoyway and Mr. Dale Pavier for providing skilled assistance and technical support during the instrumentation and monitoring program.

Financially, I would like to thank the National Research Council of Canada's Discovery Grant program and the University of Saskatchewan's Department of Civil and Geological Engineering. Also, I would like to thank the City of Saskatoon for providing financial support and assistance coordinating equipment required and the bridge closures.

Last but not least, I would like to thank my family: Robert MacLeod, Peggy MacLeod, Trenna MacLeod, Chris Pemberton, Colin MacLeod, Naomie MacLeod, Liam MacLeod and Kate MacLeod; for providing continual support and encouragement.

TABLE OF CONTENTS

LIST OF TABLES

LIST OF FIGURES

NOMENCLATURE

A	Member cross-sectional area
A_n	Nominal cross-sectional area
E	Modulus of elasticity
f_{cut}	Cut-off frequency
f_{lp}	Low-pass filtering frequency
f_{Ny}	Nyquist frequency
f_s	Sampling frequency
F_{FE}	Modelled axial force
F_{member}	Member axial force
$F_{m,M}$	Measured axial force
FD	Force distribution
I	Moment of inertia
MF	Modification factor
P	Member axial force
$PT_{reduction}$	Post-tensioning axial force reduction factor
r	User-specified sampling frequency modification factor
T_{MG}	Total axial force carried by deck member groups
T_T	Total axial force carried by all deck member groups
Wn	Normalized butterworth cutoff frequency
y_i	Distance from centroid for the i^{th} strain gauge
δt	Sampling interval
ε_{avg}	Average measured strain
ε_i	Measured strain for the i^{th} strain gauge
ε_m	Measured strain
ϕ	Modelled mode shape vector
ϕ^*	Complex conjugate of modelled mode shape vector
λ_{eI}	Normalized instantaneous strain
σ_i	Stress at the i^{th} strain gauge

LIST OF ABREVIATIONS

3-D	Three-dimensional
AASHTO	American Association of State Highway and Transportation Officials
ARIMA	Autoregressive integrated moving average
CDM	Continuum damage mechanics
COS	City of Saskatoon
COV	Coefficient of variation
DAF	Dynamic amplification factor
DAQ	Data acquisition
DLA	Dynamic load allowance
FE	Finite element
FHA	Federal Highway Administration
ft	foot
HSS	Hollow structural steel
Hz	Hertz
IRD	International Road Dynamics
kV	kilo volt
m	meter
MAC	Modal assurance criterion
MF	Modification factor
MS50	Design load rating of 5 tonnes
MSF	Modal scale factor
Pa	Pascal
PT	Post-tensioning
rms	root-mean-square
SHM	Structural health monitoring
SSI	Stochastic subspace identification
tonne	1000 kilograms
typ.	Typical
VBDD	Vibration-based damage detection

1 INTRODUCTION

1.1 BACKGROUND

Serving as Saskatoon's first bridge open to streetcar traffic in 1907, the Traffic Bridge originally helped amalgamate the communities of Nutana, Riversdale, and Saskatoon. Seen in Figure 1.1, five independent steel trusses span the South Saskatchewan River, the middle three with 61 m (200 ft) spans, and the two approach spans of 53 m (175 ft). This heavy-class steel truss structure is supported with concrete piers, one of which endured a collision with the 'S.S. City of Medicine Hat' steamboat a year after construction. A walkway is cantilevered from the floor beams on the upstream side of the bridge, providing safe access for pedestrian and bicycle traffic. The traffic deck of the bridge is composed of timber laid on edge with an asphalt overlay, whereas the walkway deck is composed of timber planks. Figures 1.2 and 1.3 depict the horse and buggy and streetcar traffic that the bridge originally supported.

Figure 1.1. Opening Ceremony of the Traffic Bridge, October 7, 1907 (http://olc.spsd.sk.ca/DE/resources/bridges/photogal.htm).

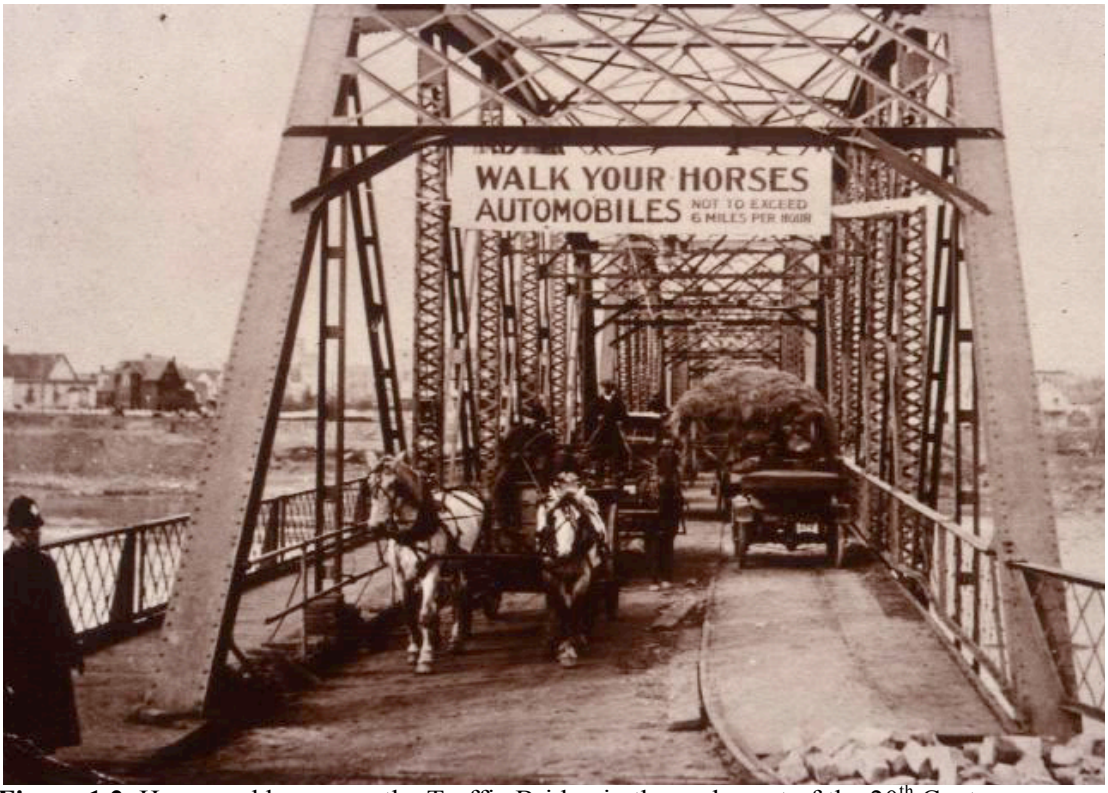

Figure 1.2. Horse and buggy on the Traffic Bridge in the early part of the 20th Century (http://olc.spsd.sk.ca/DE/resources/bridges/photogal.htm).

Figure 1.3. Streetcar on the Traffic Bridge (http://olc.spsd.sk.ca/DE/resources/bridges/photogal.htm).

Over the life of the structure, the bridge superstructure has been modified and repaired extensively. In 1986, an MS50 (5 tonne) load restriction was imposed due to the deteriorated timber deck, while the trusses were deemed adequate to sustain an MS200 design truck and lane loading. The majority of the work included regular maintenance. Some of the work completed is listed as follows (Earthtech 2003, Stantec 2005, Wardrop 2006):

- The south spans were elevated by replacing the original concrete south abutment with a steel bent (1960).
- The steel members at and below the deck level were recoated (1975/1979).
- The badly corroded exterior deck stringers were replaced and the timber deck was repaired in damaged areas (1985).
- New Hollow Structural Steel (HSS) traffic guardrails were installed, and the handrail was replaced on the walkway (1992).
- New concrete bearing pedestals, bearings, and expansion joints were installed. Repairs to damaged steel truss members were also completed (1995).
- New timber walkway planks were installed, including supporting stringers (1996).
- The approach piles were upgraded and new expansion joints installed (1996).
- A new asphalt deck surface was installed (2001).
- Truss members damaged from collision impact were repaired (2003).
- The bridge was closed due to public safety concerns after a detailed inspection was completed (2005).
- The bridge was reopened after completion of a structural rehabilitation project that included the installation of a post-tensioning system to the bottom chord members to reduce the tensile loads that the bottom chord members sustain due to dead loads (2006).

The inspection report completed in 2005 (Stantec 2005) focused on the highly deteriorated condition of the bottom chords. Local buckling failures were observed at some bottom chord members, a behaviour which is contrary to their design function as tension members. The buckling was assumed to have resulted from bearing seizure, which induced compression forces in the bottom chord members by limiting the

expansion of the steel. The estimated average section loss experienced by the bottom chords is listed in Table 1.1. These values were estimated using callipers, because more sophisticated techniques such as ultrasound have been found to be unsuccessful with heavily deteriorated members because of the presence of air voids (Stantec 2005). Figure 1.4 illustrates the typical condition of the bottom chord members. The 2005 inspection report resulted in a temporary closure of the bridge due to public safety concerns. The trusses have been numbered from the south approach span (1), in order to the north approach span (5).

Table 1.1. Estimated average section loss in bottom chord members (Stantec, 2005).

Truss	1	2	3	4	5
Upstream	47%	27%	23%	21%	13%
Downstream	41%	35%	14%	15%	20%

(a) (b)

Figure 1.4. Bottom chord member 2008 condition: (a) Span 2 downstream truss, and (b) Span 1 downstream truss joint L7, viewed from above.

The 2006 investigation report (Wardrop 2006) reinforced the findings in the 2005 report with regards to the poor condition of the bridge due to the advanced deterioration of the timber deck and steel members below 1.5 m (5 ft) above the deck. A

rehabilitation option was accepted by the City of Saskatoon for a service life extension of 20 years. This included repairing selected deficient steel truss members and connections and installing a post-tensioning system to the bottom chords in the first three spans. The purpose of the post-tensioning system was to relieve the axial tensile forces that the highly deteriorated bottom chord members experience due to self-weight. This, in effect, increased the capacity of the bottom chord members. Figure 1.5 displays the conceptual drawing of the post-tensioning system for a 53 m (175 ft) span.

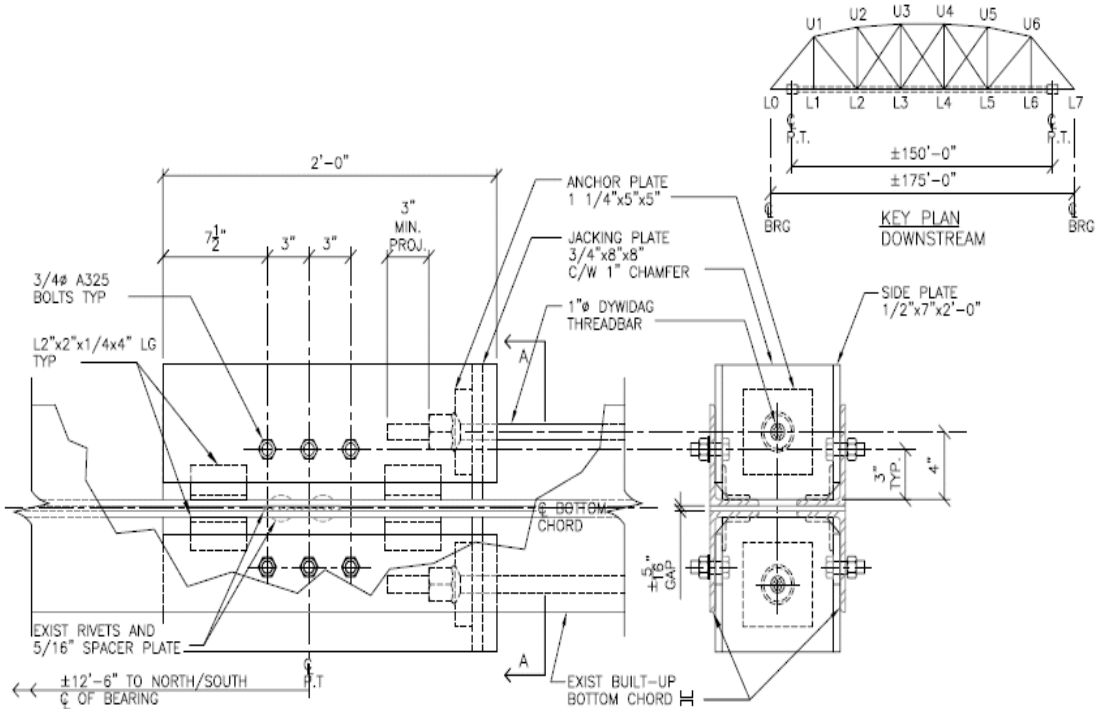

Figure 1.5. Post-tensioning system attachment to bottom chord member for 53 m (175 ft) span (Wardrop 2006).

Many uncertainties remain regarding the behaviour and condition of the century-old Traffic Bridge, particularly with respect to the load distribution at the deck level, remaining section areas, and disintegration rates. To date, all investigations have relied on visual inspections, which have been found to be highly subjective based on the experience of the inspector and subject to the accessibility of structural elements (Federal Highway Administration 2001). In addition, the structure has changed significantly from the original construction in 1907. In particular, the bearing replacement, localized buckling failure of various elements, and the addition of the post-tensioning system have all contributed to changing its structural behaviour as compared

to its original design. Heavy-class steel truss bridges have also been found to have a high level of structural redundancy due to alternate load paths at the deck level (Nagavi 2003), even though as a two-dimensional system, the truss would be statically determinate. To mitigate the risk associated with these uncertainties, particularly given the advanced state of deterioration of many of its components, a limited scope structural health monitoring (SHM) program was implemented.

1.2 OBJECTIVES

The objectives of this study were as follows:

1. to verify the actual load paths within the bridge and establish the presence of any forms of structural redundancy;
2. to assess the effects of modifying various modelling parameters in a finite element model of the bridge in order to determine appropriate modelling assumptions/techniques for this particular bridge; and
3. to investigate ways to track ongoing damage due to deterioration using structural health monitoring.

1.3 SCOPE & METHODOLOGY

The study described in this thesis consisted of a field monitoring component, in which one of the bridge trusses was monitored using strain gauges, and an analytical component, in which the behaviour of the bridge was simulated using a finite element (FE) model. The scope and methodology associated with various elements of the study are summarized in the following subsections.

1.3.1 Instrumented Members

The focus of this study was on the behaviour of one 61 m (200 ft) interior truss span. Obtaining a clear understanding of how one of the five spans responds under loading was expected to provide insight as to how to best instrument the remaining four spans if a more comprehensive SHM system was deemed feasible. To reduce the cost and quantity of instrumentation, only half of one downstream truss was heavily instrumented with strain gauges. The corresponding upstream truss was instrumented with strain gauges in only three locations to determine the three-dimensional aspects of

the response. In a supplemental investigation, the vertical acceleration response at the panel points was captured for both the downstream and upstream trusses of the span to determine the dynamic characteristics of the bridge. Further details are provided in Chapter 3.

1.3.2 Loading Scenarios

The instrumented span was subjected to controlled loading scenarios using a truck of known weight, as well as random loading due to ambient traffic, as described in detail in Chapter 3. The controlled loading scenarios were implemented to ascertain the load effects in the instrumented structural components, and to compare the resulting strain-time histories in the instrumented components to the response predicted by the FE model under similar simulated controlled loading scenarios. Controlled dynamic loading scenarios were used to capture the dynamic amplification effects. The random traffic loading scenarios were implemented to capture the acceleration response of the bridge, and to allow further refinement of the FE model.

1.3.3 Strain Measurements

To compare the measured strains to the response predicted by the FE model, and to better understand the load paths, the strains were converted to axial forces using assumed member properties. Since it was not possible to know or estimate the actual section properties with any degree of certainty, the pristine member properties were used to calculate the so-called "measured" axial forces. Although this method did not accurately capture the actual measured force, specifically for the bottom chord members that were known to feature significant deterioration, there was no way to accurately measure the cross-sectional areas of deteriorated members. Instead, the potential effect of deterioration was considered when attempting to explain comparisons between measured and calculated responses, and taken into account by using modification factors applied to the measured response.

1.3.4 Acceleration Measurements

As already mentioned, the vertical acceleration response was measured at panel points under random and controlled dynamic loading scenarios. The acceleration

measurements were not intended for use in possible damage detection methods, but only to refine the FE model by matching observed dynamic characteristics.

1.3.5 Finite Element Model

The FE model was created to investigate the structural behaviour with respect to load paths, possible redundancy, and effectiveness of the post-tensioning system. To improve the correlation between measured and FE simulated responses, various modelling parameters were modified. These modelling parameters included support conditions, member connectivity (pinned vs. fixed joints), geometric elevation of the bridge deck members relative to the bottom chord, and member properties.

1.4 THESIS LAYOUT

The layout of the thesis is as follows. Chapter 2 is a literature review, focussing on research completed to date in which strain gauges were used to monitor the behaviour of various steel bridge structures. The experimental program, including data collection and filtering methods, is described in Chapter 3. The construction of the FE model is described in Chapter 4. The results, described in detail in Chapter 5, are broken into two parts: (a) observations from the strain-time history measurements; and (b) how changes to the FE modelling parameters affected the correlation to the measured results. The findings from this study are summarized in Chapter 6.

2 LITERATURE REVIEW

2.1 INTRODUCTION

As the technology required to create durable structures is advancing, existing infrastructure is deteriorating. Structural health monitoring (SHM) is a broad area of investigation that uses instrumentation attached to a structure to confirm the structure's response under loading, identify the presence of damage, locate damage, and/or estimate the remaining service life. With the declining condition of the current infrastructure, as well as the unreliability of visual inspections (Federal Highway Administration 2001), SHM has become an important tool to assist with the assessment of existing structures and improve their reliability. Section 2.2 provides two examples of full-scale bridge tests that illustrate the need for SHM.

There are many types of instrumentation and approaches that have been used to assess the structural health of infrastructure. Accelerometers have been used to measure the natural frequencies and mode shapes of a structure for use in vibration-based damage detection (VBDD) (Doebling et al. 1998). Strain gauge data have been used to estimate the remaining life of a structure by a statistical fatigue analysis, to track load distribution changes, and to measure live load distributions. While other technologies, such as fibre optic sensors, piezoelectric sensors, temperature sensors, anemometers, weigh-in-motion devices, and displacement transducers (to name a few), have been used as part of SHM systems, the focus of this thesis is on the use of strain gauges in an SHM system. The strain-time history at various points on a structure can be used to effectively monitor the performance of a structure, and determine to what degree the members are actively resisting the applied loads. Since large amounts of data can easily be generated with strain gauges, the most critical step is to determine an efficient method to sort and apply the information. The use of strain gauges for bridge monitoring is reviewed in Section 2.3.

The literature reviewed in this chapter has been highlighted due to its relevance to this project. Most papers focus on the structural response of steel truss bridges. The first two studies described in the following section focused on destructive testing to

obtain insight into the collapse mechanisms of steel trusses. The structural response monitored using strain gauges is the focus of the remainder of the chapter, with a variety of methods of using the strain gauge data described.

2.2 FULL-SCALE BRIDGE TESTING

Full-scale testing of an old bridge can result in interesting failure mechanisms that cannot always be predicted. The highlights from two full-scale bridge tests are described in this section. These highlights include the observations noted as well as the uncertainty that remained after the tests were completed.

A decommissioned 80-year old steel truss bridge was transported to a lab and tested to measure its ultimate load and failure mode (Azizinamini 2002). The deck had been removed prior to testing, which precluded the possibility of determining whether it provided an alternate load path for the bottom chord forces. The members were not instrumented and the axial forces due to loading were obtained from a finite element (FE) analysis. The first failure occurred in a tensile-diagonal member of the bridge, and was brittle and sudden. The total applied load at failure was 2.4 times greater than the 21.4 tonne (47.2 kip) allowable load during its service life. The bridge was then retrofitted to strengthen the failed tension members, and loaded again to failure. The strengthened tension members forced the failure to occur in the top compression members at an ultimate load of 70 tonnes (154 kips), 1.36 times greater than the first load test. Also important to note from this test is that the second failure was ductile, and gave ample warning. It was concluded that, for ductile failure to occur in a 3-D, statically determinate truss, the failure must occur in the compression members and not the tension members.

Nagavi and Aktan (2003) loaded a decommissioned heavy-class steel truss bridge to failure to better understand how to create an accurate FE model of such a structure. Among the many findings, failure occurred between a deteriorated gusset-plate and the bottom chord after a seized bearing released, causing a sudden spike in axial load. The failure occurred at approximately 40% of the predicted failure load. The deteriorated connection between the gusset plate and the bottom chord member was not predicted to fail as it did.

The first study highlighted the desired failure mechanism that should be taken into consideration during design, as well as the extra capacity that was present during failure. The second study observed an unpredicted failure mechanism that occurred well below the estimated capacity. The findings from destructive testing provide excellent information that can be used for better structural design and to assess existing structures. These studies exemplify the need for damage-detection SHM systems, as structures generally may not behave as expected.

2.3 STRAIN GAUGE USE IN SHM

One major decision that must be made with the implementation of an SHM system is the type of instrumentation to be used. Each instrumentation choice has its benefits and shortfalls. The previous use of strain gauges in SHM systems is discussed in this section.

The use of strain gauges as a means to monitor the performance of structures is not new. There have been studies using strain gauges for over 90 years. However, the use of strain gauges on a highly deteriorated, statically determinate, structural system approaching the end of its service life has not met with a high success rate to measure deterioration. There have been successful studies to determine load paths and identify active structural members on aging infrastructure (O'Connell and Dexter 2001, Enevoldsen et al. 2002) using strain gauges. However, the accuracy of the actual load that each member carries is highly uncertain due to the uncertainty regarding the net remaining section of the highly deteriorated members.

The strain response has been viewed in the time domain, frequency domain, and by a peak strain histogram. The time domain can provide information related to how the instrumented structural members behave under loading, and examples are discussed in Section 2.3.1. The strain used to calculate the stress histogram of an instrumented structural element can assist in a statistical estimation of fatigue damage, and examples are discussed in Section 2.3.2. Since temperature can affect the strain measurements, examples of addressing the temperature effects are discussed in Section 2.3.3. Finally, examples of the use of an FE model to accurately represent the measured strain response are discussed in Section 2.3.4. These FE models were constructed to gain insight into the actual structural behaviour, based on the strain measurements.

2.3.1 Structural Load Path Evaluation using Strain-Time History Measurements

Strain-time histories are used in the following examples to verify load paths by focusing on certain components of the response. The time-domain is an appropriate way to observe these data, as data in this form can easily be manipulated into an influence diagram. The load distribution is of interest to observe how the structure responds to live loading scenarios, and to determine if any alternate load paths exist. The dynamic amplification factor (i.e., how much the static structural response is amplified due to vehicles travelling at speed) is used for design and assessment purposes. The following examples of steel truss bridges show that varying dynamic amplification values may be experienced.

One of the major questions related to assessing the condition or behaviour of a structure is the possibility of an alternate load path should an existing member fail, or whether the alternate load paths are currently being utilized. Nagavi and Aktan (2003) indicate that it is typical for short-span, heavy-class steel bridges to exhibit redundant behaviour even if a major member yields. This redundancy poses a challenge when attempting to create an accurate model of the structure. Deck action may contribute to resisting some of the tensile loads in the bottom chord of trusses. De Corte and Van Bogaert (2006) found that the strain signal measured for a deck member in a given span did not immediately return to zero once a vehicle was past the span. They credited this behaviour to the "orthotropic deck action," meaning that the deck was acting as a membrane to resist the tensile loads initially thought to be carried only by the bottom chord members. DelGrego et al. (2008) indicated that axial loads may not be shared between the components of laced members, and that, in reality, some members might not even be taking any anticipated loads.

O'Connell and Dexter (2001) explored the strain-time history for various members of two steel truss bridges to verify the load paths and develop an accurate model that was representative of the actual truss behaviour. The following observations are worth noting:

- The peak stress measured for a particular floor beam was not proportional to the applied load. One truck produced a floor beam peak stress of 18 MPa, while two similar trucks side-by-side produced a peak stress of 26 MPa, approximately

28% less than anticipated. This was thought to indicate the presence of alternate load paths.

- As the speed of vehicles increases, the forces carried by the structural members may increase. The amount by which the force increases with respect to the static (or crawl speed) force is known as the dynamic amplification factor or impact factor. In these tests, the dynamic amplification factor was observed to occur only in the tension chord of the truss and to have a value of 1.1.
- The top and bottom chord forces of a second bridge—the I-35W Bridge over the Mississippi River—were difficult to predict and could be modelled with some accuracy when the stress-time history results were averaged between non-composite and fully-composite action between the truss and the concrete deck.
- Pinning all supports of the model (which mimics bearing seizure) provided a more accurate stress-time history for the I-35W Bridge.

This study illustrated the importance of analyzing the strain-time history to verify load paths and bridge behaviour under live loading. Controlled load tests were found to be essential for use in combination with the strain-time histories to develop an accurate FE model to use as a baseline in the SHM process.

In another study of a steel truss bridge that was more than 100 years old, DelGrego et al. (2008) found that the structural load paths differed significantly from the distribution predicted by analytical methods. The railway bridge studied had truss members composed of smaller angles, channels, and plates laced together. The diagonal members of the bridge had a circular cross section with eye-bar ends to create near-ideal pinned connections. By measuring strains experienced by the components of the built-up diagonal members, it was found that the load distribution between the parallel components was not uniform, and that some of the component members were not, in fact, taking any live loads or were carrying only a very small portion of the live loads. This study reinforces the need to verify the live load distribution throughout the bridge structure prior to making conclusions about the bridge behaviour.

Bakht and Jaeger (1990) discussed the surprises found during the monitoring of steel truss and slab on girder bridges. It was found that, depending on the connection fixity, deck joists have the ability to sustain a portion of the bottom chord tensile loads,

proportional to the relative stiffness of the deck joists and the bottom chord. They also confirmed that the axial forces of a built-up member may not be evenly distributed among the components that make up the member. However, some of the conclusions appear to be based more on inference rather than direct measurements, and alternative interpretations of the data may be possible.

Cardini and DeWolf (2009) attempted to track the deterioration of a three span steel girder bridge using long-term strain-time history measurements and the resulting load distribution factors, peak strains and the neutral axis locations. Two strain gauges were installed at the mid-span of selected girders to capture both the bending strain distribution, which was used to calculate the neutral axis location, and peak strains, which were used for a fatigue analyses. The actual load distribution between the girders demonstrated that the design distribution factor was conservative for this specific bridge. In addition, shifts in the location of the neutral axis were used to identify the point at which the steel began to yield, and the concrete began to crush. An FE model was created and calibrated to match measurements by changing the stiffness of the concrete deck. The FE model predicted a strain-time history resulting from the application of a controlled loading vehicle that was found to match the actual response quite closely. This is an excellent example of a successful SHM system based on the use of strain gauges. This study was successful partially due to the alternative load paths available with a slab-on-girder system. One of the objectives in this thesis is to see if the approach used by Cardini and DeWolf may be applicable to other bridge types such as the statically determinate steel truss bridge studied in this thesis.

Laman et al. (1999) tested three through-truss steel bridges that were constructed in the 1930's to measure the dynamic load allowance (DLA) factor, which is the degree by which the static response is increased by dynamic loading, experienced by the truss members, stringers, and floor beams. It was found that the DLA values did not change for vehicle speeds from 40 km/hr to 100 km/hr. The majority of the bridge response occurred at low frequencies, so the DLA was typically found to be small. The components of the structure that did have higher DLA values occurred with members that experienced a low strain response. The members with the highest peak strains experienced the lowest DLA factors.

With a three-dimensional truss, there is the possibility of alternate load paths providing redundancy. This has been demonstrated by measuring strains in existing infrastructure (Bakht and Jaeger 1990, O'Connell and Dexter 2002). Typically, the bridge deck plays a role in stiffening the structure, and heavy-class steel truss members provide extra rotational restraint. Cross bracing and longitudinal beam members have also demonstrated effectiveness in reducing the live loads that the members endure.

The studies discussed in this section found that the measured response does not always mimic what is commonly assumed during design. For example:

- The load distribution among components of built-up members is not always even;
- The supports for live loading scenarios do not always behave as pin/rollers; and
- The connections between truss elements may have some rotational fixity.

The impact factors observed in these studies were either non-existent, or had a value of 1.1 for the bottom chord (tension) members only. This thesis addresses each of these issues when analyzing the measured structural response under loading.

2.3.2 Reliability and Fatigue Damage Detection

A statistical approach was used in the following examples to estimate the remaining fatigue life of the structures. In most cases, the assumed fatigue-critical elements were instrumented, and the measured strain response was used for the statistical analysis. Each example is discussed individually, with the highlights of the study noted.

Instead of observing the global structural response under loading, Alampalli and Lund (2006) focused on the smaller bridge components, and then used the information to determine the reliability and safety of the entire structure. The AASHTO fatigue specified reliability methods were applied to estimate the remaining life of a steel deck truss bridge. The strain-time history was obtained from the instrumented members, and a strain histogram was produced. Using the AASHTO specifications (1990), the factored effective stress was calculated using Miner's rule (damage accumulation theory) and compared to the limiting stress range to determine the fatigue life of the instrumented member. It was found that most members had an infinite fatigue life except for four members that were predicted to have a fatigue life of 27 years. The

fatigue vulnerable members were the sole plates welded to the top flange of the girder to support the floor beams, and built-up tension members connected with welded stay plates. The welds increased the stress amplitude, whereas a bolted connection would have increased the fatigue life of these components. Members already damaged were omitted from this study, as there was not a criterion to follow to assess the remaining fatigue life.

Chan et al. (2001) used the strain-cycle history of connection components susceptible to fatigue in a fatigue analysis to estimate the remaining life of the Tsing Ma Bridge deck located in Hong Kong, China. Continuum damage mechanics (CDM) was used to estimate damage from fatigue and the results of this approach were compared to the results obtained using Miner's rule. The application of strain gauges has the potential to be successful in this case, since healthy bridge data have been collected, which is a key component for a statistical analysis to locate damage at some future stage. It was found that Miner's rule can provide a satisfactory conservative approach for the design of new structures, while CDM in combination with strain data may be a more accurate approach to estimate the remaining service life of a bridge since fatigue damage is not linear (as assumed by Miner's rule), but progressive and accelerates with age, a fact which was demonstrated with the CDM approach.

Liu et al. (2009) developed a model on which to base the reliability of the maximum stresses captured over time for individual bridge components. The measured strain histogram at each location was used to estimate the bounds and probability of exceeding a maximum value. The model then combined the individual probabilities in series or parallel, based on how the members were connected, and could be used to determine the global probability of failure. However, an assessment to determine the cause of an excessive value was not completed (i.e., damage location). Thus, this paper simply provides a method to determine if the structure is behaving in a manner similar to when it was first instrumented and monitored. This model could be considered a Level 1 SHM system, in that it can potentially predict the presence of damage, but not the location or severity.

Caglayan et al. (2008) used the strain-time histories as well as acceleration measurements in an SHM system applied to a four-span steel girder bridge. The strain-

time histories were used to produce a stress histogram to predict the fatigue life and determine member locations most susceptible to fatigue failure with the same approach as Alampalli and Lund (2006). Strain data, along with material tests and acceleration data, were used to refine an FE model, which was then found to represent the actual strain-time history very closely.

While the statistical approach to detect damage with strain data appears promising, there has not yet been a successful approach to monitor an already-damaged member. There are many bridges still in service that have experienced damage to an unknown extent (Federal Highway Administration 2001).

2.3.3 Temperature Effects

Some of the difficulties encountered when implementing an SHM system are caused by temperature effects on the structure itself and the effect that this has on the reliability of the strain data measured. Catbas et al. (2008) attempted to combine the long-term response due to dead load, live load, wind, and temperature variations using the strain-time histories on a long-span cantilever truss bridge. The objective was to capture the real-time effects that are difficult to model with an FE analysis. The temperature-induced strain was calculated using the yearly average as a baseline, with the upper and lower bound strains obtained from days that experienced the highest and lowest temperatures, respectively. It was found that temperature-induced strains can be more than ten times greater than traffic induced strains in some cases.

While it is necessary to consider the temperature-induced stresses on the structural components during design of the structure, it is not necessarily required for the analysis of strain data. For short-term strain measurements, under approximately ten minutes, the effects of a temperature change on the construction material would be negligible. However, for long-term strain measurements, the temperature-induced strains must be separated from the transient strains for a reliable analysis. One approach, developed by Omenzetter and Brownjohn (2006), used a moving average on the strain data to eliminate the temperature effects, based on the assumption that temperature effects will vary slowly relative to transient load effects. This process is referred to as the vector seasonal autoregressive integrated moving average (ARIMA). The coefficients of the ARIMA models vary with time to account for the change in

temperatures. The coefficients were not determined by the ambient temperature, but from the global strain response of the structure. The temperature effects can cause significant stresses due to constrained contraction and expansion; however, the use of short-term strain data under ten minutes has been found to eliminate the need for temperature correction in the consideration of transient events (Alampalli et al. 2006).

It appears, therefore, that for short-term measurements, there is no need to address the temperature effects. The methods discussed in this section are purely for the application of long-term measurements.

2.3.4 Measurement Considerations

To obtain accurate data that can be used in an SHM system, data processing techniques such as filtering and data sampling rates must be taken into consideration at the time of measurement. First of all, the data acquisition rate must be taken into consideration. The factors influencing the sampling rate include the natural frequencies of the structure, interfering noise frequencies within close proximity, and loading scenarios.

Acquiring data at too high a sampling rate will pose a processing and storage issue, while acquiring data at too low a frequency may pose an accuracy problem when it comes to filtering or obtaining dynamic information (filtering details are discussed in the following paragraphs). De Corte and Van Bogaert (2006) indicated that, due to an adjacent 15 kV power line, acquiring strain data at a frequency above 200 Hz caused too much distortion to the signal. Also, a sampling rate of less than 200 Hz was not recommended because it only took 5 seconds for the vehicle to pass the span travelling at a speed of 160 km/hr, so with a lower sampling rate, some of the response may have been lost. It has been suggested that the sampling rate should be at a magnitude higher (a minimum of ten times) than the natural frequency of the structure. The purpose of this is that some filtering techniques (such as decimating) smooth the data by averaging the samples over a user-defined factor, and then reducing the sampling rate by that factor. As a minimum, the sampling rate must be at least two times the highest natural frequency of interest (Nyquist frequency, further details provided in Chapter 3).

Consideration must be given to certain parameters related to the acquisition of strain-time data, such as the sampling frequency and filtering options. Filters can be

used at the sampling source or applied to the stored data, to obtain the desired response and remove unwanted components. A low-pass filter retains only signals below a user-defined frequency, while a high-pass filter removes signals below the user-defined frequency. With the use of these filters, noise can be removed and the static and dynamic responses can be isolated from one another. Although the response signal may be thought to improve with a higher-order filter (Laman et al. 1999), it is not always the case, as supported by the work in this thesis.

Laman et al. (1999) used a low-pass filter with a cutoff frequency of 5 Hz in order to eliminate the dynamic response from strain measurements on a bridge with a lowest natural frequency greater than 5 Hz, but keep the static response due to vehicle loading. Li et al. (2003) recommended a sampling rate between 25.6 and 51.2 Hz to limit the volume of data and still obtain accurate peak strain measurements for use in statistical fatigue analysis. The rationale for the chosen sampling rate was not provided, but the highest strain amplitudes occurred at frequencies below 2.048 Hz, as was shown in the frequency domain. Since this was a statistical analysis with the objective of observing the number of occurrences above a particular strain amplitude, this low sampling rate might have been thought appropriate to limit the data volume.

The approach used in this thesis was to obtain raw, unfiltered data that would be processed during the analysis stage. Each SHM study is expected to have different levels of noise and interference, and the filters were modified to work best with the data obtained in this study.

2.3.5 Finite Element Modelling

Producing an accurate finite element model that is representative of an actual bridge structure is a challenge. The modeller must make assumptions at each step in the construction of the model. The actual material properties, member properties, connection type and restraint conditions, for example, will all differ to some extent from the design assumptions. The following studies describe the issues encountered while attempting to match the measured to the modelled response, and the corrective steps taken.

The material properties, including the modulus of elasticity (stiffness) and density (mass), can have a significant effect on the model's accuracy. Caglayan et al.

(2008) conducted material tests to verify material properties for use in their FE model. Based on four material tests taken from a damaged lateral cross bracing member, the mean yield strength was found to be 238 MPa, with a nominal value (i.e., the mean value minus the standard deviation) of 217 MPa. The mean tensile strength was 388 MPa, with a nominal value of 372 MPa. However, destructive testing may not always be possible, so the best guess of material properties using the typically published values for the materials in use at the time of construction are often used.

With respect to support conditions, while it is common practice to assume ideal roller-supports for the purposes of bridge design, it may be found that this type of action is not, in fact, occurring. O'Connell and Dexter (2001) found that supports designed as rollers did not act as rollers under service level live loads. This resulted in higher predicted forces than measured, because supports that restrain the longitudinal movement put compressive forces in the bottom chord truss members, simulating arch-like behaviour. Enevoldsen et al. (2002) found that the support restraint conditions highly affect the load distribution, but could not provide ideal restraint conditions. In addition to the parameters just discussed, linear analyses are often used due to their relative simplicity, but they may not be capable of capturing the actual structural response experienced.

He et al. (2008) were successful in using measurements of the response of the steel truss Nanjing Yangtze River Bridge to refine an FE model by updating the modelling parameters based on sensitivity analyses. The steel modulus of elasticity (207,000 MPa), highway deck mass, and steel sleeper mass were all modified to achieve a good match between the measured and modelled mode shapes and natural frequencies. The measured and modelled stress-time histories were also found to correlate very closely. Only two modelling parameters were explored in this study (steel modulus of elasticity and mass). The other major modelling parameters not considered, but which could also play a very important role in achieving an accurate FE model response, are the degree of support restraints, connection types, and effective deck stiffness.

Nagavi and Aktan (2003) captured the strain-time history at numerous points on a heavy-class steel truss bridge during destructive testing and correlated the measurements to a nonlinear FE model to verify the results, as well as to better

understand how to create an accurate FE model. The steel material properties were modelled based on test results from samples taken from the bridge. The FE models were constructed with various combinations of truss and beam elements. Iterations of the FE models were produced, ranging between a full truss element model, a full beam element model, and a combination where truss elements were used for tension members and/or braces, and beam elements were used for compression members and/or sway frames. It was found that using beam elements for compression members was more accurate based on the measured results because the beam element allowed for some moment transfer that occurs with the heavier members at the connections. The truss elements were found to be a more accurate representation of the behaviour of the tension members and braces because of the smaller member sizes involved. Freezing of a roller, by restraining the movement in the longitudinal direction, was observed to produce less deflection under a given load condition than that observed with free-roller supports.

When the nonlinear models were loaded to yielding, it was found that hinges formed, reducing the end moments of the truss members. As a result, the loads were redistributed throughout the truss; ultimately, the truss became determinate once all of the elements had yielded. As mentioned in Section 2.2, during the destructive testing, the loads only reached approximately 40% of the anticipated capacity before failure. Failure was precipitated by the sudden release of a frozen roller, which forced an abrupt spike in the bottom chord forces, causing the corroded gusset plate at the support to break free from the bottom chord. While the FE model used in this study proved to be an accurate representation of the truss behaviour prior to failure, it was not able to capture the failure mode. Modelling accurate failure mechanisms is still a significant challenge.

Enevoldsen et al. (2002) instrumented a steel-truss-arch bridge constructed in 1912, to assess the differences between actual and FE modelled strain–time histories. It was found that there was load-sharing occurring in the FE model at the upper deck level between the deck, longitudinal beams, and crossbeams. Any modifications to the stiffness of these upper level elements resulted in a load re-distribution between these members. The FE model was modified so that it was able to simulate the instrumented

member measured axial forces. The modelling parameters found to be most important with regard to matching the modelled and measured results included:

- Joint stiffness between members (i.e., how much shear load transfer occurs),
- Rotational stiffness at joints connecting members (i.e., how much moment transfer occurs), and
- Crossbeam centre of gravity (i.e., how the geometric placement of members in the FE model affects the overall stiffness and load paths of the structure).

One of the findings of this study was that the pseudo-elements (redundant) shown in Figure 2.1, initially thought to only provide structural stability, were highly active in compression, relieving up to 17 MPa in stresses from the crossbeams. This is a significant level of stress, considering that the strain gauges only measured live loads and the majority of the axial forces expected in structures of this size typically result from the self-weight of the structure. This study demonstrates the need of an SHM system to obtain a clear understanding of how structures such as these are behaving prior to making conclusions as to the structural behaviour. If an FE model is to be used as part of the SHM system, it must be refined to match measurements as closely as possible in order to ensure that it is an accurate representation of the structure.

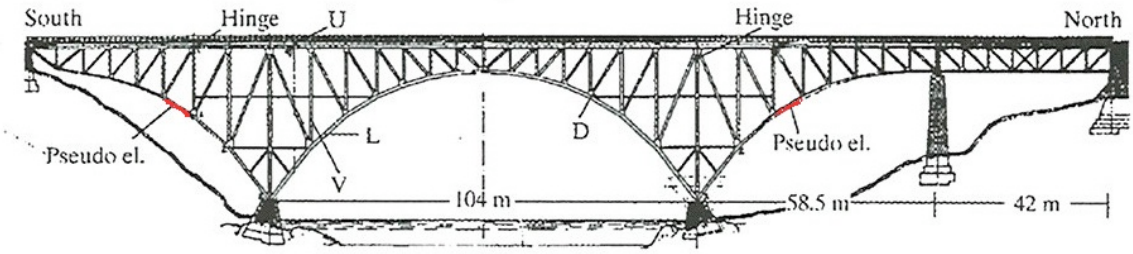

Figure 2.1. Elevation of the Forsmo Bridge, Sweden (Enevoldsen et al. 2002).

2.4 RESEARCH NEEDED

Published studies regarding the use of strain gauges for monitoring the health of steel truss bridges have generally involved either in-service bridges that are in relatively good condition, or decommissioned bridges that were tested to failure (Azizinamini 2001). What seems to be lacking is a reliable approach to apply an SHM system to an aging steel truss bridge experiencing relatively low live loads that is capable of

monitoring the progressive deterioration and possibly prolonging the service life. With measurements that can demonstrate that the structural elements are experiencing stress ranges within an acceptable level, or even below the expected/allowable stress amplitude, the risk decreases, which could possibly extend the service life of costly structures. DelGrego et al. (2008) investigated a 100-year old steel railroad truss bridge, but measurements were limited to the diagonal members. This thesis attempts to address this deficiency.

The literature illustrates that there are significant difficulties associated with creating an FE model of a truss bridge that is capable of accurately representing its behaviour. The construction of an FE model of a 100-year old steel truss bridge such as the Traffic Bridge, with low live loading (5 tonne limit), substantial modifications to the original design, and highly deteriorated bottom chords, is an even greater challenge. The successful creation and calibration of an FE model of the Saskatoon Traffic Bridge provides insight into its actual structural behaviour and provides guidance with respect to modelling similar structures. The FE model could then be incorporated into an SHM system used to detect damage. Ideally, the FE model provides a predicted load distribution. Combining the FE model with a measurement-verified response, the uncertainties with respect to structural behaviour are addressed, inherently reducing risk associated with the uncertainties. Also, with the measurement-verified FE model, it may be possible to detect damage over time by observing a change in the load distribution. Since the applied load always takes the stiffest path to the supports, any change in load distribution would indicate the presence of damage. However, it is recognized that damage detection may be difficult due to the limited opportunities for alternate load paths. In part, this study was completed to assess the possibility of implementing an SHM system for the Traffic Bridge in Saskatoon, SK.

3 DESCRIPTION OF EXPERIMENTAL PROGRAM

The experimental program was designed to complete two tasks:

1. To capture the response of the bridge members under realistic loads; and
2. To provide data to be used to calibrate and verify the FE model.

It is critical to understand the measured response of the bridge in order to create a model that accurately simulates the bridge's behaviour. The placement of the strain gauges on a member is also critical in order to capture a desired measurement that is useful in the analysis. This chapter describes the SHM objectives, instrumentation, placement of the instrumentation, and data analysis methods used to understand the actual load paths for the loading scenarios considered and to refine the FE model in a manner that is most likely to simulate the actual bridge response due to loading.

3.1 INTRODUCTION

The use of strain gauges in SHM is a popular choice of instrumentation due to the ease of installation, low cost of the sensors and the simplicity with which the strain data can be converted to useful stresses or forces. With the use of a sufficient number of strain gauges, the results can be used to verify the actual load paths associated with applied loads. More commonly, with more limited instrumentation, the critical structural members can be monitored to obtain the strain histograms over time to acquire the estimated fatigue-life estimates for those elements.

In order for an SHM monitoring system to be successful using strain gauges, the placement of the gauges is critical. While it is easy to generate large amounts of time-history data, those data may or may not be useful for determining the structural behaviour of the system and/or for damage detection. The objective of this experimental program was to use field measurements to obtain an accurate representation of the truss load-paths under controlled and ambient loading that could then be compared to results from a calibrated FE model. A total of 72 strain gauges were used to capture the load transfer mechanisms within the truss due to vehicle loading and to investigate the usefulness of such data as a structural monitoring tool. Accelerometers also were installed at the panel points along the bottom chord. The accelerometer data were used

to extract the dynamic characteristics of the bridge in order to verify the FE model response; no attempt was made to use the accelerometer data for vibration-based damage detection (VBDD), as that was not the focus of this study.

The five spans making up the Traffic Bridge are nominally simply supported and are believed to act independently of one another. To minimize the required instrumentation, data, and analysis for this feasibility study, only one of the five spans was instrumented. The second span from the south side of the river was chosen because of its accessibility for sensor installation, as shown in Figure 3.1, and due to its larger span of 61 m (200 ft) compared to the end span of 53 m (175 ft). The first three panels of the second span are located over dry land, making them easily accessible for installing the instrumentation. This location is also easy to access for setting up the portable data acquisition system when taking measurements. Due to the load restriction of 5 tonnes (MS50 design rating) on the Traffic Bridge, low response levels are experienced, and a larger span (61 m) was selected to maximize strain and accelerometer readings, thereby minimizing the effects of noise. The overall dimensions of the second span are shown in Figure 3.2. Appendix A contains portions of the original Traffic Bridge structural drawings for reference.

Figure 3.1. Installation of strain gauges on the bottom chord member.

The vehicle traffic ran on an asphalt surface, supported by a timber deck spanning laterally over the supporting joists. The joists run longitudinally and span

approximately 7.62 m (25 ft), supported by a floor beam that spanning laterally to the truss panel points, distributing the deck loads to the trusses.

The test program is described in the following sections, including the instrumentation location and installation, loading scenarios, and data acquisition and analysis considerations.

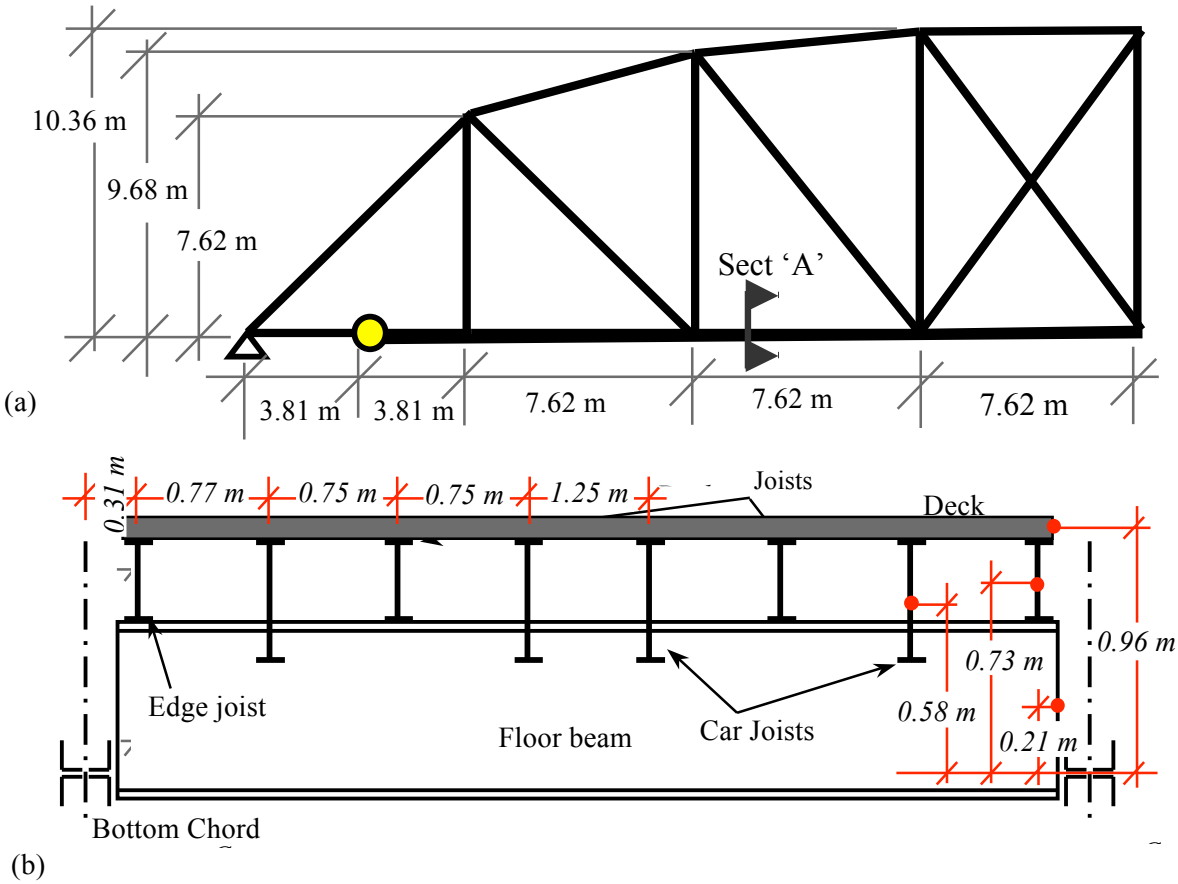

Figure 3.2. Traffic Bridge second span overall dimensions; (a) elevation view of half of the symmetrical span, (b) Section 'A' of deck and support system transferring loads to bottom chord, including modelled heights above the centroid of bottom chord member.

3.2 INSTRUMENTATION

3.2.1 Strain Gauges

The objective was to instrument one half of one truss intensively to obtain an accurate representation of the load paths within that segment of the truss. In addition, an attempt was made to identify critical members in case an expanded SHM system would be considered for other bridge spans. The majority of the strain gauges were installed on

the downstream truss within the first three panels nearest the south abutment. The downstream truss was chosen because it is easily accessed by a 12 m (40 ft) lift, and because it is less subject to tampering due to its limited public access since there is no adjacent walkway on this side of the bridge. Looking at the instrumentation on a more localized scale, each truss member consists of two to four individual steel sections that have been bolted or laced together to act compositely to resist loads. Therefore, each of the individual elements that make up a member had to be instrumented, not only to obtain the total member response, but also to investigate the potential to detect damage using changes to the load distribution among the individual elements over time. The strain gauges were typically placed at symmetric locations with respect to both principal member axes to facilitate subsequent analysis by eliminating bending effects from averaged gauge results.

The locations of the installed strain gauges are illustrated in Figures 3.3 and 3.4, and Appendix B. The members have been labelled based on the location between panel points of the truss. The panel point prefix contains either an 'L' for lower, or a 'U' for upper. Following the prefix is a numeral specifying the panel point in question, numbered consecutively starting at zero at the south support panel point. For example, the bottom chord member spanning between the support and the first panel point would be labelled 'L0L1'. The capitalized letter following the member location depicts the type of member instrumented: (A) top chord; (B) bottom chord between support and PT bulkhead; (C) typical bottom chord members; (D) vertical members; (E) diagonal members; and (F) car joists. The subscript letter 'd' refers to the downstream instrumented location, and 'u' refers to the upstream instrumented location. Figure 3.3 illustrates the general locations of the gauges on the truss members, while Figure 3.4 illustrates the location of the strain gauges on the member cross-section. To limit the amount of detail shown on Figure 3.4, Table 3.1 provides the actual dimensions to the strain gauges for bottom chord members. The downstream truss instrumentation (Figure 3.3 (a)) consisted of a total of 37 strain gauges. The bottom chord member in the first panel 'L0L1' was instrumented at two locations: one midway between the abutment and the bulkhead used to anchor the post-tensioning system, with a strain gauge attached to each leg of all the component members (Figure 3.4 (a)); and one midway between the

bulkhead and panel-point ‘L1’, with four strain gauges located as shown in Figure 3.4 (b). These two locations were selected to provide a means of estimating the live load resisted by the post-tensioning dywidag bars. The bars themselves could not be instrumented directly because doing so may have damaged the materials used to protect the bars from corrosion. Since the location of the dywidag bars limited access to the interior faces of individual angle sections, the bottom chord members in the next two panels, ‘L1L2’ and ‘L2L3,’ were each instrumented with only four strain gauges, with one gauge placed on the exterior leg of each angle, as shown in Figure 3.4 (b).

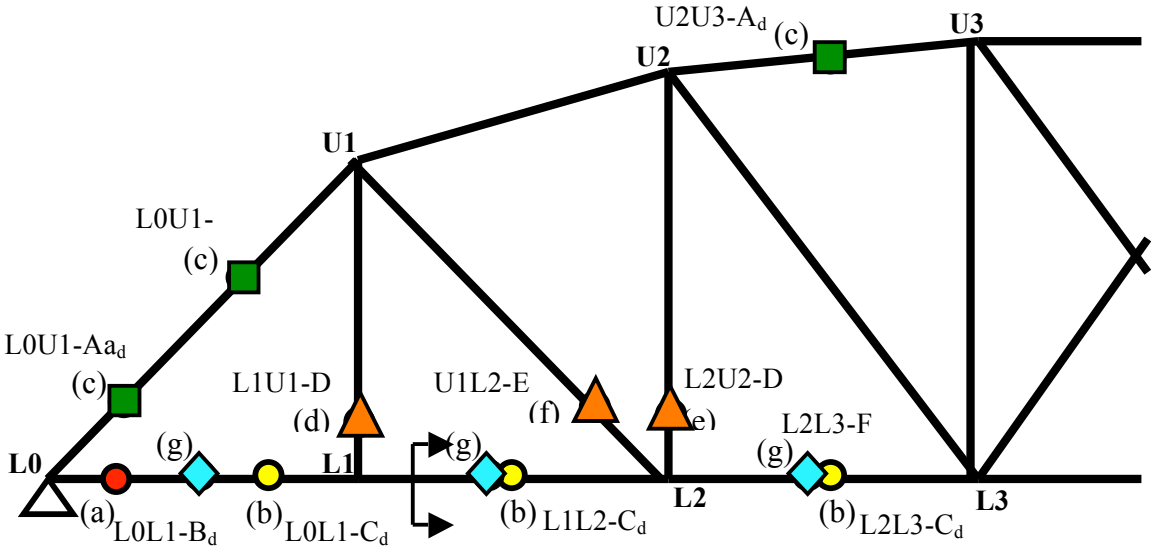

(a) Downstream Truss

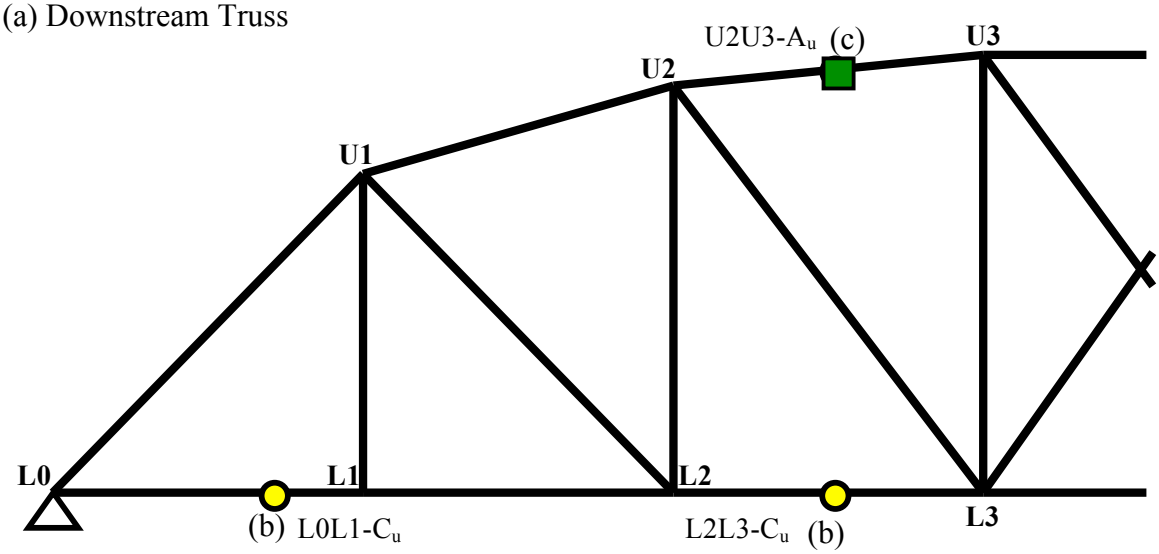

(b) Upstream Truss

Figure 3.3. Strain gauge layout on the second span from the south side of the South Saskatchewan River: (a) downstream truss including the downstream deck stringers; and (b) upstream truss. The letters adjacent to sensor symbols correspond to the matching part of Figure 3.4. Refer to Figure 3.4 for more details.

The top chord on the downstream truss was instrumented along two members: on the end post 'L0U1' (two locations), and at the midpoint of the third panel 'U2U3,' as seen in Figures 3.3 (a) and 3.4 (c). The three strain gauges at each location were installed at the midpoint of the top plate and at the mid-height of the two channels, as shown in Figure 3.4 (c). The unsymmetrical placement of the strain gauges relative to the centroidal axis of the cross-section meant that bending effects could not be simply eliminated by averaging the strain gauge measurements; rather, the strains due to axial load and bending had to be separated analytically based on linear elastic flexure theory (described in greater detail in Section 3.4).

The first two vertical members of the downstream truss were also instrumented. Member 'L1U1' consists of four angles; therefore, four strain gauges were installed, one on the exterior face of each angle (see Figure 3.3 (a) and 3.4 (d)). Member 'L2U2,' on the other hand, is composed of two channels; therefore, two strain gauges were installed, one at mid-height of each channel (see Figure 3.3 (a) and 3.4 (e)). The two angles that make up the first diagonal member 'U1L2' were also instrumented with one strain gauge on each of the vertical angle legs (see Figure 3.3 (a) and 3.4 (f)).

To investigate the upstream truss, two bottom chord members were instrumented midway between panel points with a strain gauge on the exterior face of each angle in the first and third panels 'L0L1' and 'L2L3' (Figures 3.3 (b) and 3.4 (b)). The top chord in the third panel 'U2U3' was also instrumented with three strain gauges (Figures 3.3 (b) and 3.4 (c)).

There are four car joists that are approximately located below the wheel paths: one for each vehicle wheel; two for each lane. The two car joists supporting the northbound traffic in the downstream lane were instrumented at mid-span in the first three panels. Figure 3.3 (a) and 3.4 (g) illustrate the strain gauge locations. Three gauges were installed per car joist: one at mid-height, along with one both 152 mm (6 in) above and below mid-height. The southbound traffic lane car joists (upstream lane) were not instrumented, as the focus was mainly on the downstream truss, and the adjacent lane. Appendix B contains more information regarding the installation of the strain gauges.

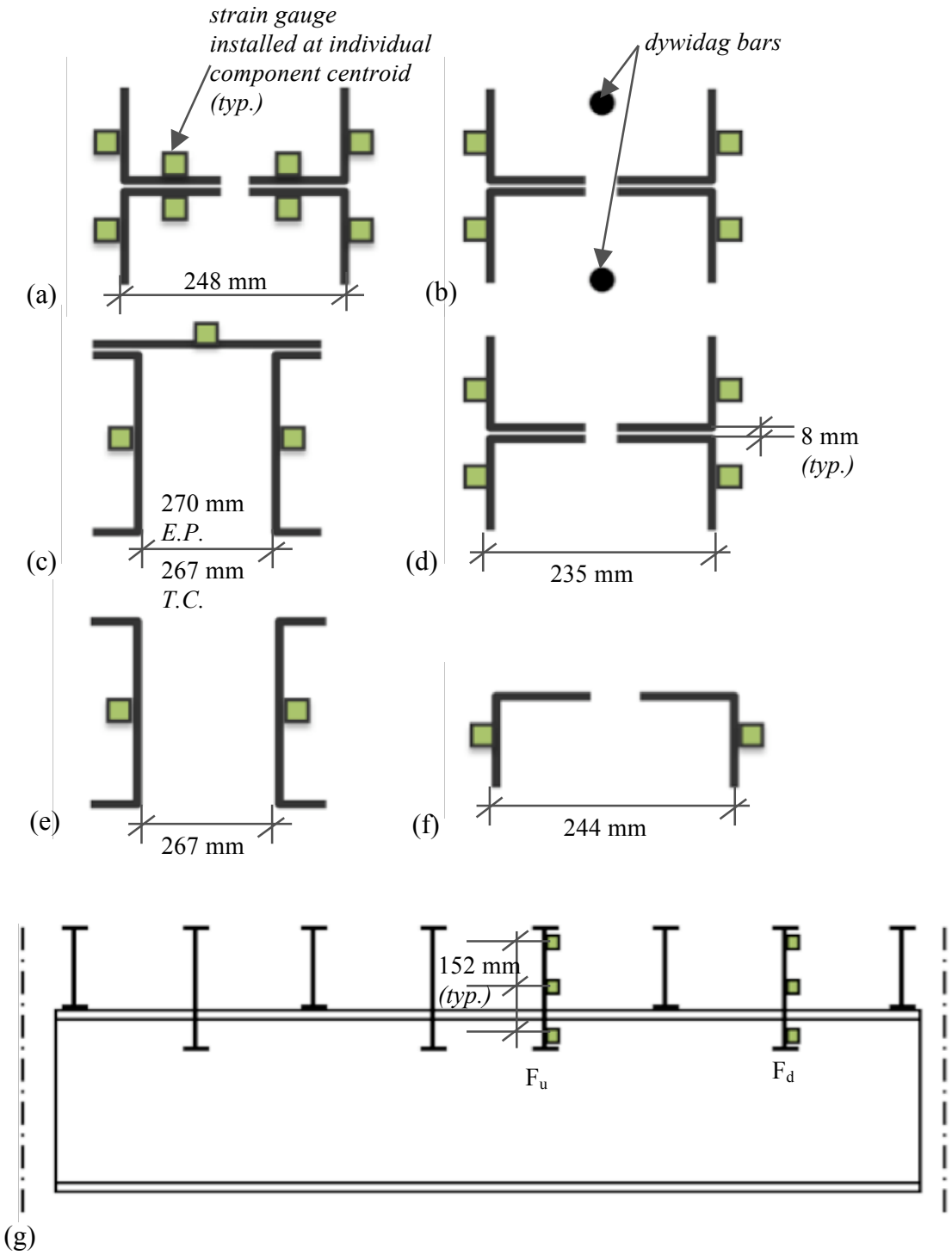

Figure 3.4. Strain gauge locations on member cross-sections: (a) bottom chord south of post-tensioning bulkhead; (b) bottom chord north of post-tensioning bulkhead; (c) top chord and end post; (d) vertical member L1U1; (e) vertical member L2U2; (f) diagonal member U1L2; and (g) downstream deck joists (typ.).

Table 3.1. Bottom chord member strain gauge installation at deteriorated locations.

Member	Strain Gauge	Perpendicular Distance From the Four Outside Corners
L0L1-B_d 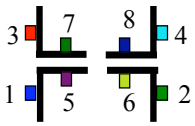	1	50.4 mm (2 in)
	2	50.4 mm (2 in)
	3	50.4 mm (2 in)
	4	76.2 mm (3 in)
	5	38.1 mm (1.5 in)
	6	38.1 mm (1.5 in)
	7	44.5 mm (1.8 in)
	8	50.4 mm (2 in)
L0L1-C_d 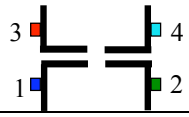	1	50.4 mm (2 in)
	2	76.2 mm (3 in)
	3	50.4 mm (2 in)
	4	66.7 mm (2.6 in)
L2L3-C_u 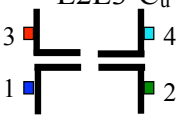	1	110 mm (4.3 in)
	2	50.4 mm (2 in)
	3	80.1 mm (3.2 in)
	4	50.4 mm (2 in)
L0L1-C_u 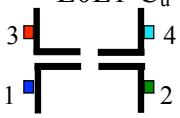	1	41.3 mm (1.6 in)
	2	50.4 mm (2 in)
	3	82.6 mm (3.3 in)
	4	50.4 mm (2 in)

In order to consider the effects of temperature variation during long-term monitoring, four "dummy" reference gauges were installed. These gauges were installed on the bottom flange of the floor joists near the end of the span, perpendicular to the longitudinal axes of these members, where strains due to imposed loading were thought to be negligible. Two reference gauges were installed in both panels 1 and 2, with one of these gauges on each of the upstream and downstream floor joists in each panel. In this study, the data obtained from each test (all with a measurement duration under 10 minutes) were zeroed individually, so it was not necessary to remove the temperature effects measured by the dummy reference gauges. The dummy reference gauges can be used for future long-term monitoring studies.

As a result, a total of 72 Vishay Micro-Measurements R-Leadwire-Series (designation LEA-06-W125E-350/3R) strain gauges were installed on the second span of the Traffic Bridge. The unit gauge length for these sensors is 3.175 mm (0.125 in) with a strain range of ±5000 microstrain (με). These units are fully sealed and were

spot-welded to the steel bridge members. The strain gauge welding unit utilized a low weld energy of 3 to 50 joules, leaving the member largely unaffected by the installation procedure. Prior to attaching each gauge, the paint and/or loose rust on the steel member was ground off, producing a clean surface prior to spot welding. Although the gauges have a nominal operating temperature range of -40°C (-40°F) to 83°C (180°F), careful handling was required to prevent the cracking of the vinyl coating that acts as a seal protecting the unit. As an extra precaution, Vishay Micro-Measurements M-Coat F sealant kit was used to further seal the strain gauges and inhibit corrosion. This sealant procedure included the application of an external rubber coating which adhered to the neoprene rubber sheets that, in turn, were placed on top of the butyl rubber interior sealant that was applied directly to the gauge. Aluminum foil tape was then used to secure the sealant assembly to the steel. The instrumented location was then painted to prevent further corrosion of the steel, and to disguise the presence of the gauges.

There were instrumentation locations on the bottom chord members where the gauges were not installed at the desired position of the angle centroid due to deterioration. The locations where this occurred are listed in Table 3.1, which gives the distance from the outside corner of the angle to the actual installed location.

3.3 LOADING

3.3.1 Ambient Loading

The Traffic Bridge has a load restriction of 5 tonnes (MS50 design rating). The typical traffic the bridge experiences consists of small passenger vehicles that are spaced sporadically with an average daily traffic count of 6,977 in 2008, 6,704 in 2006, 10,052 in 2003, and 10,869 in 2001 (City of Saskatoon 2008). Although the speed limit is 50 km/hr, it has been observed that many vehicles proceed at a slower speed due to the narrow bridge lanes. Measurements were recorded during both controlled and ambient loading. Under ambient loading scenarios, the recorded signal duration would last from one minute to ten minutes, depending on the traffic conditions at that time. The measurements would typically begin just prior to the instant when a vehicle entered the span, and continued until approximately 30 seconds after the last vehicle left the span to

allow for measurement of the free vibration of the structure. The measurement duration was typically kept to less than 10 minutes to limit the data file to a reasonable size.

3.3.2 Controlled Loading

A truck loaded to approximately 5 tonnes was used for the controlled loading scenarios. For the first trial (May 2nd, 2009), the truck weight was measured with the axle weight control unit (DAW300-PC) provided by International Road Dynamics Inc. (IRD). There was a high variability observed in the four different weight measurements performed. The vehicle mass had a coefficient of variation of 4% and a mean truck weight of 57.4 kN (5.85 tonnes), with a weight distribution shown in Figure 3.5. The mass distribution between the axles was found to be consistent with one third of the truck mass at the front axle, and two-thirds of the truck mass at the rear axle. The controlled loading vehicle was weighed by the City of Saskatoon (COS) for the second controlled loading trial (July 8th, 2009), giving a total vehicle weight of 49 kN (5 tonnes). Since the individual axle weights were not measured for the second trial, the mass distribution was assumed to be the same as for the first trial.

For both the first and second controlled loading trials, both static and dynamic load tests were completed. The static test consisted of parking the truck with the rear axle over each panel point, with the truck pointed in the normal direction of traffic in each lane for a minimum of 10 seconds. The static loading scenario is depicted in Figure 3.6, with the rear axle of the control load vehicle on the bridge span positioned, in turn, at each panel point L0 to L7. The truck was placed in both the southbound and northbound lanes of traffic, orientated in the normal direction of travel. The dynamic tests were conducted using vehicle speeds of 5 km/hr, 10 km/hr, 20 km/hr, 30 km/hr, and 50 km/hr. The truck was driven in each lane in the typical direction of travel (southbound or northbound) for a minimum of three trials for each speed and direction. More information related to the controlled loading scenarios can be found in Appendix B, while the strain values acquired during the controlled loading scenarios can be found in Appendix E.

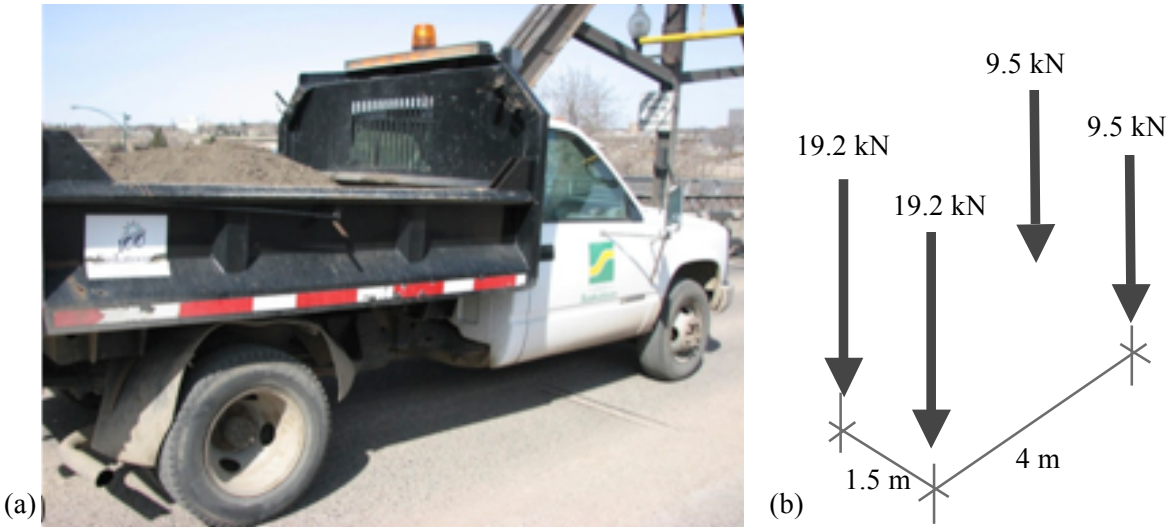

Figure 3.5. (a) Controlled loading vehicle; (b) Weight distribution for trial one.

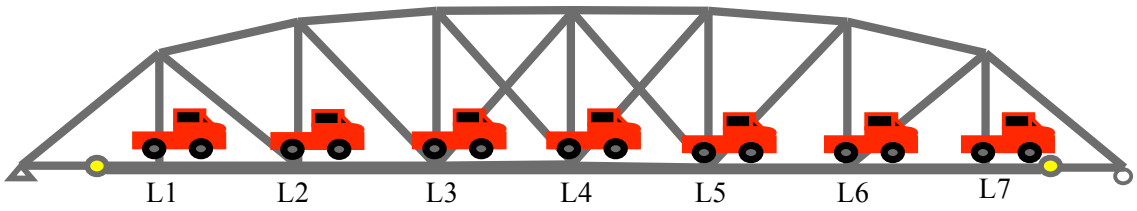

Figure 3.6. Static controlled loading scenarios L0 to L7. However, for the analysis, only panel points L1 to L7 were used.

The measurement techniques varied slightly between the first and second controlled loading trials. During the first trial, the recording period was limited to the time that the truck was on the instrumented span. In addition, the static load measurements were obtained intermittently, recording only a 10 second duration when the truck was parked at each panel point. This provided low confidence in the measurement results as some of the data was difficult to assess due to the following two main issues:

- Three baseline strain measurements were obtained—prior to, during and after the static loading—by recording the unloaded strain signal for two-minute intervals, and averaging the measurements over each interval. The difference between these three baseline average values was significant; the baseline strains varied, on average, by approximately 7 to 10 με, which was, in some cases, the maximum strain experienced under the controlled loading scenarios. It was

therefore felt that insufficient baseline strain measurements were recorded to provide a reliable estimate of their values.

- The 10 second signal length was a static measurement, meaning that no change in the strain signal was expected. At the low level strain readings observed, however, signal noise (i.e., variation in the signal value) was significant. The baseline strain was subtracted from the mean value of strain over the 10 second interval to obtain the estimated static strain.

It was concluded that, to provide better reliability (i.e., greater certainty regarding the static strain values) with this method, a baseline strain should have been recorded just before and after each static panel-point loading recording.

A different approach was taken for the second controlled loading test, lengthening the duration of the measurement to improve the quality and value of the resulting data as described below and illustrated in Figure 3.7. The static load test measurement for the second trial was started approximately 5 seconds prior to the truck entering the span. The truck was then driven at a crawl speed as the rear-axle of the vehicle was moved to each panel point, at which time the vehicle was halted for at least 10 seconds before moving on to the next point. The recording was terminated after the vehicle left the span, providing a measurement duration of approximately 2.5 minutes, or approximately 75,000 strain samples (vector length). This provided a good level of confidence in the results, because baseline strain readings were available at the beginning and end of each record. The recorded strain values at each panel point were easily obtained from appropriate sections of the record, (see Figure 3.7), and any change in baseline strain due to temperature effects was neglected due to the short recording duration.

The dynamic load test measurements followed the same procedure as was used for the second trial of the static measurements, except that the vehicle was not halted during the test, but kept at a constant speed. The control-loading vehicle was driven in both the southbound (upstream) and northbound (downstream) lanes three times each, at speeds of 5 km/hr, 10 km/hr, 20 km/hr, 30 km/hr, and 50 km/hr. The vehicle maintained an approximately constant speed during each recording. The recordings began approximately five seconds prior to the truck entering the span to properly initialize the

strain readings. The recording was terminated approximately 10 seconds after the truck left the span to provide a good opportunity to monitor the bridge during its free-vibration stage after the loading event.

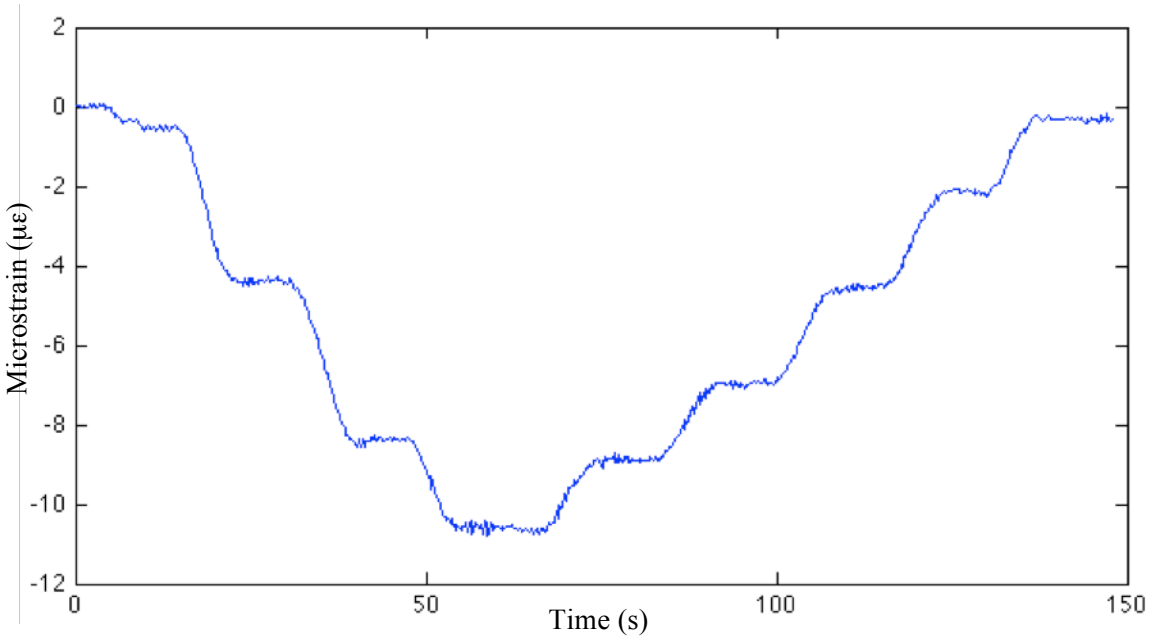

Figure 3.7. Top-chord member ($U2U3_d$) static strain-time history acquired during the second static controlled loading trial.

3.4 Data Acquisition and Strain Measurement Conditioning

To interpret the strain histories with a higher degree of confidence, the measurements had to be conditioned to remove unwanted noise to better represent the response. Based on the response to be extracted (i.e., the static or dynamic response), different approaches were taken, with the steps followed discussed below.

3.4.1 Strain Sampling Rate Considerations

A high *sampling frequency* of 500 Hz was used to measure the strain-time history for all load cases. Although De Corte and Bogaert (2006) recommended a maximum sampling rate (highest number of samples recorded per second) of 200 Hz to eliminate signal interference from power lines, it was found that, even with a sampling frequency 2.5 times greater than the recommended sampling rate, this distortion was easily removed with filters applied to the data. The purpose for using this high frequency was to eliminate the possibility of aliasing. Aliasing is an artificial measured response

due to having an actual frequency component greater than what can be detected based on the sampling rate (Penny et al. 2003). The active vibration modes of bridge structures typically occur at frequencies below 20 Hz. While these structures may have a measurable modal response well above 20 Hz, those modes are less likely to contribute at significant levels to the overall response.

A sampling rate of 500 Hz allowed the measurements to be decimated by a factor of 10 (as explained in the following paragraph), reducing the effective sampling rate to 50 Hz. The highest frequency that can be recognized from a measurement is half of the sampling rate, so for this case it was 25 Hz, which is higher than the maximum estimated frequency of interest. This maximum detectable frequency is commonly referred to as the *Nyquist* frequency f_{Ny} (Penny et al. 2003):

$$f_{Ny} = \frac{f_s}{2}, \qquad \text{or} \qquad f_{Ny} = \frac{1}{2\delta t}, \qquad \{3.1\}$$

which is equal to one half of the sampling rate f_s with a sampling interval of δt. With a high sampling rate, the Nyquist frequency was easily greater than the highest natural frequency of interest, thereby minimizing the possibility of aliasing.

Decimating is a filtering tool that is used to smooth the data to filter out any unwanted noise in the signal and reduce the sampling rate by a user-specified factor r. The decimating tool used was one of the built-in functions in Matlab (Matlab 2009) and had a built-in low-pass filter with a cut-off frequency, f_{lp}, of

$$f_{lp} = \frac{0.8 f_s}{2r}. \qquad \{3.2\}$$

Decimating was not used for the strain-time history analysis, but was applied to the accelerometer data in the dynamic analysis (as explained in Section 3.5.2). Data decimation is explained here because the analysis methods used must be taken into consideration at the data acquisition stage to ensure an adequate sampling rate.

3.4.2 Strain Noise Considerations

A *low pass filter* with a cut-off frequency of 50 Hz and an order of three was used in order to eliminate noise from the strain response. The low-pass frequency cut-off requirements were determined by plotting the Power Spectral Density (PSD) functions for strain signals. The PSD displays the amplitude of the signal in the

frequency domain. Figure 3.8 displays the PSD for a 30 km/hr controlled loading scenario. It is evident that the strain response occurred almost entirely in the quasi-static frequency range below approximately 2 Hz. However, a low-pass filter cut-off for measurements of 50 Hz was found to be adequate to eliminate high frequency noise such as electrical interference from the signal, and was used for the analysis.

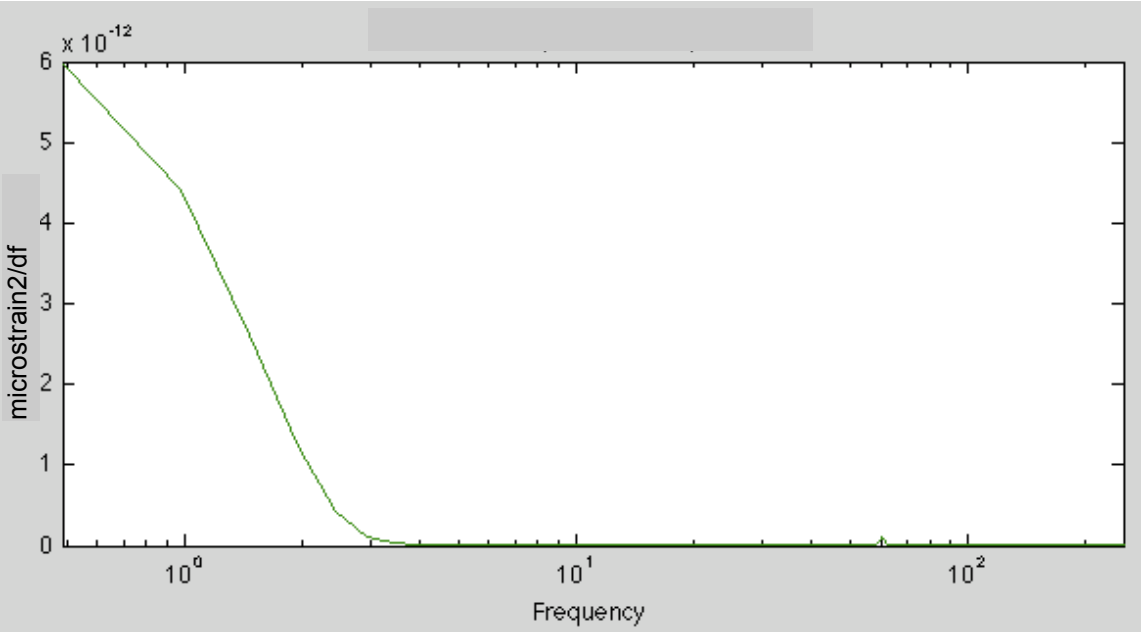

Figure 3.8. Example strain Power Spectral Density function for a controlled loading test at 30 km/hr.

Any frequency component greater than the cut-off frequency f_{lp} was filtered out of the measured response. The resulting data were free of high frequency noise. The filter employed was a third-order lowpass Butterworth filter (Matlab 2009).

A *high-pass filter* was not used for strain measurements because of the high amplitude of the low-frequency response, since such a filter would result in the majority of the static response being removed. Also, a high-pass filter was deemed unnecessary due to lack of signal drift. A high-pass filter may be necessary during cold-weather dynamic monitoring, because the measurement process can slowly heat up the gauges, resulting in a drift in the signal. The temperatures experienced during the May 2nd and July 8th measurement trials were between 1^{o}C to 18^{o}C, and significant signal drift was not observed.

3.4.3 Accelerometers

Accelerometers were used to measure the dynamic response of the bridge under controlled and ambient traffic conditions. As the focus in this project was on the use of strain gauges in an SHM system, the data collected from the accelerometers were only used to refine and verify the FE model. To monitor both the upstream and downstream trusses with a limited number of sensors, two separate instrumentation set-ups were used, each comprising eight sensor locations. Two reference accelerometers were used to correlate the measured response from the upstream truss to that of the downstream truss in order to obtain the complete dynamic response. Figure 3.9 illustrates the accelerometer instrumentation plan: the triangles represent the reference accelerometers that remained in the same location for both test set-ups; the circles represent the upstream monitoring set-up; the squares represent the downstream monitoring set-up. The vertical acceleration response was measured at each of the specified locations.

The size of the data files was found not to be a concern, as the measurement duration was typically less than 10 minutes. The data were acquired using a National Instruments model SCXI-1001 chassis, and a model 6036E 16 bit DAQ card. No filtering was implemented on the DAQ unit; only an initial "zeroing" of the gauges prior to data acquisition was performed to ensure that the readings would not saturate the sensors. Filters were applied digitally during the data conditioning and analysis stage. This way, the original data were always available, and the data from specific events were filtered individually to get the best representation of the response.

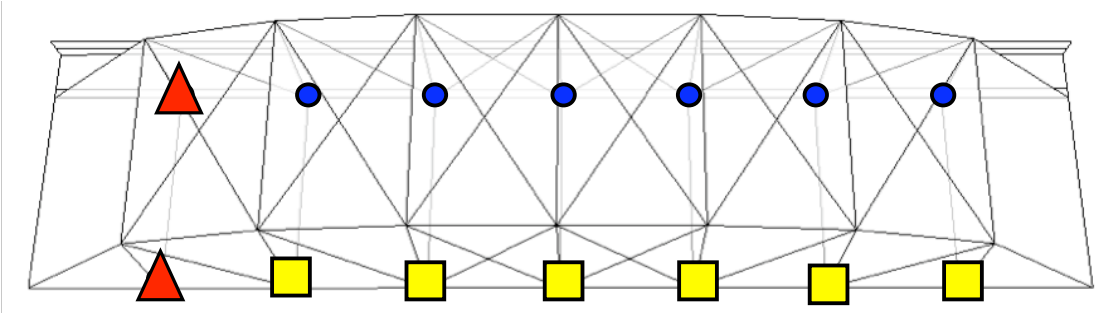

Figure 3.9. Accelerometer instrumentation plan: reference accelerometers in red triangles; upstream accelerometer set-up in blue circles; downstream accelerometer set-up in yellow squares.

Kinemetrics Inc. (Pasadena, CA) EpiSensor ES-U model accelerometers were used. The accelerometers were set to a maximum range of ±10g with a precision of 0.0025g.

3.5 DATA ANALYSIS

The collected raw data were smoothed in preparation for further analysis by applying filters that removed any extraneous noise collected during the sampling process. These filters are described in the following sections.

3.5.1 Strain Data

The strain-time histories from the bridge were analyzed using the software program MatLab™. The signals at various stages of processing are shown in Figure 3.10. The data were first zeroed (Figure 3.10 (b)) to remove the static offset readings existing in the system prior to the truck entering the span (Figure 3.10 (a)). A low-pass Butterworth filter (MatLab 2009) was then applied to remove frequency components above 50 Hz (Figure 3.10 (c)). A 50 Hz cut-off frequency f_{cut} was chosen to retain the dynamic response of the structure while eliminating the signals picked up from other sources such as electrical interference. To use a Butterworth filter, the user must specify the cut-off frequency, in a normalized form Wn, where

$$Wn = \frac{f_{cut}}{0.5 f_s}, \qquad \{3.3\}$$

as well as the desired order; an order of three was chosen for this study. The Butterworth low-pass filter retains all sample points. Therefore, to smooth the data below the cut-off frequency, a moving average filter was then applied (MatLab 2009) over a window length of 50 to 100 data points (0.1 to 0.2 s), depending on how clean the original signal was (Figure 3.9 (d)). Only the window length is specified to define this moving average filter.

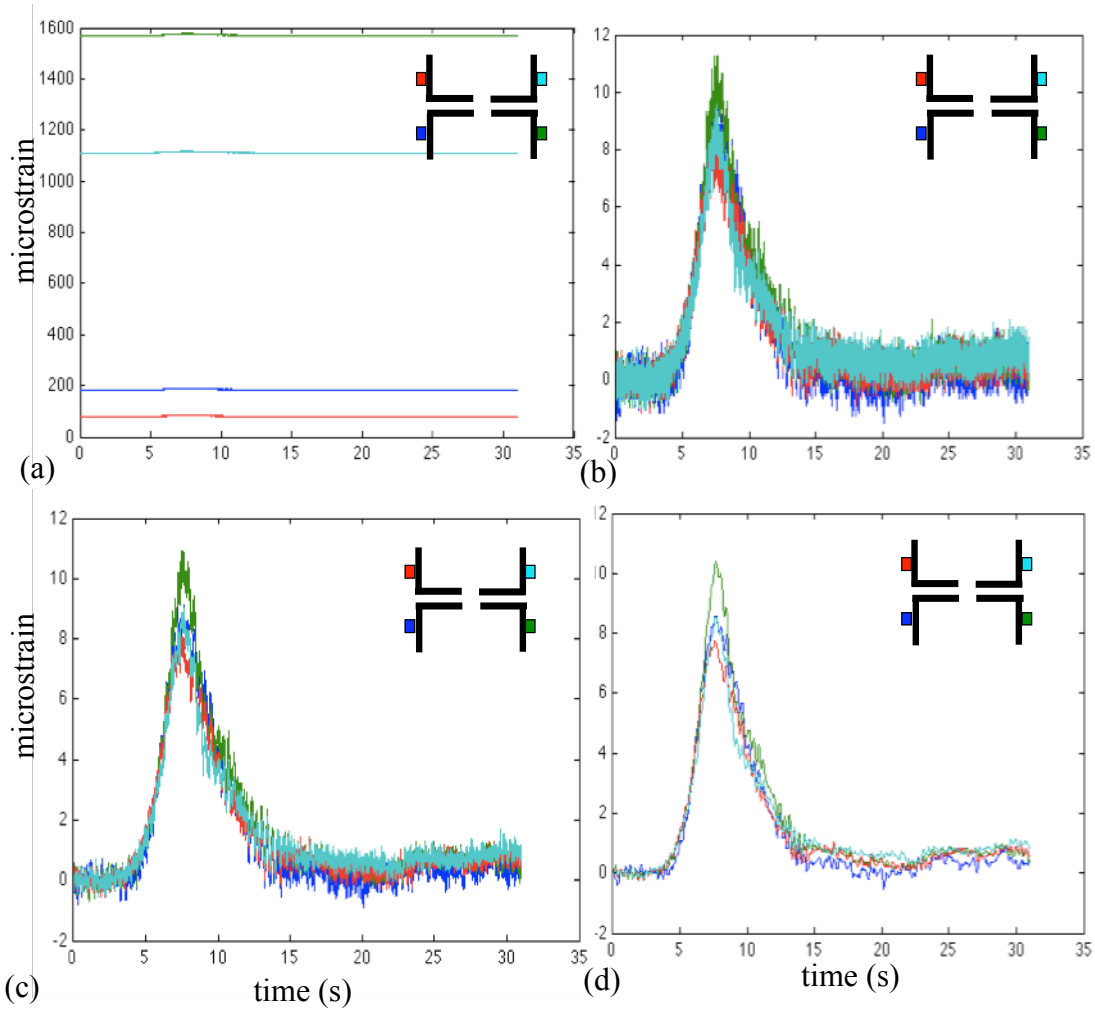

Figure 3.10. Signals from the four strain gauges for the downstream bottom chord member $L2L3_d$ at various stages of processing: (a) raw data; (b) after zeroing; (c) after applying a low-pass filter; and (d) after applying a moving average filter.

For the static load tests, the resulting axial force at each cross-section, F_{member}, was calculated using an average strain value ε_{avg}, which was the obtained using measurements from all strain gauges at that cross section, and where the strain value at each gauge was averaged over the time that the truck was in a particular location. The averaged strain value was multiplied by the modulus of elasticity of steel E and the estimated cross-sectional area A at the location of the instrumentation to obtain the axial force as follows:

$$F_{member} = \varepsilon_{avg} EA \qquad \{3.4\}$$

A significant amount of deterioration has occurred to the bottom chord members over their service life, with an average net section loss of 31%; at some locations, the estimated net section loss is 51% (Stantec 2005). The resulting axial force estimates for the bottom chord members were, therefore, produced with a high level of uncertainty due to the large potential variability in bottom chord member cross sectional areas. Attempts to measure the cross-sectional area were largely unsuccessful due to two primary factors: (a) the horizontal portion of the angles were bolted together at the vertical centroid, making it impossible to measure and visually observe the entire section; and (b) there was considerable variability in the level of deterioration in the vertical legs of the angles, making it impossible to obtain a representative measurement with callipers. This problem is addressed in Chapter 5, when correlating the model to the measured results. The full nominal cross-sectional area was assumed for the truss members deemed to be in good condition, which was the case for all members located above the deck.

With the exception of gauges on the top chord truss members, the strain gauges were installed symmetrically on the truss members, relative to the principal axes of the built-up cross section, at the centroids of the individual components (see Figure 3.4). This simplified the data analysis because the strain readings at any given location were easily averaged to eliminate any strain contributions due to bending about the built-up section axes.

The unsymmetrical placement of the strain gauges on the top chord truss members relative to the principal centroidal axis of the cross-section meant that bending effects could not be eliminated by simply averaging the strain gauge signals; rather, the strains due to axial load and bending had to be separated analytically based on linear elastic flexure theory. Assuming a uniaxial stress state, the normal stress at the "i^{th}" gauge, σ_i, is equal to its strain, ε_i, multiplied by the modulus of elasticity E. This stress can be split into two components:

$$\sigma_i = \varepsilon_i E = \frac{P}{A} \pm \frac{My_i}{I} \qquad \{3.5\}$$

where the axial load P divided by the cross-sectional area A makes up the axial component; and the moment at that location M, multiplied by gauge distance from the

centroid y_i, divided by the moment of inertia I about the centroidal axis makes up the bending component. The two corresponding strain components are shown in Figure 3.11, along with the cross-sectional locations of the measured strains.

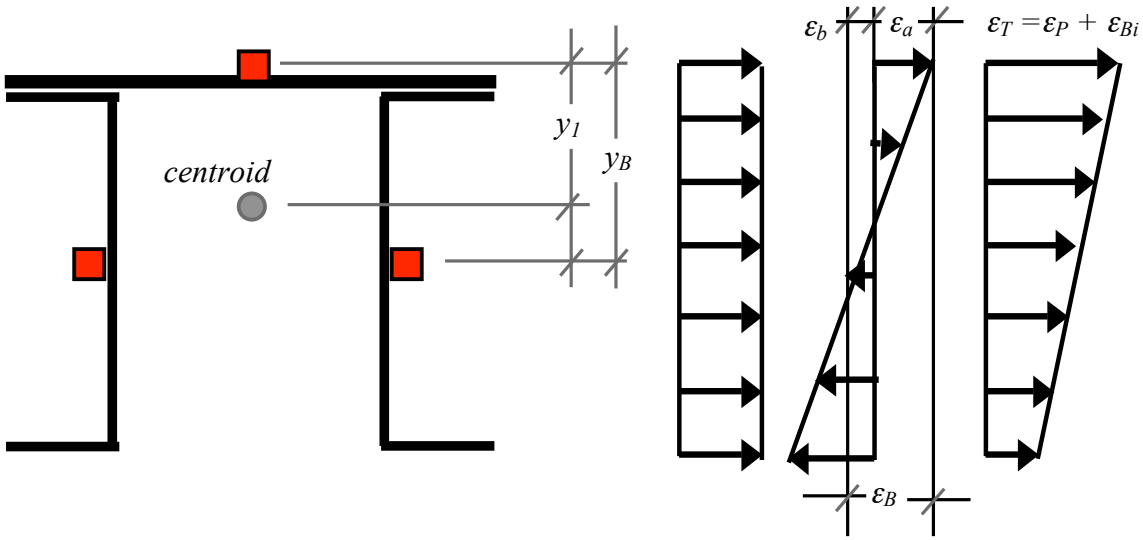

Figure 3.11. Top chord cross section, showing the locations of gauges relative to the centroidal axis, and the components of strain.

The bending strain per gauge was separated from the axial strain by first taking the measured bending strain ε_B (the difference between the measured strain at the top plate gauge ε_1 and the average of channel gauges ε_2 and ε_3, $\varepsilon_{2,3}$), and using similar triangles to obtain the following relationships:

$$\varepsilon_a = \varepsilon_B \frac{y_1}{y_B}, \quad \text{and} \quad \varepsilon_b = \varepsilon_B \frac{y_{2,3}}{y_B}, \qquad \{3.6\}$$

where y_B is the distance between the top plate gauge and the channel gauges, as shown in Figure 3.11. The total axial strain, ε_P was then calculated by subtracting the bending strains, ε_a and ε_b, from their respective measured individual strains ε_1 or $\varepsilon_{2,3}$ and averaging the results:

$$\varepsilon_p = \frac{1}{3}\left[\left(\varepsilon_1 - \varepsilon_a\right) + \left(\varepsilon_2 - \varepsilon_b\right) + \left(\varepsilon_3 - \varepsilon_b\right)\right] \qquad \{3.7\}$$

The strain-time histories of all members and loading events were then analyzed on an individual member basis and used to help calibrate the FE model described in Chapter 4.

3.5.2 Accelerometer Data

The raw, unfiltered accelerometer data were analyzed using the software program MACEC (2003). This software takes the output signals (acceleration) and applies the stochastic subspace identification (SSI) method (Peeters et al. 2001) to extract the mode shapes and natural frequencies. The three sampling parameters that must be input prior to the SSI analysis are:

- The instrument sensitivity for the accelerometers in mV/unit (the accelerometer sensitivity was set at 10 V/g, which is equal to 1019.4 mV/(m/s^2));
- The sampling rate of 500 Hz; and
- The instrument degrees of freedom, including instrument type. For this case, the acceleration was measured in the vertical direction only, hence had only a single degree of freedom.

The measured acceleration was pre-processed as follows (prior to implementing the SSI method). The data were decimated by a factor of 10 to smooth the data, eliminating unwanted higher frequency signal noise, and effectively reducing the sampling rate from 500 Hz to 50 Hz. At this stage, the following SSI parameters were estimated for the analysis:

- The expected model order, which was estimated by the number of peaks in the power spectrum multiplied by a factor of two. An expected model order of 8 was used for the analysis.
- The model order range of 2:20 was used. The poles are calculated for each model with an order up to the specified value, and used to determine the stability of the modelled measurements (MACEC 2003).

After initializing the SSI method, MACEC provided stabilization plots where only the most stable poles were chosen in estimating the measured mode shapes and frequencies. The measured dynamic properties were then compared to the modelled results to provide a means to verify the model calibration. The amplitudes of the

modelled mode shape vector $\boldsymbol{\phi_c}$ were normalized to the measured mode shape vector $\boldsymbol{\phi_d}$ using a modal scale factor, MSF_{cd}, as follows (Allemang 2003):

$$MSF_{cd} = \frac{\{\phi_d\}^T \{\phi_c^*\}}{\{\phi_d\}^T \{\phi_d^*\}} \qquad \{3.8\}$$

Once the mode shapes had been normalized, the modal assurance criterion MAC_{cd} could be calculated by summing the squares of the vectors as follows (Allemang 2003):

$$MAC_{cd} = \frac{\left|\{\phi_c\}^T \{\phi_d\}\right|^2}{\{\phi_c\}^T \{\phi_c\} \{\phi_d\}^T \{\phi_d\}} \qquad \{3.9\}$$

A MAC value of one indicates perfect correlation between the vectors being compared, whereas a MAC value of zero would indicate that the vectors are orthogonal. For the FE model to be considered an accurate representation of the real bridge, a MAC value very close to one, (within approximately 5%) was desirable.

4 NUMERICAL MODEL

4.1 OVERVIEW

The intention of the finite element (FE) model was that it be representative of the existing structure to provide some insight into how the truss system is behaving, and to simulate the effect of damage and determine how it might be detected. In order for the FE model to match the measured strain and acceleration response, the modelling parameters such as member properties, geometry, and support conditions must represent reality as accurately as possible. With the measurement-verified FE model, the actual load paths were established and used to estimate, among other things, the effectiveness of the post-tensioning system installed to reduce the bottom chord axial loads. The resulting FE model was also used to ascertain the effects of future damage to specific members, and to see if damage detection using strain gauges is feasible as a long-term SHM system.

A detailed description of the finite element model, as well as the modelling parameters studied to match the existing structure, is provided in the following sections.

4.2 DESCRIPTION OF BASE MODEL

The interior 61 m (200 ft) span of the Traffic Bridge was modelled using the commercial software package ANSYS (2007), as shown by a graphical representation in Figure 4.1. The initial basic model used four element types and consisted of 1430 nodes and 1151 elements. All truss members were geometrically positioned through their centroids with regard to elevation, as well as their lateral and longitudinal locations. However, all deck, joist, deck beam, and walkway deck elements were positioned at the elevation of the bottom chord centroid. This elevation positioning of all deck elements simplified the model construction by eliminating the need for artificial connector elements to bring the deck elements to their actual elevation.

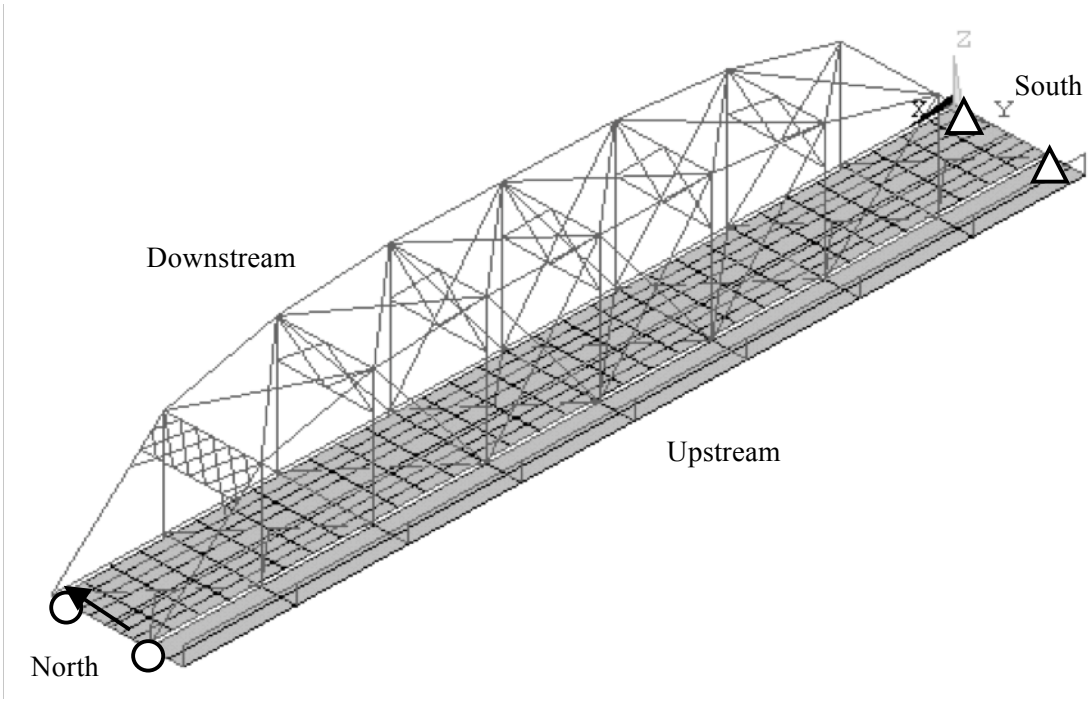

Figure 4.1. 3D graphical representation of the ANSYS FE model, including support conditions (see Table 4.1 for explanation).

4.2.1 Support Conditions

The original support conditions were modelled as ideal pin-roller supports. The southern supports restrained translation in the longitudinal 'x', lateral 'y', and vertical 'z' directions, without restraining rotation (see Figure 4.1). The northern supports were both fixed against translation in the vertical direction, but only the upstream northern support was fixed against translation in the lateral direction. The longitudinal direction was not restrained against translation at either northern support. Table 4.1 summarizes the support conditions.

Table 4.1. Summary of original support conditions.

Support	Symbol (see Figure 4.1)	Translational Restraint
Upstream South 'L0'	△	longitudinal, lateral & vertical
Downstream South 'L0'	△	longitudinal, lateral & vertical
Upstream North 'L8'	○	lateral & vertical
Downstream North 'L8'	○	vertical only

4.2.2 Elements

For all truss members, the ANSYS 3D beam finite element BEAM4 was used. Although truss members are typically idealized as two-force members that are assumed to take only tension and compression forces, in reality, the members do experience bending due to self weight, eccentric load transfer, and dynamic excitation. The BEAM4 element can experience tension, compression, bending, and torsion. It features six degrees of freedom at each node: three translational and three rotational.

The timber/asphalt deck was modelled using 3D shell SHELL63 elastic elements. This element features four nodes, each with six degrees of freedom: three translational and three rotational. The SHELL63 element can, like a BEAM4 element, experience tension, compression, bending and torsion. It can be defined with varying thickness at each of the nodes, and has isotropic material properties.

The post-tensioning dywidag bars were modelled using the LINK8 spar (truss) element. These elements were attached to the bottom chord member, in an uninterrupted span extending from 3.81 m (12.5 ft) from each support, as illustrated in Figure 4.2. These pinned elements resisted longitudinal displacements only, not in-plane flexure or torsion. Based on specifications provided on the post-tensioning system design drawings (Wardrop 2006), an iterative process was carried out to determine the appropriate initial strain when the system was installed. A pre-stressing strain was assumed for the initial analysis, which was then modified in further analyses to achieve the specified pre-stressing force under self-weight conditions. A pre-stressing force of 274 kN was used for the downstream truss, while 297 kN was used for the upstream truss. The difference in pre-stress forces was due to the unbalanced dead load acting on the upstream truss produced by the walkway.

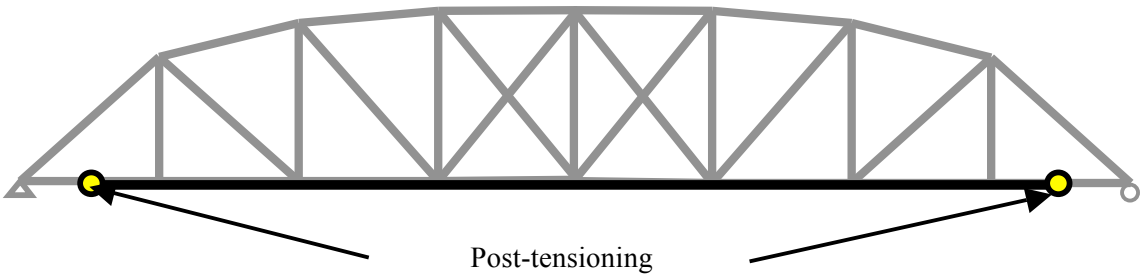

Figure 4.2. Post-tensioning bulkhead attachment to bottom chord members, 3.81 m (12.5 ft) from supports.

4.2.3 Connectivity

All linear (beam and truss) members were assumed to have pinned connections at both ends. To model this condition with ANSYS, each member was defined with unique nodes at both ends that were not shared with any other member but which were coincident with nodes from adjacent members. To connect the members, the translational degrees of freedom of the coincident nodes of adjoining members were coupled (i.e., the translational displacements were forced to be equal), while the rotational degrees of freedom remained uncoupled, thus permitting independent rotation of the connected member ends. To prevent members from spinning freely about their longitudinal axis, the rotational degrees of freedom about the member axis were restrained at both ends of the member.

4.2.4 Member Properties

Only two material types were used in the construction of the model: steel and timber, with their specific properties listed in Table 4.2. The base model consisted of members assumed to be in pristine condition, with the full cross-sectional areas assumed, despite the actual estimated section loss due to corrosion experienced by the steel members at and below the deck level. Table 4.3 describes the member location, shear area, moment of inertia about each axis, as well as the estimated added mass for connections. The member types referenced in Table 4.3 are shown in Figures 4.3 and 4.4. The added mass was estimated to be between 1% to 5% of the cross-sectional area of the member, depending on the type of connection. For smaller connections, such as for the diagonal members, 1% added mass was used, whereas for the larger connections with gusset plates, such as for the bottom chord members, 5% added mass was used. The asphalt was assumed to contribute zero stiffness; no separate elements were used to model the asphalt, and its mass was added to the deck. An accurate representation of the mass was critical when matching the dynamic characteristics of the structure.

Table 4.2. Steel and timber material properties used in the FE model.

Material	Steel	Timber
Modulus of Elasticity	200,000 MPa	10,000 MPa
Poisson's Ratio	0.3	0.25
Shear Modulus	76,923 MPa	N/A
Density	7850 kg/m^3	550 kg/m^3

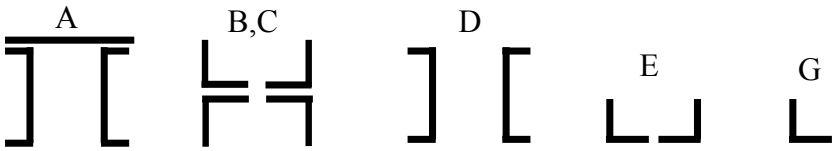

Figure 4.3: Truss member types used for the FE model (see locations and properties listed in Table 4.3).

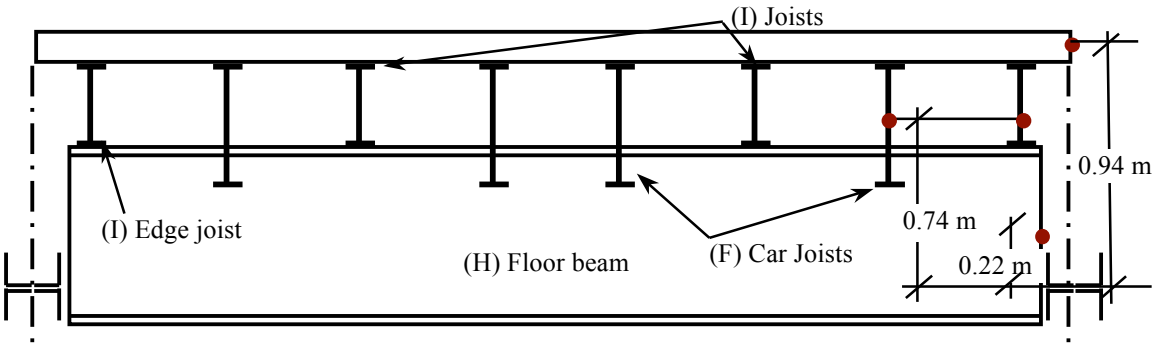

Figure 4.4. Deck member types used for the FE model, including dimensions used for the raised deck model. In the modified model, the deck was raised 0.94 m, the stringers and car joists were raised 0.74 m, and the floor beam, walkway beams, walkway joists, and walkway deck elements were raised 0.22 m above the bottom chord centroid (see locations and properties listed in Table 4.3).

Table 4.3. Traffic Bridge member properties determined from original drawings.

Members	Member	Member Type (Fig. 4.3, Fig. 4.4)	Total Cross Sectional Area (mm^2)	Moment of Inertia I_y (10^6 mm^4)	Added Mass (kg/m)
Bottom Chord	L0L1	B,C	9316	48.9	12.5
	L1L2	C	9316	48.9	12.5
	L2L3	C	12258	65.4	14.8
	L3L4	C	15122	81.8	17
Top Chord	L0U1	A	22152	453.2	26.1
	U1U2	A	17206	386.3	23.2
	U2U3-U4	A	19581	419.7	24.6
Diagonals	U1L2	E	5394	1290.3	3.8
	U2L3	E	4413	1073.9	3.4
	U3L4	E	1884	70.7	2.4
Verticals	L1U1	B	4594	53.2	5.4
	others	D	5794	56.1	27.3
Bottom Bracing	L0L1	G	1652	113.2	0.6
	L1L2	G	1348	68.7	0.5
	L2L3	G	942	35.3	0.4
	L3L4	G	942	35.3	0.4
Top Bracing	U1U2	G	2697	1.4	1
	U2U3-U4	G	768	29.3	0.3
Portal Frames	T&B	E	3097	1.5	5.9
	x-bracing	G	768	29.3	0.15
Floor Beam	All	H	21855	1923.8	8.6
Car Joists	All	F	12387	491.2	2.4
Regular Joists	All	I	6032	90.7	1.2
Edge Joists	All	I	4187	49.1	31.7
Walkway Floor Beam	All	G	9735	2002.6	40
walkway joist	All	I	4594	586.8	45
Railing Post	All	n/a	3653	1.7	1.4
Railing handrail	All	n/a	3821	914.9	1.5
Dywidag Bars	All	n/a	548	n/a	n/a

**Li = i^{th} lower panel point numbered from south abutment*
**Ui = i^{th} upper panel point numbered from south abutment.*

4.3 MODIFICATIONS TO BASE MODEL

The assumptions made when constructing an FE model are not always representative of how the structure responds under loads. While it is common to assume pin/roller supports for a simple span bridge, for example, it may not behave as such (O'Connell and Dexter 2001). The timber deck of the Traffic Bridge (with asphalt overlay) was designed to carry the loads to the floor joists only, but in some cases,

bridge decks have been found to assist in transferring the tensile loads thought to be carried only by the bottom chord members to the supports (De Corte and Van Bogaert 2006). With heavy-class steel truss bridges such as the Traffic Bridge, it has been found that there is a significant level of structural redundancy (Nagavi and Aktan 2003) and that anticipated load paths may differ significantly from actual load paths.

To refine the model to match the measured results as closely as possible, selected modelling parameters were systematically altered one at a time, and finally in combination, to assess their influence on structural behaviour. The effects of altering support conditions, member connectivity, deck member elevations and section properties are outlined in the following sections. The influences of these modifications to the FE model are described in Chapter 5.

4.3.1 Modifications to Support Conditions

Although the bearings were replaced within the last 10 years, there is the possibility of bearing stiffening. This bearing stiffening could be caused by deterioration of the steel elements or debris clogging the system, resulting in resistance at the supports in the longitudinal direction. This resistance may induce compression forces into the bottom chord members, and could cause local buckling (Stantec 2006).

Springs of various levels of stiffness were added in the longitudinal direction to mimic bearing friction at all four supports (4-springs), as seen in Figure 4.5. By adjusting the spring stiffness, this could mimic partial bearing stiffening. The presence of springs could also approximate the case where there is play within the joints of the bottom chord. This 'play' could be due to deterioration in the connections, requiring a certain deflection to be experienced before the member becomes fully active to resist loads.

The ANSYS element COMBIN14 was used to model the springs. The massless element's nodes have translational degrees of freedom in the x, y, and z directions, and the element is only capable of resisting axial translations, not bending. The spring was modelled with a stiffness ranging from 1 MN/m to 100 MN/m. A damping coefficient was not used in conjunction with the spring.

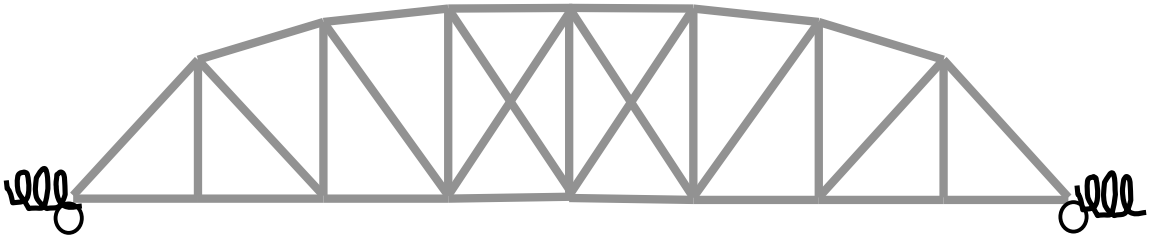

Figure 4.5. Modification to support condition: longitudinal restraints added to mimic bearing stiffening.

4.3.2 Modifications to Connectivity

Trusses are typically designed and analyzed as axial force members that experience only pure tension and compression forces. However, some moment transfer is expected to occur at the truss joints. The heavy gusset plates required to connect the heavy-class steel truss members result in some bending moment transfer at the connections. To model this effect, the rotational degrees of freedom of the adjoining members along the top and bottom chords were coupled (the rotations about each axis were forced to be equal) to allow moment transfer to occur. The expected amount of moment transfer occurring at other connections of members was not expected to be substantial because of the relative flexibility of these members in flexure; therefore, all other connections were modelled simply as pinned connections.

4.3.3 Modifications to Deck Member Elevations

The deck members included the floor beams, car joists (i.e., the joists positioned along the probable wheel paths), regular joists, edge joists, timber deck, walkway floor beams, walkway joists, and walkway deck, as depicted in Table 4.3 and Figure 4.4. These deck members were originally located at the centroidal elevation of the bottom chord members. The modified, raised deck model brought all deck members to the actual elevations of their respective geometric centroids. This was accomplished by the creation of zero-mass connector elements (ANSYS BEAM4 element) that connected the raised member to its supporting member below. The member properties of the connector elements were chosen to match those of the floor beam (excluding the mass), as shown in Table 4.3. The floor beam properties were chosen because it possessed the highest member stiffness in the FE model, and that stiffness was required to transfer loads to its supporting member. The top node of the fictional vertical connector was moment-connected (translational and rotational DOF's were coupled) to the supported

member above, while the bottom node of the connector was pin connected (translational DOF's only coupled). The deck vertical connectors were moment connected to the deck, while pin connected to the supporting joists and beams. Relative to the bottom chord centroid, the floor beams, walkway beams, walkway joists, and walkway deck were raised 0.22 m (8.5 in), the car joists and deck joists were raised 0.74 m (29 in), and the centre line of the deck elements was raised 0.94 m (37 in).

4.3.4 Modifications to Member Properties

4.3.4.1 Modifications to Deck Material Properties

Since there is a possibility that the deck may assist in relieving some of the tensile forces from the bottom chord members, the level of deck participation will depend on its stiffness. The original deck modulus of elasticity of 10,000 MPa was reduced in 10% increments to as low as 3,000 MPa and was also increased to 20,000 MPa and 30,000 MPa to determine the influence on bottom chord forces. The modulus of elasticity was also reduced to 1 kPa to track the load path in the virtual absence of the deck.

4.3.4.2 Modifications to Truss Member Properties

The first set of modifications was designed to test the possibility of alternate load paths at and below the deck level, which would become more important as the bottom chord deteriorates. This was accomplished by reducing the modulus of elasticity, shear modulus, and density of one bottom chord member by a common factor for the full length of the member to simulate section loss due to deterioration. The model was then analysed with only the one bottom chord member having reduced member properties. This process was repeated with each of the bottom chord members being given reduced properties on an individual basis. The material properties were reduced by 10%, 20%, 30%, 40%, 50%, 60% and 75% relative to their original values. The geometric properties did not need to be modified in order to represent the loss in cross-sectional area because the reduction in the modulus of elasticity produced the same effect for truss members. This was thought to be a satisfactory approach because, although different rates of corrosion are experienced throughout the member length, changes in load

distribution in this nearly determinate system can be related to an overall "effective" stiffness of each member.

Since the bottom chord members are composed of four angles bolted together with a separating plate, an FE model was constructed to replicate the behaviour should one of the four angles experience a differential reduction in member properties. The modulus of elasticity was therefore reduced for one of the four parallel members. The change in force distribution throughout the truss members resulting from this reduction in material properties was then observed. There is some uncertainty as to the accuracy of this aspect of the model, since in the field, the parallel members are bolted together at intervals along their length while, in the FE model, parallel members were not connected between their ends. However, if the parallel members act as a unit, there would not be a discrepancy between a change in strain values unless local damage at the strain gauge location occurred. Thus, the parallel members would be acting simultaneously and equally to resist the load, and the measured strain would be identical in each member.

The vertical, diagonal and top chord members' material properties were also reduced to mimic damage. Again, this reduction was performed for one member at a time, and the resulting axial force distribution (or change in force distribution) throughout the truss was observed.

4.3.4.3 Modifications to Floor Beam Stiffness

The floor beams run perpendicular to the main bridge trusses, and support the car joists and stringers. The lateral stiffness of the floor beams was modified in order to limit the tensile force transfer from the bottom chord members to the interior deck elements (stringers, car joists, and deck). The moment of inertia about the vertical member axis (i.e. about the weak axis of the beam) was reduced by 50%, 60%, 70%, 80%, 90%, and 95%.

4.4 LOADING SCENARIOS

Simulations were completed of the control load vehicle operating in both the downstream and upstream traffic lanes of the FE model corresponding to the static analyses. Each 7.62 m (25 ft) car joist was divided into eight elements of equal length to provide nodes at which to apply the truck axle weight. The axle loads applied at each

node are illustrated in Figure 4.6. The static analysis was performed with the rear axle aligned with each of the 7 interior panel points, which corresponded to the controlled loading test procedure, as described in Section 3.3.2. The front axle estimated load of the vehicle was then divided between the closest nodes based on the relative distance between the front wheel position and the adjacent nodes, as shown in Figure 4.6. The weight distribution of the front axle was 80%-20% to the fourth and fifth nodes from the panel point, respectively, based on the geometry. The uncertainty in the weight distribution is a source of possible error. The measured truck weights obtained during testing can be found in Appendix B, while the resulting axial forces from the FE simulations of the controlled loading scenarios can be found in Appendix D.

In addition to the static and transient analyses, a modal analysis was also performed to extract the natural frequencies (eigenvalues) and mode shapes (eigenvectors) of the structure. A Block Lanczos method which internally uses the QL algorithm was used for this analysis (Release 11 Documentation for ANSYS). This modal analysis was completed to compare and calibrate the dynamic characteristics of the model to the measured dynamic characteristics (obtained as described in Section 3.5.2) in order to ensure the accuracy of the model. Due to the large walkway cantilever on the upstream side of the bridge, the system was highly sensitive to the mass of the walkway and walkway elements. As a result, the estimated walkway element added mass was adjusted until the modelled response correlated well to the measured natural frequencies and mode shapes.

Figure 4.6. Control vehicle node loads for transient analysis.

5 RESULTS

5.1 INTRODUCTION

A summary of results from the field and numerical studies is presented in this chapter. The measured strain-time histories were investigated to determine the structural load paths and redundancy within the Traffic Bridge, as well as possible methods of detecting incremental damage. The results from the numerical model trials are then compared to the measured results to determine the accuracy of the FE model, and to evaluate the most effective modelling parameter assumptions to simulate the measured response.

The strain-time histories obtained from the instrumented members under controlled loading scenarios are examined first. The strain-time histories from the 72 strain gauges were investigated to determine the structural response under transient loading, both at a local and global scale. From a local scale perspective, the strain distribution between the individual angles, channels, or plates that make up a built-up truss member were considered. The global scale refers to the load distribution throughout the entire structure, including a comparison between corresponding members of the upstream and downstream trusses within the instrumented span; the dynamic characteristics are also an indicator of global behaviour.

A discussion of the numerical results follows, comparing the FE model structural behaviour to the measured structural response with regards to the controlled loading scenario axial force–time histories. Finally, the dynamic response under ambient (uncontrolled) loading is investigated.

5.2 STRAIN MEASUREMENTS

5.2.1 Dynamic Amplification Effects

To compare the measured response to the FE model, the effects of dynamic amplification are explored in this section. Other measurement considerations, such as the strain distribution between gauges at a specific location, strain distribution amongst members, and the nominal force associated with the measured strain are discussed in Section 5.2.2. Dynamic amplification refers to the amplification of the response due to

the dynamic excitation by vehicles, which may increase with increasing vehicle speeds. Dynamic amplification values are useful for the analysis of new and existing structures to obtain a realistic estimate of peak axial forces based on a known maximum vehicle weight. A low-pass filter, with a cut-off frequency below the lowest natural frequency of the bridge, can be used to isolate the quasi-static component of the response from the total dynamic response.

The dynamic amplification factors (DAF) for the controlled loading scenarios, *i*, are presented in Table 5.1. These values were obtained by dividing the averaged peak member force $(F_m)_{i\_max}$ by the subsequent averaged peak static force $(F_m)_{static\_j}$ for a particular loading scenario.

$$DAF_i = \left(\frac{F_m}{F_{static}} \right)_{i\_\max} \quad \{5.1\}$$

To clarify, there were three identical trials, *j*, completed for each controlled loading scenario. The peak measured axial force, $(F_m)_{i\_max}$, was taken as the average of the peak values experienced during each of these identical trials, with the calculated forces being equal to the nominal cross-sectional area (A_n), multiplied by the modulus of elasticity (E) and the peak measured strain $(\varepsilon_m)_{i\_max}$ for the controlled loading scenario, as shown in Equation {5.2}.

$$\left(F_m\right)_{i\_\max} = A_n \cdot E \cdot \left(\varepsilon_m\right)_{i\_\max} \quad \{5.2\}$$

where,

$$\left(\varepsilon_m\right)_{i\_\max} = \frac{1}{3}\left(\sum_{j=1}^{3} \left(\varepsilon_m\right)_{j\_\max} \right)_i \quad \{5.3\}$$

The bottom and top chord members sustained, on average, little or no dynamic amplification, with averaged DAF factors remaining at 1 for most cases. The exception to this trend was seen for the southbound controlled loading scenario at a vehicle speed of 30 km/hr, with an averaged DAF factor of 1.1. The vertical and diagonal members experienced a slight reduction in response amplitudes under dynamic loading, with an overall averaged DAF reduction for all vehicle speeds of 0.9.

The DAF factors from this study correspond well with the results from previous studies on truss bridges. O'Connell et al. (2001) indicated that only the tension members of the truss experienced a DAF factor of 1.1, while Laman et al. (1999)

indicated that there was no amplification of member forces with an increase in vehicle speed. The amplification factors in the current study were slightly larger than 1.0 in the bottom chord (tension) members, while very little change occurred in the other truss members. The amplification factors were found to be small; therefore, the averaged measured values from the three identical controlled loading scenarios were subsequently used to compare with the FE model without dynamic amplification effects.

Table 5.1. Peak dynamic amplification factors and coefficient of variation (COV) values for the controlled loading scenarios.

	20 km/hr Vehicle Speed				30 km/hr Vehicle Speed				50 km/hr Vehicle Speed			
Member	north	COV	south	COV	north	COV	south	COV	north	COV	south	COV
L0L1-BCa$_d$	1.1	8%	1.0	7%	1.0	6%	1.1	3%	1.0	6%	0.9	7%
L0L1-BCb$_d$	1.0	7%	1.0	10%	0.9	6%	1.1	4%	0.9	6%	0.9	8%
L1L2-BC$_d$	1.0	8%	1.0	11%	0.9	6%	1.1	5%	0.9	6%	0.9	3%
L2L3-BC$_d$	1.0	5%	1.0	4%	0.9	6%	1.0	4%	0.9	6%	1.0	1%
L0L1-BC$_u$	1.1	9%	1.1	8%	1.1	4%	1.1	4%	1.1	4%	1.0	3%
L2L3-BC$_u$	1.1	1%	1.0	11%	1.0	3%	1.0	5%	1.1	3%	1.0	2%
BC Avg.	1.0	6%	1.0	9%	1.0	5%	1.1	4%	1.0	5%	1.0	4%
L0U1-TCa$_d$	1.0	6%	0.9	5%	1.0	2%	0.9	7%	0.9	2%	0.9	4%
L0U1-TCb$_d$	1.0	5%	1.0	4%	1.0	3%	0.9	11%	0.9	3%	1.0	0%
U2U3-TC$_d$	1.0	4%	1.0	5%	1.0	3%	1.0	5%	0.9	3%	1.0	3%
U2U3-TC$_u$	1.1	3%	0.9	4%	1.0	4%	1.0	4%	1.1	4%	1.0	1%
TC Avg.	1.0	5%	1.0	5%	1.0	3%	1.0	7%	1.0	3%	1.0	2%
L1U1-V$_d$	0.9	5%	0.9	14%	0.3	30%	0.9	9%	0.8	30%	0.9	3%
L2U2-V$_d$	1.1	6%	0.9	6%	1.1	4%	0.7	15%	1.0	4%	0.9	3%
U1L2-D$_d$	0.9	7%	1.1	6%	0.9	2%	1.0	7%	0.8	2%	1.1	2%
D & V Avg.	0.9	6%	1.0	9%	0.8	12%	0.9	10%	0.9	12%	0.9	3%

5.2.2 General Characteristics of Truss Member Strain Results

Strain-time histories of the bottom chord, top chord, vertical and diagonal truss members, as well as those of the floor joists, are explored below. Analyses of the measured responses at local and global scales are completed in this section; correlation of the results to the FE model is presented in Section 5.3. For a thorough description of strain gauge placement and locations, see Chapter 3.

5.2.2.1 Bottom Chord Strain Gauge Results

The strain distribution among the gauges on individual structural components of the composite member at an instrumented location is of interest to determine if bending

occurs during loading and also to establish a baseline for future monitoring. Theoretically, each of the strain gauges on a member should experience very similar readings, since truss members are designed to experience axial loads only, and since the component members are expected to share the load. However, non-uniform deterioration of the component members and the subsequent connections could result in a range of peak strain readings in the various components. Example strain time histories shown in Figure 5.1 display the strain measurements from each gauge at the indicated instrumented locations along the bottom chord of the bridge truss for a controlled loading trial with the truck travelling north at 30 km/hr. This controlled loading scenario was chosen to represent the results more generally observed, as the results from other loading events showed similar trends.

All but two of the bottom chord strain gauges included in Figure 5.1 provided good, uninterrupted measurements. The two strain gauges that did not provide good readings were located on member L0L1-C_d and are omitted from Figure 5.1 (b). One strain gauge did not provide a response (zero-amplitude) and the other had an interrupted signal (strain amplitude some of the time, combined with zero amplitude response at other times). Therefore, only the two functioning gauges for that location (i.e., those that provided uninterrupted signals) were used in the subsequent analyses. The remaining strain gauges on other bottom chord members provided good, continuous signals for all loading trials and were thus included in the analyses.

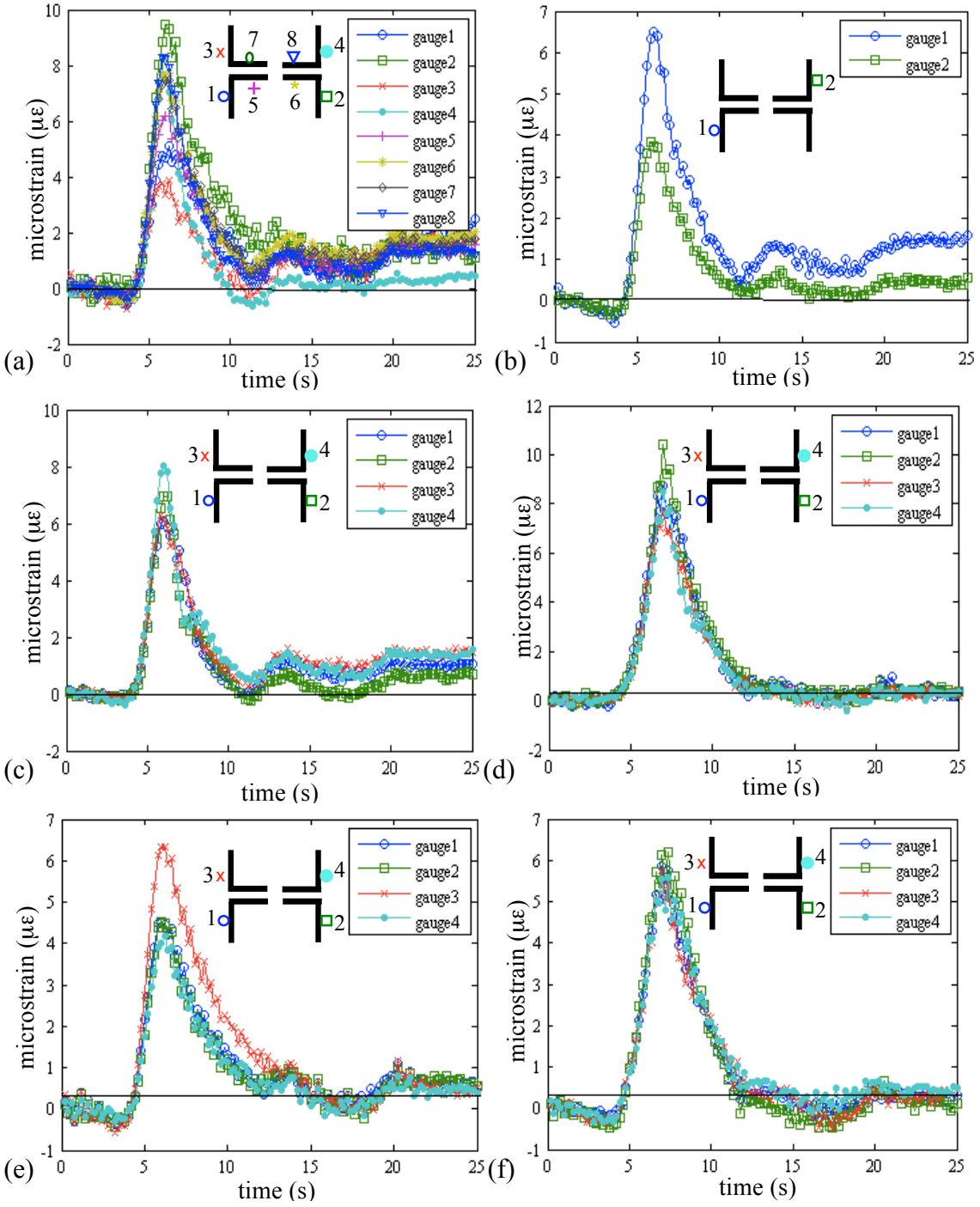

Figure 5.1. Strain-time history for instrumented bottom chord members for 30 km/hr northbound control vehicle: (a) member L0L1-B_d; (b) member L0L1-C_d; (c) member L1L2-C_d; (d) member L2L3-C_d; (e) member L0L1-C_u; (f) member L2L3-C_u.

As can be seen in Figure 5.1, measured strain amplitudes at companion gauges at a given location varied to some degree. The difference between strain readings in the various components of a member could be due to bending, uneven load distribution to the members at the panel points, or redistribution due to member section loss caused by corrosion. For example, the strain-time history shown in Figure 5.1 (a) and (c) suggests that members L0L1-B_d and L1L2-C_d may be subject to bending about the vertical member axis, since the gauges on the downstream side of the member have a higher strain amplitude than the gauges installed on the upstream side of the member, assuming that the component cross-sectional areas are uniform. Discrepancies in strain plots in Figure 5.1 (d) and (e) may suggest that Member L2L3-C_d and L0L1-C_u could be experiencing a higher degree of deterioration in one of the four components due to the higher amplitudes indicated by only one strain gauge. In contrast, as shown in Figure 5.1 (f), member L2L3-C_u features an even distribution of axial load to all components, assuming that the cross-sectional areas are uniform. To obtain the measured axial force of the bottom chord members, the instantaneous (i.e., not averaged over time) strain values at each of the gauge locations on a member were averaged.

As suggested in the discussion above, any observations concerning the member strain distributions are open to interpretation because it is impossible to measure the cross-sectional areas to verify member forces. However, the relative levels of strain in member components provide an indication of the effective participation of the components. In order to use these data in a future SHM system, therefore, a baseline strain distribution was obtained to compare with future measurements. For each controlled loading event, the peak strain amplitude of each gauge ε_i, was divided by the sum of the peak strain amplitudes of all gauges at an instrumented location to obtain the normalized instantaneous strain, $\lambda_{\varepsilon i}$:

$$\lambda_{\varepsilon i} = \frac{\varepsilon_i}{\sum_{j=1}^{n} \varepsilon_j} \qquad \{5.4\}$$

The strain distribution between the gauges at an instrumented location can then be used as a baseline, and any change from that baseline in the strain distributions recorded with

future measurements could indicate the presence of damage either at the members instrumented, or the connections of the members.

The strain distributions for the bottom chord members are summarized in Table 5.2. With the exception of the instrumented location L0L1-Ca, the strains appeared to be evenly distributed. The strain distribution factors for the northbound controlled loading scenarios differed only slightly from the southbound controlled loading scenarios. The average coefficient of variation (COV) for all loading events and instrumented locations was 6%. This low COV indicates a good level of reliability in the baseline strain distributions to be used as a comparison with future measurements in an SHM system.

One general observation was that the strain-time histories for gauges on each of the bottom chord members did not immediately return to zero once the truck left the instrumented span at approximately 12 seconds after the start of the loading event, as illustrated in Figure 5.1. De Corte and Bogaert (2006) also observed similar behaviour and suggested that it was due to the deck behaving as a membrane to resist the tensile loads. Further explanation is not given in their article, but it is assumed that for the deck to participate, deflection must occur throughout the entire deck and that the deck does not immediately return to its undisturbed state after the vehicle passes, but takes a few seconds to do so. While the non-zero strain reading is suspicious, it is questionable as to whether it is due to the deck acting as a membrane. For the deck to act as a membrane resisting only tensile loads, it should be reducing the tensile forces in the bottom chord and not increasing it for a few seconds once the vehicle is past the span. Perhaps the deck is acting as the compression part of a beam, in which case the bottom chord members would have an elevated tensile strain readings when the control load vehicle is just past the span. Another possible way to interpret this behaviour is that the deck acts as a viscoelastic material that slowly loses strain after being unloaded: the deck experienced compressive forces, so the bottom chord members had an elevated tension force after being unloaded due to the slow loss of compression stresses in the deck. However, this behaviour was not mimicked in the analysis results from the FE model, which did not consider the deck to be viscoelastic.

Table 5.2. Bottom chord strain distribution factors for the northbound and southbound controlled load scenarios.

Location	Gauge	Northbound	COV	Southbound	COV
L0L1-B	1	0.10	8%	0.09	11%
	2	0.16	6%	0.13	8%
	3	0.08	10%	0.13	30%
	4	0.14	6%	0.13	4%
	5	0.11	6%	0.10	7%
	6	0.14	6%	0.15	6%
	7	0.13	6%	0.12	5%
	8	0.14	7%	0.15	4%
L0L1-Ca	1	0.62	7%	0.62	8%
	2	na	na	na	na
	3	na	na	na	na
	4	0.38	7%	0.38	7%
L1L2-Ca	1	0.22	7%	0.24	4%
	2	0.26	7%	0.23	5%
	3	0.22	5%	0.24	6%
	4	0.30	7%	0.29	3%
L2L3-Ca	1	0.25	5%	0.27	7%
	2	0.29	5%	0.28	3%
	3	0.22	5%	0.23	5%
	4	0.24	5%	0.23	3%
L0L1-Cb	1	0.23	4%	0.21	4%
	2	0.24	6%	0.24	5%
	3	0.32	4%	0.31	4%
	4	0.22	6%	0.23	5%
L2L3-Cb	1	0.25	5%	0.25	5%
	2	0.27	6%	0.26	4%
	3	0.25	7%	0.26	3%
	4	0.23	5%	0.24	5%

5.2.2.2 Top Chord Strain Gauge Results

The strain-time history of the top chord members is shown in Figure 5.2 for a northbound controlled loading scenario with a constant speed of 30 km/hr. The blue (○-marker) and green (❑-marker) lines represent the strain gauges at mid-height on the sides of the channels, while the red (x-marker) line represents the single strain gauge on the top of the plate that is bolted on top of the channels. The strain-time history in Figure 5.2 (a) shows that one strain gauge placed on a channel of member L0U1-Aa_d

experienced a slightly higher strain than the others, but the existence of bending could not be concluded about either axis due to a lack of linearity (the strain distribution did not follow a consistent proportional relationship during the measurement period). Therefore, the member forces calculated subsequently were calculated by simply averaging the strain measurements. However, member L0U1-Ab_d, shown in Figure 5.2 (b), appears to experience bending about the vertical axis, so the strain readings were simply averaged to obtain the member average axial force since the gauges on the channels were equidistant from the vertical bending axis. For the upstream and downstream top chord members in the third panel, U2U3-A_d and U2U3-A_u, as shown in Figure 5.2 (c) and (d), the strain readings were also simply averaged to obtain the member axial force due to very similar readings in all gauges at the various instrument locations, as shown by the strain distributions in Table 5.3.

Unlike the bottom chord members, the top chords only experienced a live load strain reading from the moment the truck entered the span (at 4 seconds) to when the truck left the span (at 12 seconds). The top chord members did not have elevated strain amplitudes after the truck was past the span, as the bottom chord members experienced. This is likely due to a lack of alternate load paths at the level of the top chord members that would be capable of transferring load to (or from) the top chord, unlike the situation with the deck and the bottom chord members. This again suggests some degree of redundancy experienced with the members at and below the deck level.

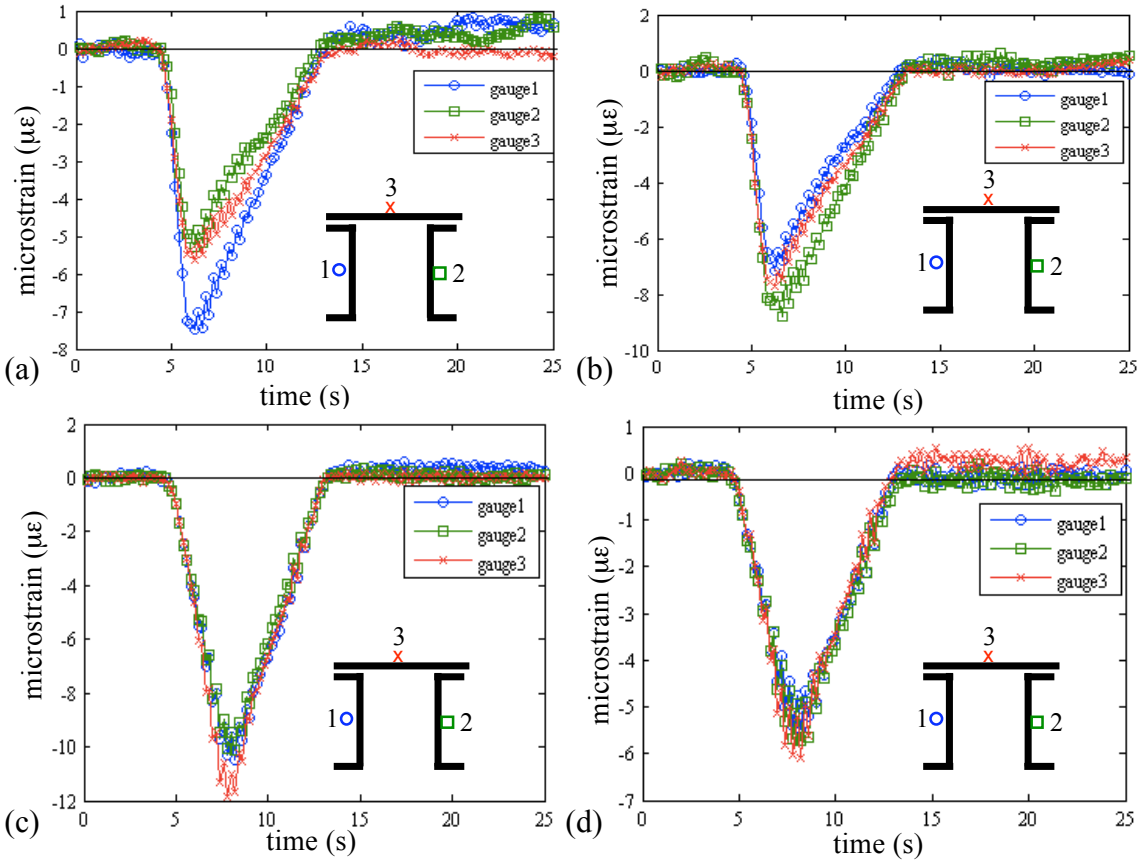

Figure 5.2. Strain-time history of top chord members for the 30 km/hr northbound control load scenario: (a) member L0U1-Aa_d; (b) member L0U1-Ab_d; (c) member U2U3-A_d; (d) member U2U3-A_u.

Based on the strain-time histories, it appears as though the top chord members do not participate in providing alternate load paths, and behave as statically determinate members. Any change in stiffness of the top chord members will therefore not affect the load distribution throughout the structural system. Because the existing condition of the top chord members is deemed to be good, based on field observations (Stantec 2005), it is likely unnecessary to monitor the relative strain distribution between the strain gauges at the top chord locations. In other bridges, however, there has been evidence of compressive failure in the end posts (such as member L0U1, the top chord member that terminates at the supports), due to corrosion occurring between the top plate and the adjoining channels (Bahkt 1990). In order to detect this type of failure, monitoring the peak strain distribution among the elements making up the composite section of the top chords may be prudent, in addition to what is done for the bottom chords. The strain

distribution of the top chord elements are outlined in Table 5.3, along with the COV values for those distributions.

Table 5.3. Top chord peak strain distribution factors for the northbound and southbound controlled loading scenarios.

Location	Gauge	Northbound	COV	Southbound	COV
L0U1-Aa_d	1	0.47	22%	0.36	30%
	2	0.31	37%	0.33	37%
	3	0.22	31%	0.32	27%
L0U1-Ab_d	1	0.32	18%	0.27	50%
	2	0.45	31%	0.43	43%
	3	0.23	42%	0.30	44%
U2U3-A_d	1	0.36	37%	0.37	33%
	2	0.31	42%	0.31	41%
	3	0.34	37%	0.32	49%
U2U3-A_u	1	0.33	37%	0.32	53%
	2	0.32	42%	0.34	64%
	3	0.35	37%	0.34	65%

It was expected that the top chords in the third panel (U2U3) would be primarily resisting compression forces, while the top chord/end post (L0U1) would be experiencing compression and slight bending in the lateral direction due to the frame installed below the top panel point to limit lateral deflection. This behaviour would result in a uniform peak strain distribution between the gauges instrumented at the third top chord panels (U2U3), and varying peak strain distributions between the gauges instrumented at the end post (L0U1). As shown in Table 5.3, the peak strain distributions for the third top chord panel were fairly uniform, verifying the expected behaviour of resisting compression forces only. The end post (L0U1) experienced bending about the vertical axis. The COV is slightly larger with the top chord members compared to that of other instrumented members. The reason for the higher COV value is uncertain, as the strain amplitudes experienced by the top chords were similar to those of other instrumented members (from 4 με to 30 με).

5.2.2.3 Vertical and Diagonal Member Strain Gauge Results

The strain-time histories for the two vertical members (L1U1-D_d and L2U2-D_d) and a single diagonal member (U1L2-E_d) are shown in Figure 5.3. From the varying levels of recorded strain in a given member, it appears that bending was present in both

vertical members, as well as in the single diagonal member instrumented. However, the strain differential in the single diagonal member was small, and may be due to experimental variation. Due to the symmetrical placement of the strain gauges, the resulting axial force was found by averaging the strains recorded at all gauges at a particular cross section in all cases. The pristine cross-sectional areas were used in the axial force calculations with a high degree of confidence because the members did not exhibit any visual signs of corrosion at the instrumented locations.

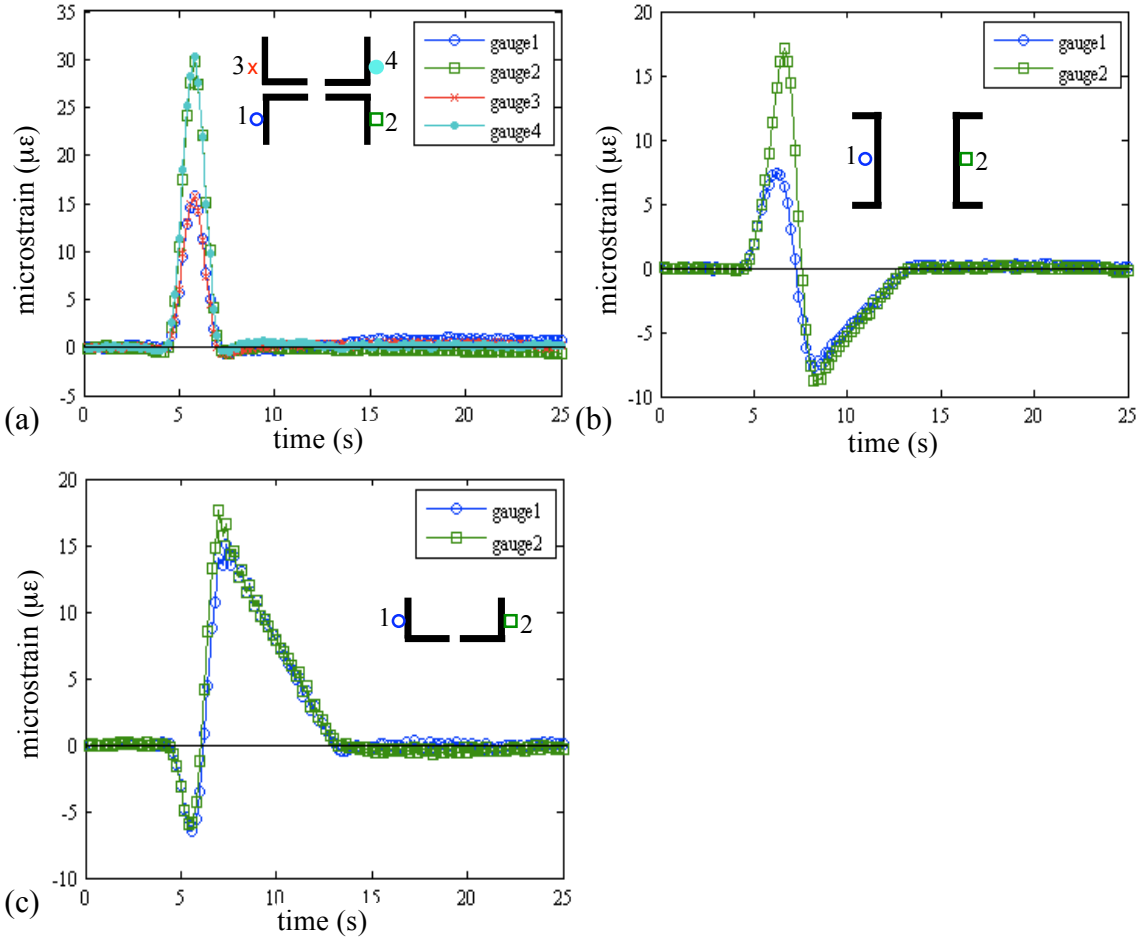

Figure 5.3. Strain-time history of vertical and diagonal members for a 30 km/hr northbound control load scenario: (a) member L1U1-D_d; (b) member L2U2-D_d; (c) member U1L2-E_d.

The bending present in the measured strain time histories in Figure 5.3 should not actually be present in the nominally pin-connected vertical and diagonal members. It is possible that the deterioration of the lower connection could cause an eccentricity in the joint, and result in an unintentional difference in the measured strains of the composite elements of a member, or simply cause a change in the load distribution

between the components of the member. Also, some moment transfer could be occurring at the gusset plate connections. Table 5.4 displays the peak strain distribution factors for the instrumented vertical and diagonal members. Unlike the bottom chord member peak strain distribution factors, there is a substantial difference between the northbound and southbound controlled loading scenarios for the vertical members L1U1-D_d and L2U2-D_d. The diagonal member, on the other hand, experienced no change between the northbound and southbound distribution factors. The observed directional differences are likely due to the bending that the vertical members appear to be experiencing.

Table 5.4. Vertical and diagonal strain distribution factors.

Location	Gauge	Northbound	COV	Southbound	COV
L1U1-D	1	0.17	8%	0.11	12%
	2	0.33	5%	0.38	5%
	3	0.17	8%	0.11	9%
	4	0.33	5%	0.39	6%
L2U2-D	1	0.31	8%	0.17	18%
	2	0.69	5%	0.83	4%
U1L2-E	1	0.46	6%	0.46	9%
	2	0.54	6%	0.54	3%

5.2.2.4 Floor Joist Strain Gauge Results

In a purely statically determinate 3D truss system, the deck and supporting members (car joists, stringers, floor beams) only act to transfer the deck loads to the truss by flexural action. However, the deck members can provide a potential alternate load path for tension at the bottom chord level, depending on the added stiffness that those members provide, due to the continuous nature of the deck possibly permitting membrane action. The floor joists were therefore instrumented to capture evidence of an alternate load path for tensile forces in the bottom chord members.

For a 30 km/hr control vehicle headed northbound, Figure 5.4 displays the strain-time history for the downstream deck joists in the first panel and the second panel (for instrumentation layout, see Chapter 3). The red (x marker, 150 mm above the middle gauge), green (□ marker, middle gauge) and dark blue (○ marker, 150 mm below the middle gauge) lines, respectively, depict the strain gauges on the deck joist in panel 1.

The yellow (* marker, top gauge), pink (+ marker, middle gauge), and light blue (● marker, bottom gauge) lines depict the strain gauges on the deck joist in the second panel, also shown from highest in elevation to lowest.

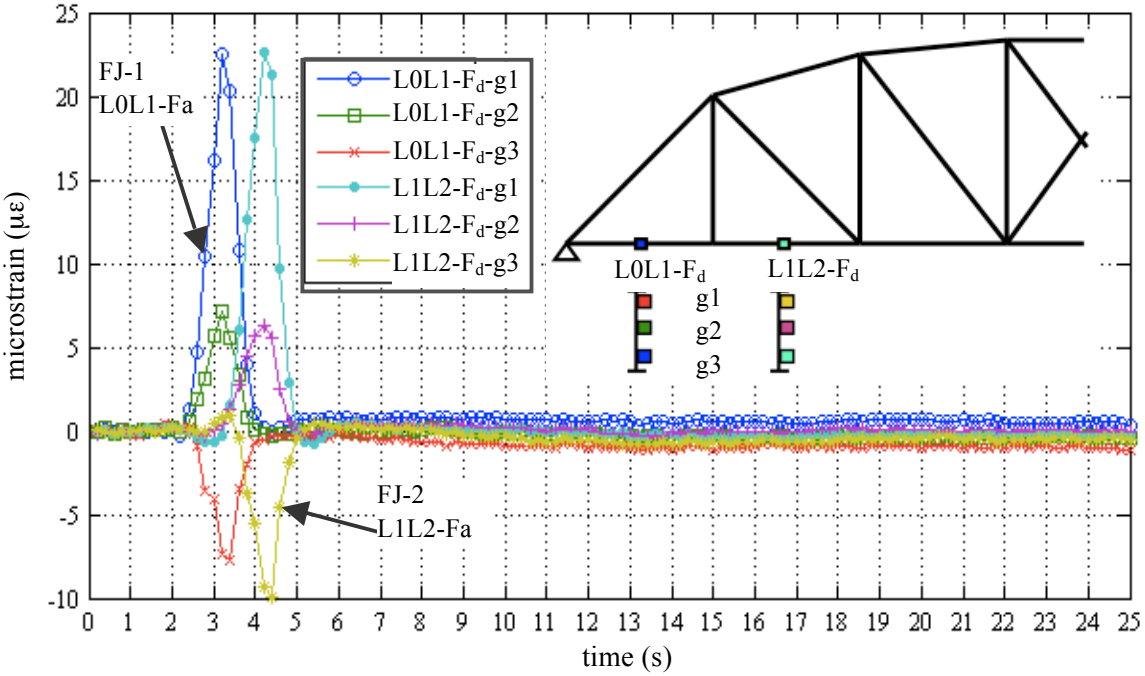

Figure 5.4. Strain-time history of the downstream deck joists in panels 1 and 2.

For the case considered, the front axle of the truck entered the span at approximately 2.5 seconds and the rear axle left the first panel at 4.5 seconds. The front axle then entered the second panel just after 3.5 seconds, and the rear axle left the second panel by about 5.5 seconds.

Figure 5.4 illustrates that the deck joists experience bending about their horizontal axis, with the neutral axis located between the top and middle strain gauges. The fact that the neutral axis is located above the joist centroid, as indicated by the tensile strains in the middle gauges, and that the bottom peak strain values have a greater amplitude than the top gauge values at both instrumented locations, indicates that the timber deck contributes by means of composite action to resist some of the flexural compression forces. Given the observation that the deck joist strain gauges immediately return to a strain value very close to zero once the truck is past the panel, it appears unlikely that the deck joists contribute significantly to resist axial tensile forces at the bottom chord level, at least for the transient loads.

For further analysis, a linear-regression analysis was applied to the instantaneous strain measurements of the three vertically aligned strain gauges at each instrumented location on the car joists. The instantaneous strain profile was calculated using the best-fit line between measured strains from the car joist strain gauges, resulting in an estimate of the neutral axis location and curvature at each sampling interval. The instantaneous axial force and bending moments were not calculated because the car joists were found to act compositely to resist loads with the deck, for which accurate composite member properties could not be estimated. The neutral axis location was plotted with respect to time, as shown in Figure 5.5; in addition, the curvature is plotted with respect to time in Figure 5.6. The calculations used to apply the linear-regression to the data can be found in Appendix C.

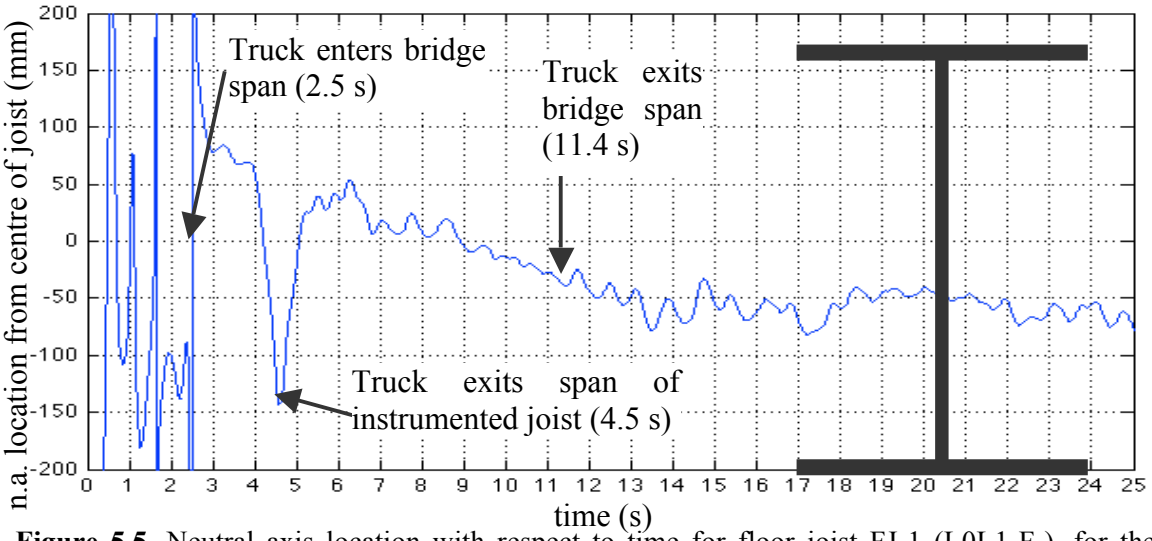

Figure 5.5. Neutral axis location with respect to time for floor joist FJ-1 (L0L1-F_d), for the northbound, 30 km/hr loading scenario (W3).

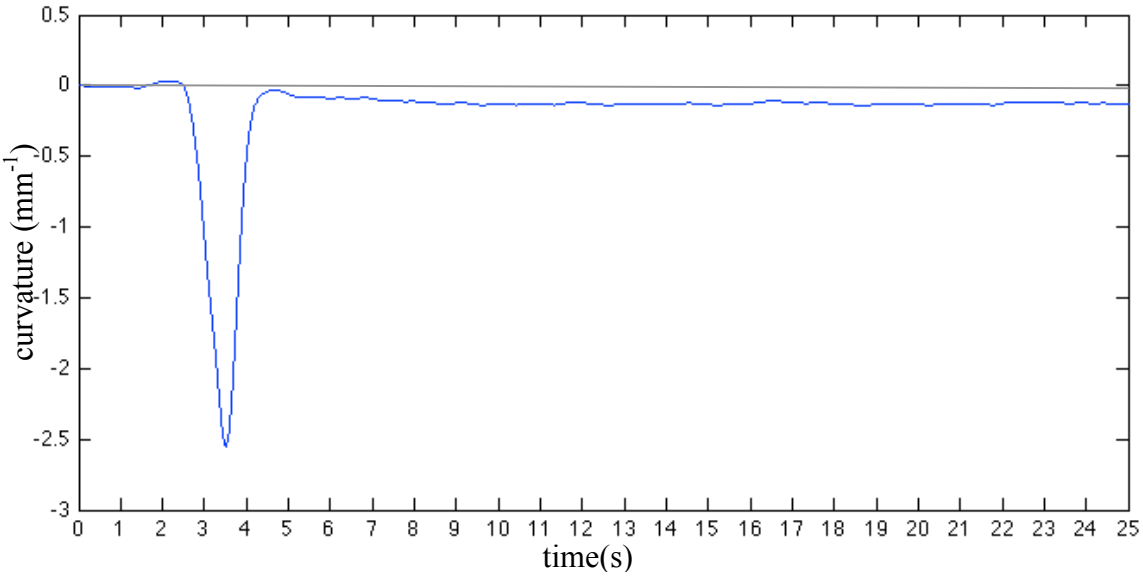

Figure 5.6. Car joist curvature-time history for a 30 km/hr northbound controlled loading scenario (W3).

The neutral axis location of the deck joists did not remain at a constant location, as it should have if the joist was subject to bending only, without the presence of axial loads. As indicated in Figure 5.5 for the joist in the first panel of the instrumented span, the truck entered the span of the bridge at approximately 2.5 seconds, leaving the first panel at 4.5 seconds and the span at approximately 11.4 seconds. Prior to the measured time of 2.5 seconds, the instrumented bridge span was empty (only dead loads acting), so theoretically the neutral axis location should have remained constant with respect to time. However, during the first 2.5 seconds of the signal, the truck was moving along the first span of the bridge (not the instrumented span), and could have been inducing compression in the floor joists due to the longitudinal friction from the truck wheels. The noisy signal of neutral axis location up to 2.5 seconds was likely due to having near-zero strain measurements, making the linear regression analysis unreliable. The neutral axis location was approximately 75 mm (3 in) above the mid-height of the joist while the vehicle was within the span of the instrumented member (L0L1-F_d). The neutral axis location then dropped to approximately 125 mm (5 in) below the mid-height of the joist and recovered to 50 mm (2 in) above the mid-height of the joist within the first second after the truck exited the instrumented joist (L0L1-F_d). This drop is likely due to the un-loading of the joist once the vehicle exited the span of the instrumented joist, in effect reversing the bending loads temporarily. The neutral axis then dropped linearly to a

height of approximately 50 mm (2 in) below the geometric centre of the joist once the vehicle was off the bridge span for approximately 2 seconds.

The shift in neutral axis location could also be due to a change in the degree of composite action between the deck and the joist as the truck moves along the span. For example, while the truck is directly above the joist, the increased friction would provide a higher level of composite action. Alternatively, when the truck exits the panel, the friction between the deck and joist elements reduces, thereby reducing the composite action, and effectively causing the neutral axis to fall.

To determine the reliability of the estimated location of the neutral axis, the average correlation coefficients were calculated from the linear regression line fit through the instantaneous strain measurements for four stages of the controlled loading scenario. The correlation coefficients are listed in Table 5.5 for when the truck was (a) not yet on the span, (b) over the instrumented panel, (c) on the bridge span, and (d) past the span. Prior to the truck entering the span, a low correlation coefficient was expected due to the near-zero strain readings recorded during that stage; this was validated by the results, with correlation coefficient values of 0.24, -0.01, -0.04, and 0.04 at the four instrumented locations. Correlation coefficients near unity were found for car joist L0L1_Fa while the truck was on that specific panel, indicating a linear relationship between the strain readings from the three gauges at that location. The correlation coefficient for that member then dropped to 0.99 once the truck passed the panel, which still represents a good fit. The other three instrumented car joists produced very low correlation coefficients, even when the truck was on the instrumented panel. This low correlation could either indicate a high level of noise in the signal, preventing an accurate analysis to determine how much axial tensile force the car joists relieved from the bottom chord members, or it could also indicate a fairly uniform level of strain in the three gauges, because, with a slope near zero, the correlation coefficient would also result in a low value.

Table 5.5. Car joist neutral axis correlation coefficient of line through strain readings for the 30 km/hr northbound controlled loading scenario (W3) before the truck enters the span, while the truck is on the instrumented panels, after the truck leaves the instrumented panel but is still on the span, and after the truck leaves the span.

	Correlation Coefficient			
Car Joist	before	panel	span	after
L0L1_Fa	0.24	1.00	0.99	0.99
L0L1_Fb	0.01	0.72	0.82	0.95
L1L2_Fa	0.04	0.04	0.36	0.54
L1L2_Fb	0.04	0.04	0.60	0.90

Since it is apparent from Figure 5.4 that the car joists experience bending when directly loaded by the control vehicle, the time history of the curvature is useful to determine if the car joists experienced bending when the vehicle was not directly loading the joist. It is shown in Figure 5.6, that the curvature was zero until the control vehicle passed over the instrumented car joist. This implies that the beam underwent bending primarily due to direct loading. It should be noted that only transient load effects could be detected through the gauges, so dead load effects could not be evaluated.

In summary, from the measurements it was inconclusive as to whether the deck members act to resist the tensile loads. The change in neutral axis location as the truck moved along the span suggests that the joists resist some of the axial tensile forces. However, the joist response was primarily one of bending under live loading. To what degree the joists and deck participate in resisting the self-weight of the structure remains uncertain.

5.3 MODELLED RESULTS

5.3.1 Overview

A number of modelling parameters were systematically varied in an attempt to improve the agreement between calculated and measured responses. The calculated forces can also be thought of as theoretical forces that were obtained from the FE model. The measured response was obtained by using the strain data and an assumed pristine cross-sectional area of truss members (see Section 3.5). It is important to note that the accuracy of the measured response relative to the actual response is dependant on having an accurate estimate of the cross-sectional area of the instrumented member.

The instrumented bottom chord members were the primary focus of this section. The other instrumented truss members (top chords, verticals, and diagonal) were found to experience a negligible change in axial forces due to variations in the modelling parameters investigated, and hence are not addressed in this section. In order to calibrate the FE model in a systematic manner, the measured, original FE model, and modified FE model axial forces are plotted on the same graphs, with one modelling parameter of interest varied per figure.

The modelling parameters examined included the support conditions, member connectivity, deck element elevations, deck stiffness, floor beam stiffness and truss member properties (as described in Chapter 4). The effects of modifications to the FE model were examined to determine what model best represented the actual structural system with respect to static load transfer (as inferred from measured strains from the controlled loading scenarios), as well as the mode shapes and natural frequencies (as inferred from the accelerometer measurements under ambient loading scenarios). The measured strains included the response to the live loads produced by the controlled loading scenarios only, which was limited by the posted vehicle load restriction of 5 tonnes.

Since one objective of this study was to determine how the structure is effectively behaving in the transfer of loads to the supports, the effectiveness of the post-tensioning (PT) system was also explored. Because the strain gauges were installed after the installation of the PT system, and the PT bars themselves could not be instrumented, the PT effects could only be studied using the FE model.

It should be noted that the FE model simulated the controlled loading scenarios by placing the rear axle of the control load vehicle on the interior panel points only (L1 to L7). Appendix D contains the measured and modelled axial forces for the controlled loading scenarios discussed in this section.

5.3.2 Bottom Chord Measured Results vs. Model Modifications

It was found that modifying the modelling parameters (as described in Section 5.3.1) resulted in little or no change in the axial load distribution throughout the upper truss members. Therefore, the results obtained from the model modification studies are focused primarily on the change in load distribution within the bottom chord members.

The following results are compared to the original model in all cases. The general description of all modifications to the FE modelling parameters is located in Chapter 4. The root-mean-square method (rms) was used to calculate the difference between modelled and measured axial forces. This method was chosen to capture the overall *difference* in response between the measured force, F_S, and the modelled force, F_M, at all loaded panel points, i, for each instrumented member as:

$$rms\_difference = \sqrt{\frac{\sum_{i=1}^{n}(F_S - F_M)_i^2}{\sum_{i=1}^{n}(F_S)_i^2}} \qquad \{5.5\}$$

where n is the number of panel points. Therefore, a lower rms difference value would indicate a better fit. This method was also used to calculate differences between various FE models. The measured strain used to calculate the measured forces can be found in Appendix E.

5.3.2.1 Modifications to Support Conditions

The support conditions were modified to investigate the influence of possible partial fixity of the nominal pin and roller supports. This was accomplished by introducing a spring at each of the four supports to resist movement in the longitudinal direction, emulating partial bearing seizure. As described in Section 4.3.1, the spring stiffness was varied from 1 MN/m to 100 MN/m.

In Figure 5.7 (northbound) and Figure 5.8 (southbound), the calculated axial forces in selected bottom chord members are plotted versus panel point location of the control truck for various spring stiffness values. As the spring stiffness was increased, the bottom chord axial forces decreased in all bottom chord members consistently; in fact, for very stiff support springs, some members are seen to go into compression when the modelled control vehicle is located at some positions.

The general shapes of the axial load diagrams in Figure 5.7 do not change with an increased support stiffness, with the exception that the axial load changes from tension to compression in bottom chord members near the supports when the load is located at the far end of the span; the compressive forces become slightly more amplified than the tensile forces. This means that, with increased spring stiffness, the

peak tensile force reduces slightly, while the peak compressive force increases substantially (see Figure 5.7). The general shapes, if not the amplitudes, of the graphs in Figure 5.7 match those of the measured shapes, with the exception of member L0L1-C_u northbound.

Generally, the measured plots have greater amplitudes than the corresponding modelled forces. This could be due to the fact that the remaining net section of the bottom chord members at the instrumented location may be much less than the pristine net section used to calculate the measured axial force. However, it appears as though member L0L1-B_d and L0L1-C_d, for the southbound loading scenarios, experience a lower measured force than modelled (Figure 5.8). This occurs when the control loading truck is in the lane opposite to the member in question. This could indicate that within the first panel, there is a discrepancy with the deck system stiffness between north and southbound load cases, which would reduce the proportion of the tensile load carried by the bottom chords, or that an alternate load path is present.

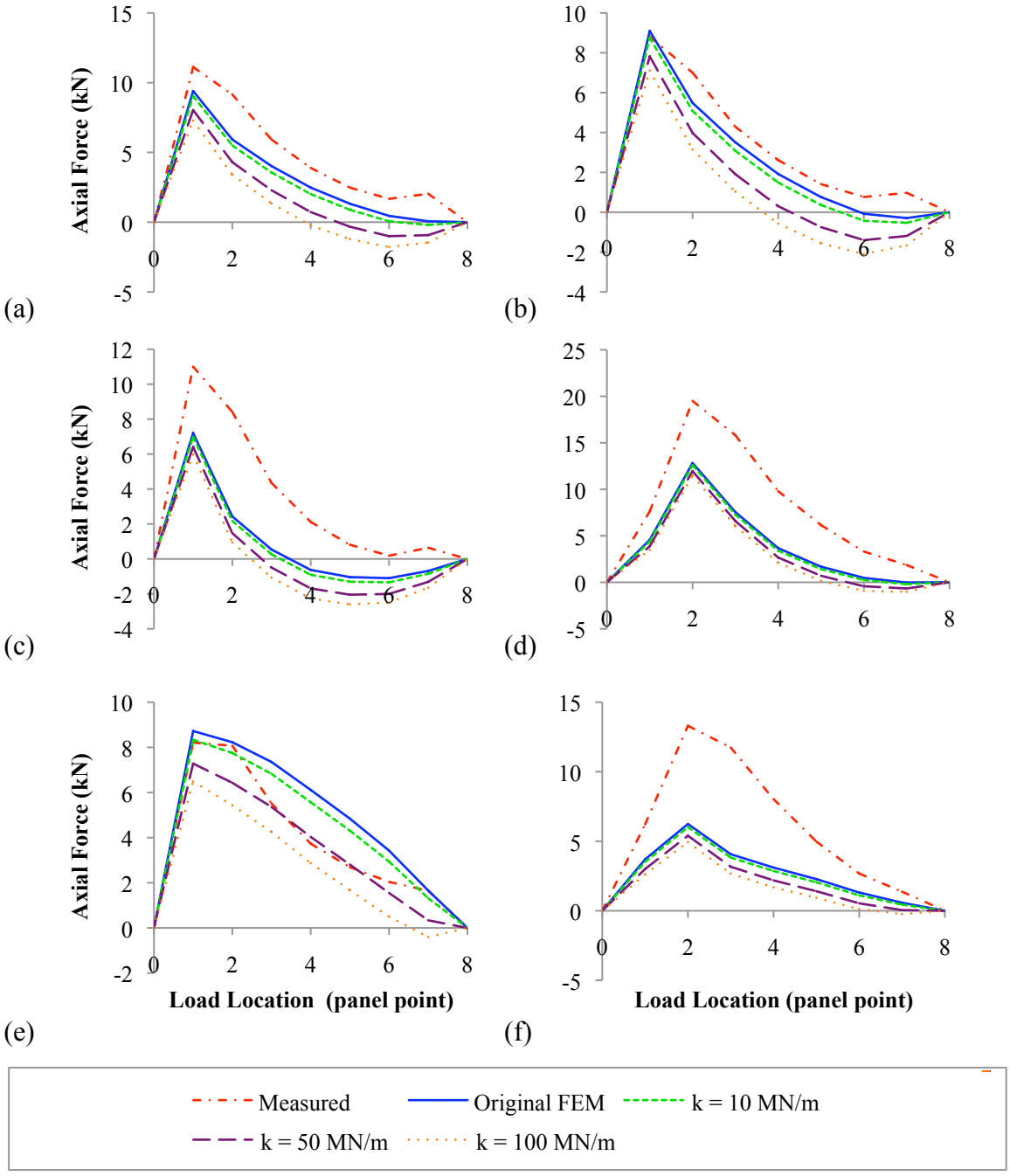

Figure 5.7. Bottom chord axial forces vs. load location for various support spring stiffness conditions for the northbound controlled loading scenario; (a) member L0L1-B_d; (b) member L0L1-C_d; (c) member L1L2-C_d; (d) member L2L3-C_d; (e) member L0L1-C_u; (f) member L2L3-C_u (refer to Figures 3.3 and 3.4 for member designations).

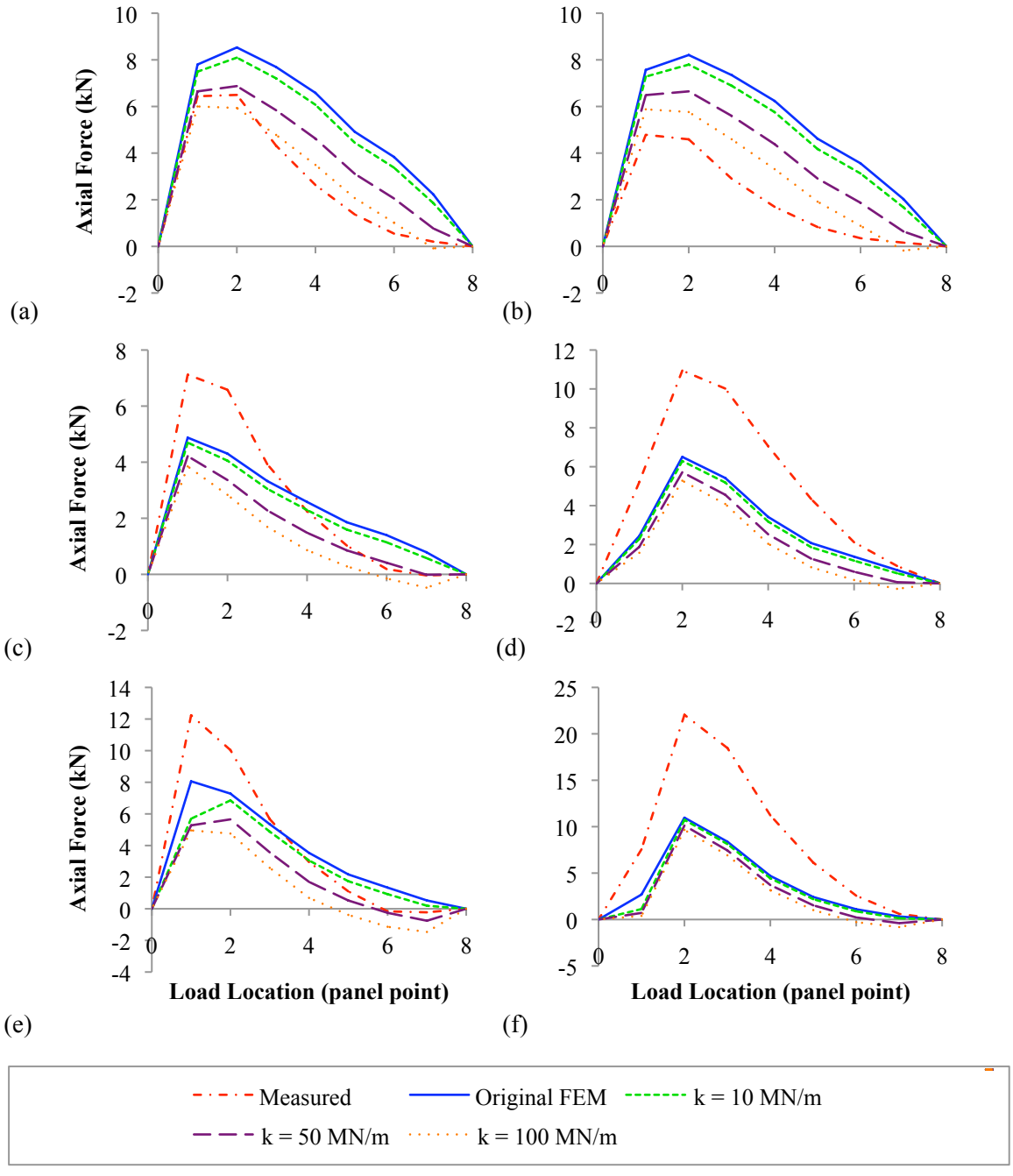

Figure 5.8. Bottom chord axial forces vs. load location for various support spring stiffness conditions for the southbound controlled loading scenario; (a) member L0L1-B_d; (b) member L0L1-C_d; (c) member L1L2-C_d; (d) member L2L3-C_d; (e) member L0L1-C_u; (f) member L2L3-C_u (refer to Figures 3.3 and 3.4 for member designations).

Increasing the stiffness of the springs did not improve the agreement between the measured and modelled forces. Table 5.6 lists the differences between the modelled and measured axial forces for the original model, and for the models with springs at the

supports. The increase in difference due to increased spring stiffness occurs because an increase in spring stiffness reduces the axial force in the bottom chord members. Since the measured axial force was greater than the modelled axial force with pin/roller supports (for most of the instrumented bottom chord members), this reduction caused a greater difference between the modelled and measured values. However, it is important to remember that the measured axial force is based on the pristine condition of the members, which overestimates the axial force based on the present condition of the bottom chord members. The exception to this trend occurred with members L0L1-B_d and L0L1-C_d for the southbound loading scenarios. This could be an indication that the bearing pads have seized on one side, or of the presence of a redundant load path.

Table 5.6. Difference between modelled and measured axial force in bottom chord members for the original FE model, and for FE models with springs located at the supports with stiffness values of 10 MN/m, 50 MN/m and 100 MN/m.

	Difference							
	Northbound				Southbound			
Member	original	10 MN/m	50 MN/m	100 MN/m	original	10 MN/m	50 MN/m	100 MN/m
L0L1-B_d	31%	37%	54%	68%	74%	63%	33%	14%
L0L1-C_d	20%	27%	48%	63%	126%	112%	71%	41%
L1L2-C_d	60%	64%	76%	84%	34%	36%	44%	53%
L2L3-C_d	48%	50%	55%	60%	46%	49%	56%	62%
L0L1-C_u	29%	21%	17%	32%	32%	43%	50%	59%
L2L3-C_u	57%	60%	66%	72%	54%	57%	61%	65%
Avg. Diff.	*41%*	*43%*	*53%*	*63%*	*61%*	*60%*	*53%*	*49%*

5.3.2.2 Modifications to Connectivity

There has been some debate as to how to model heavy class truss member connections. The ideal truss member carries only axial loads with no bending, when in fact any member with some flexural rigidity will experience bending to some extent. The amount of bending may be small, resulting from self-weight or eccentricity, or it could be the result of dynamic excitation or an unanticipated loading scenario. The gusset plate connections themselves limit the member rotation so that it is unlikely that each connection acts as a pure pin. However, the orientation of the bottom chord members, with the majority of the section located near the vertical centre of its cross-section, limits the amount of bending that can be transferred. To investigate this issue,

two FE models were constructed, one with pinned connections throughout, and the other with fixed top and bottom chord truss member connections and pinned connections elsewhere, as described in Chapter 4.

Figures 5.9 (northbound) and 5.10 (southbound) display the modelled and measured axial loads in the instrumented bottom chord members for the controlled loading scenarios. There is a very clear trend, with no exceptions, that the model with the fixed top and bottom chord connections produced much higher bottom chord axial loads. On average, the fixed connection model produced axial forces that were 114% higher than those of the pinned connection model. Comparing the measured axial forces to those predicted by the FE models, the pinned (original) model produced an average difference of 51%, while the fixed model produced a difference of 73%, relative to the measured results. The fixed model consistently predicted higher than measured axial forces.

The reason that the fixed model predicted such a significant increase in axial forces could be due to stiffening of the bottom chord load path with the fixed connections; the relatively stiffer bottom chords would therefore attenuate the tensile force shed to alternate load paths, such as through the deck. However, the fixed top and bottom chord model is not considered realistic because it is improbable for the bottom chord members to experience forces that are 73% higher than those measured, especially since the axial forces were calculated using the original, pristine cross-sectional areas and, therefore, were likely overestimated.

It can therefore be deduced that the bottom chord connections are behaving more like pinned connections than fixed, based on the overestimation of axial force by the fixed connection model. The measured axial force is more likely to agree with the pinned connection case when a more realistic (reduced) estimation of cross-sectional area is used.

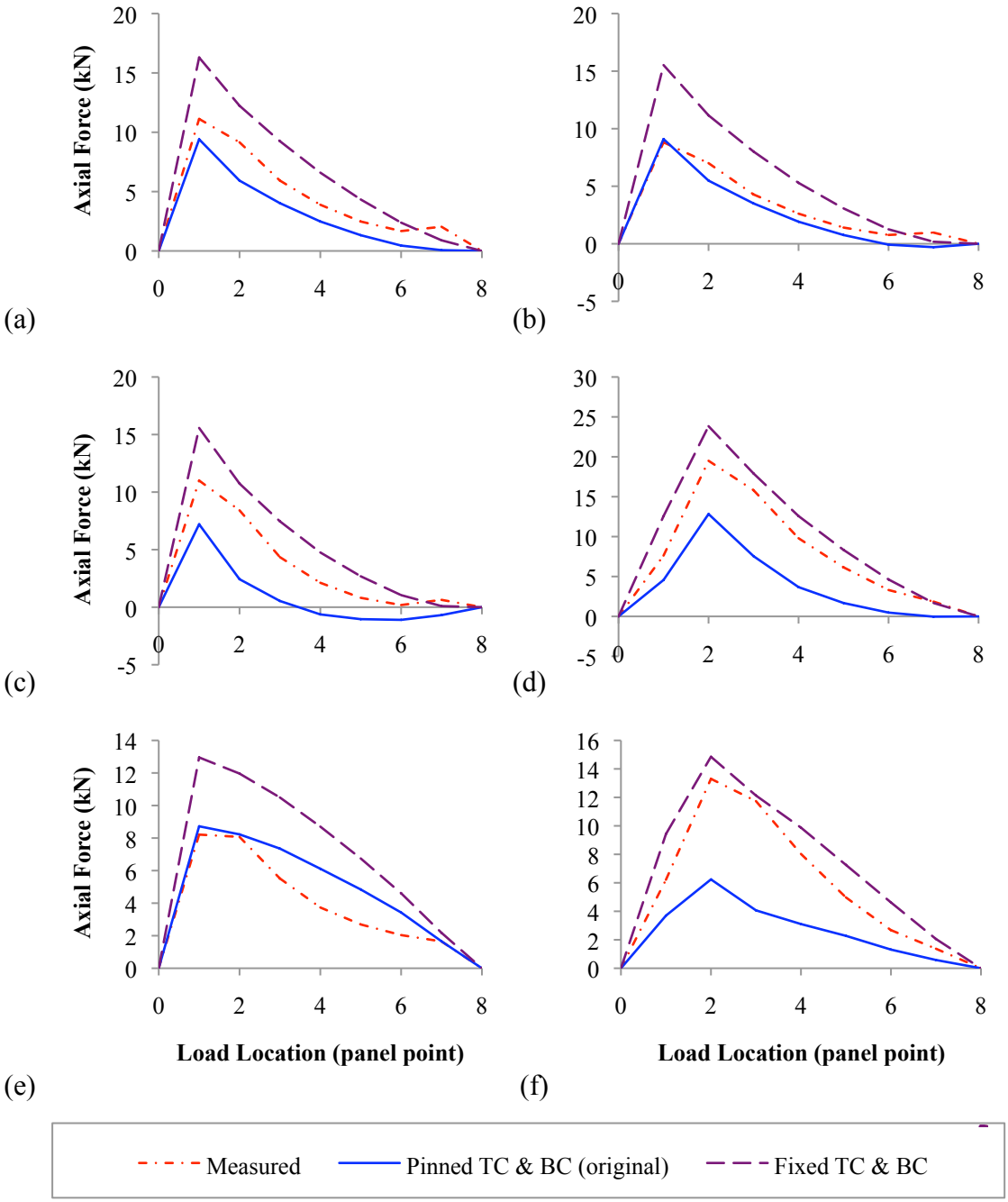

Figure 5.9. Bottom chord axial forces vs. load location for pinned and fixed top and bottom chord conditions for the northbound controlled loading scenario: ((a) member L0L1-B_d; (b) member L0L1-C_d; (c) member L1L2-C_d; (d) member L2L3-C_d; (e) member L0L1-C_u; (f) member L2L3-C_u.

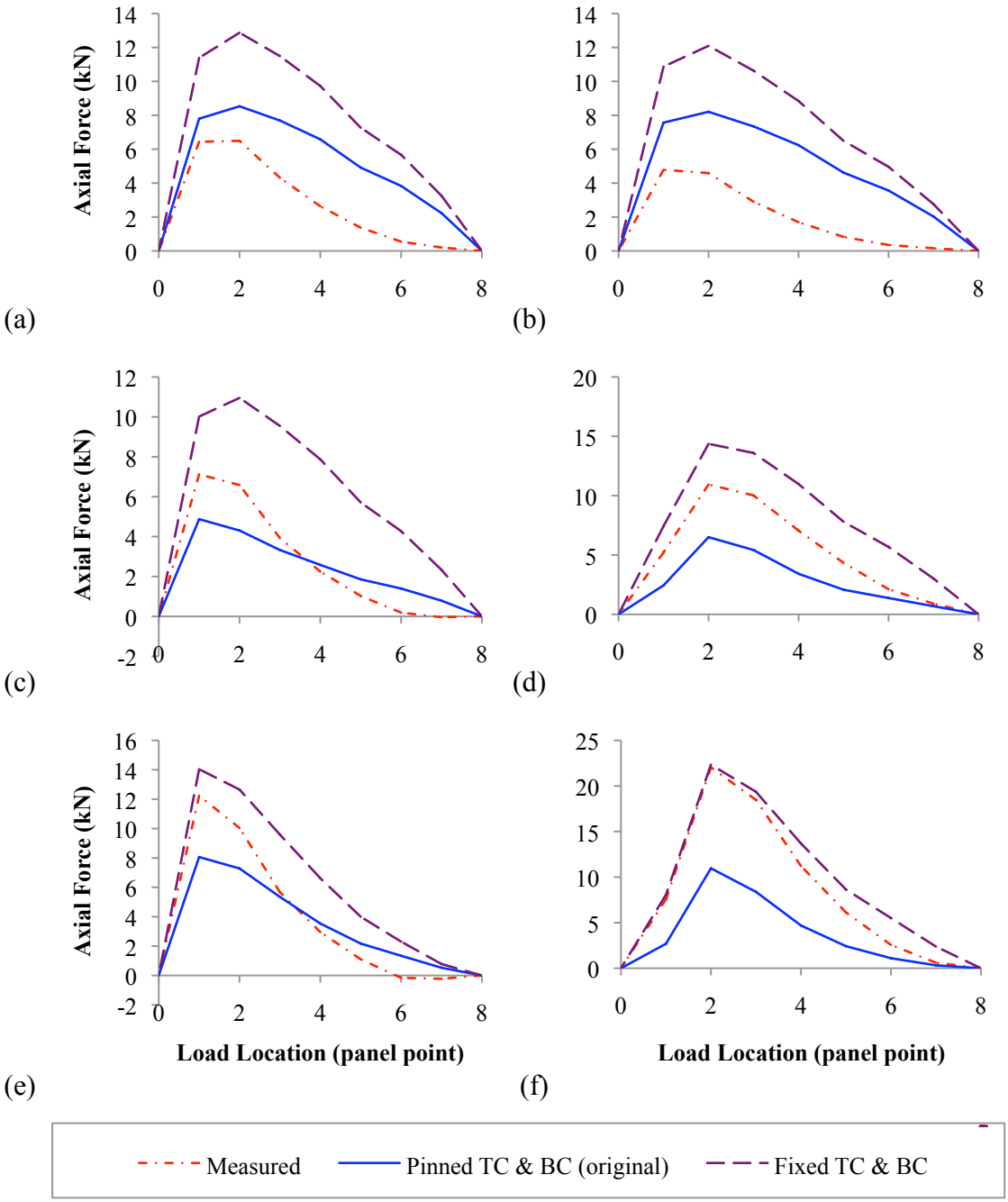

Figure 5.10. Bottom chord axial forces vs. load location for pinned and fixed top and bottom chord conditions for the southbound controlled loading scenario: (a) member L0L1-B_d; (b) member L0L1-C_d; (c) member L1L2-C_d; (d) member L2L3-C_d; (e) member L0L1-C_u; (f) member L2L3-C_u.

5.3.2.3 Modifications to Deck Member Elevation

To elevate the deck members to their true geometric elevations, a zero-mass vertical shear connector was created that was intended to transfer forces from one member to the next. The section properties of the vertical connector were defined by a factor multiplied by the floor beam stiffness (the largest member in the structure). The idea behind this factor was to permit alterations to stiffness, resulting in modifications to the amount of horizontal force transferred between members at different elevations. However, a decrease in stiffness of the vertical connectors merely resulted in a marginal increase in the bottom chord axial loads. On the other hand, increasing the stiffness using a factor greater than '1' accomplished a negligible change in the bottom chord axial load.

The bottom chord axial loads predicted by the raised deck and original models, as well as those measured, are illustrated in Figures 5.11 (northbound) and 5.12 (southbound). It is clear that the raised deck model overestimated the measured axial loads, with the exception of upstream bottom chord member L2L3-C_u for both of the southbound and northbound controlled static loading scenarios. The reason for the overestimation in bottom chord forces could be because the vertical connectors significantly reduced the stiffness of the deck system, thereby reducing the amount of axial load carried by the deck elements and effectively increasing the axial forces in the bottom chord members.

Although the raised deck model is more geometrically correct, the force transfer mechanism between elements at different elevations was not properly captured by the inclusion of the fictitious vertical shear connectors. The actual force transfer mechanism appears to be more effective, approaching a condition where all members are at the same elevation.

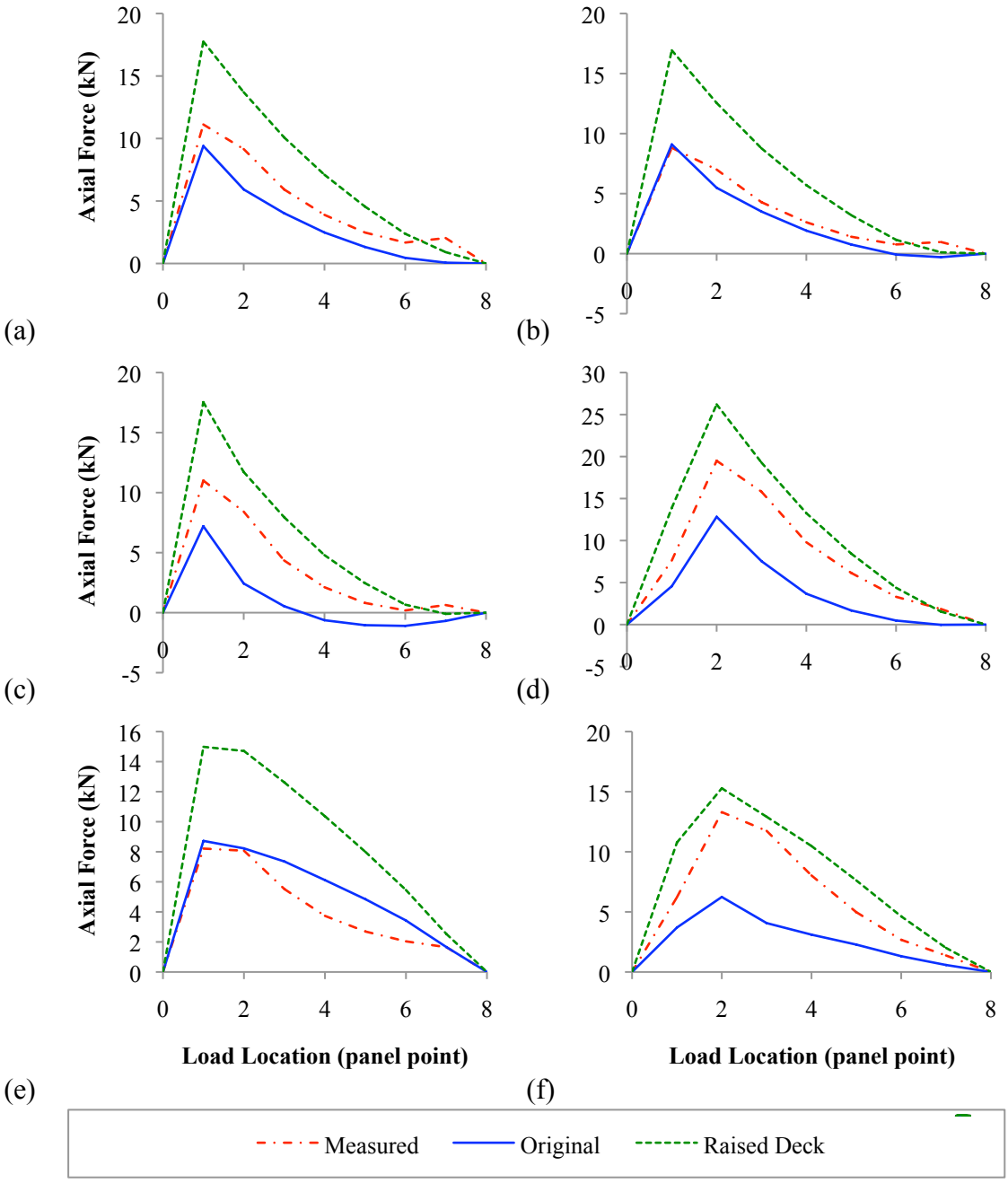

Figure 5.11. Bottom chord axial forces vs. load location for raised deck conditions for the northbound controlled loading scenario: (a) member L0L1-B_d; (b) member L0L1-C_d; (c) member L1L2-C_d; (d) member L2L3-C_d; (e) member L0L1-C_u; (f) member L2L3-C_u.

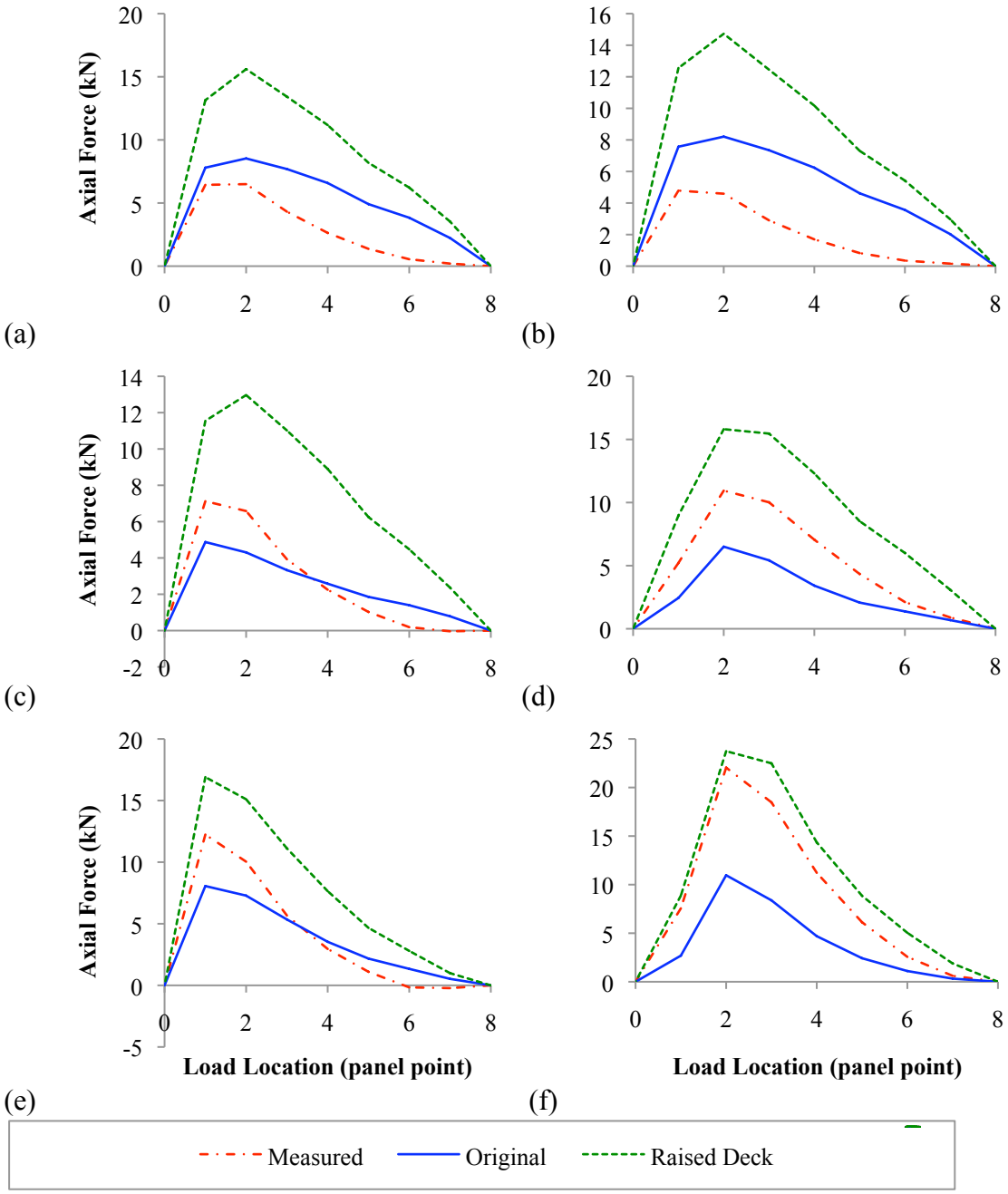

Figure 5.12. Bottom chord axial forces vs. load location for raised deck conditions for the southbound controlled loading scenario: (a) member L0L1-B_d; (b) member L0L1-C_d; (c) member L1L2-C_d; (d) member L2L3-C_d; (e) member L0L1-C_u; (f) member L2L3-C_u.

5.3.2.4 Modifications to Deck Stiffness

Since there is the possibility that the deck may assist in relieving some of the tensile forces endured by the bottom chord members, the level of its participation will depend on the deck stiffness. Figure 5.13 displays a plan view of the deck and walkway, showing a graphical representation of the distribution of normal stresses (Pa) in the longitudinal direction with the control load vehicle situated with the rear axle over panel point L3. It is evident that the deck carries the highest concentration of tensile stresses at the location of the vehicle and at the deck panels closest to the supports; also, the deck carries some tensile axial stress over the entire length and width of the loaded span.

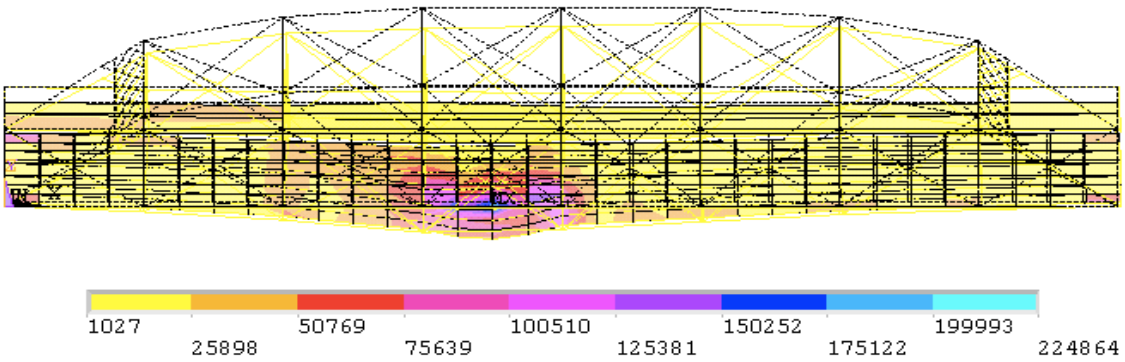

Figure 5.13. Tensile stress (N/m^2) for deck and walkway elements during the static loading scenario with the rear axle of the control load truck positioned on the downstream 3rd panel point (L3), as predicted by the original model with a deck modulus of elasticity of 10 GPa.

The deck modulus of elasticity was altered as described in Chapter 4. It can be seen in Figures 5.14 (northbound) and 5.15 (southbound) that as the deck stiffness increased, the transient axial load carried by all the bottom chord members decreased. Only results for the models with deck modulus of elasticity of 30 GPa (upper bound), 10 GPa (original model), and 3 GPa (lower bound) are shown in these figures; the relationship between bottom chord forces and deck stiffness was found to be fairly linear. This trend indicates that the modelled deck is contributing to structural redundancy. The redundancy occurred at and below the deck level only, for the upper truss members experienced a negligible change in axial member forces as various modelling parameters were varied.

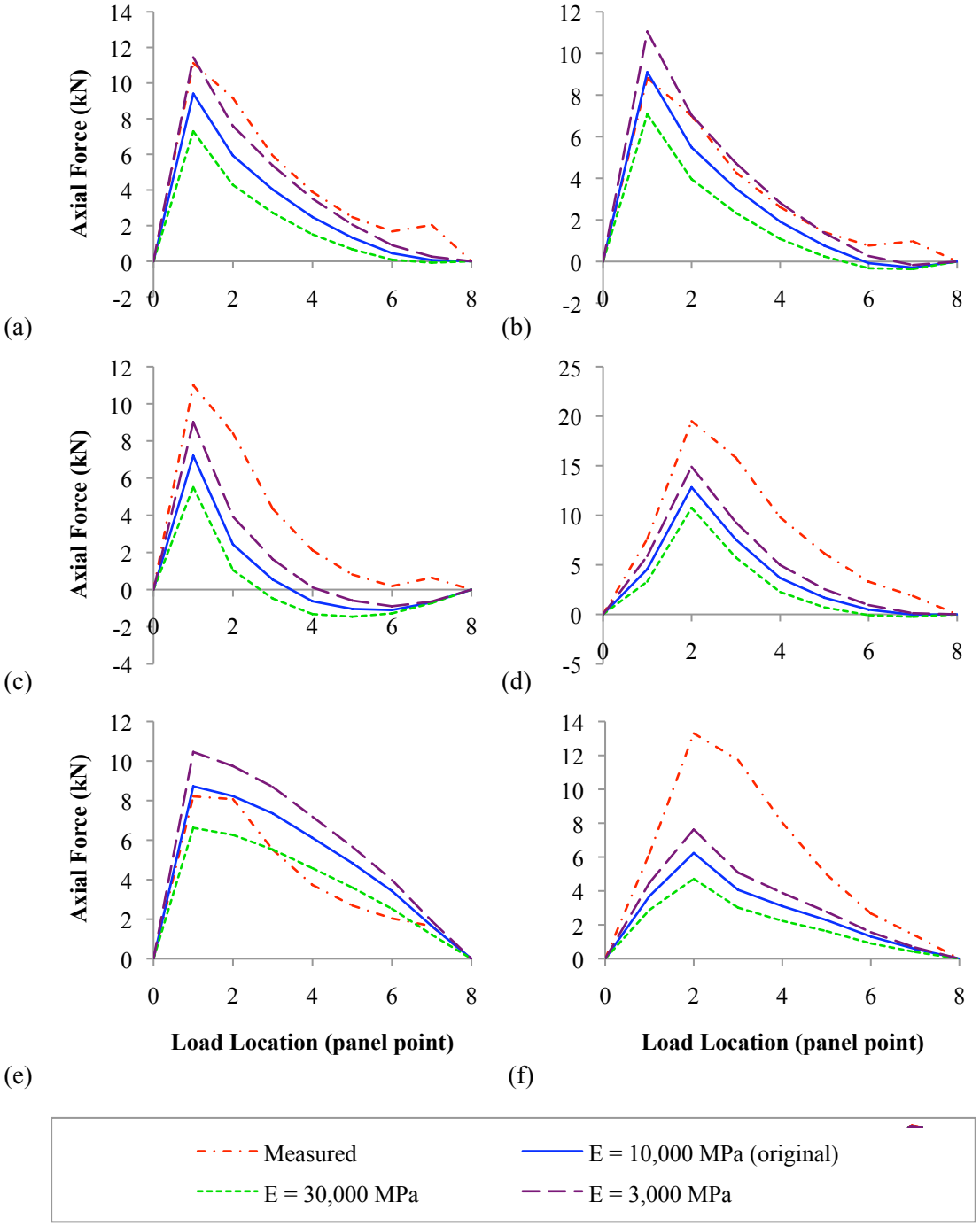

Figure 5.14. Bottom chord forces predicted by models with varying deck modulus of elasticity (E) and those measured vs. load location for the northbound controlled static loading scenario: (a) Member L0L1-B_d; (b) Member L0L1-C_d; (c) Member L1L2-C_d; (d) Member L2L3-C_d; (e) Member L0L1-C_u; (f) Member L2L3-C_u.

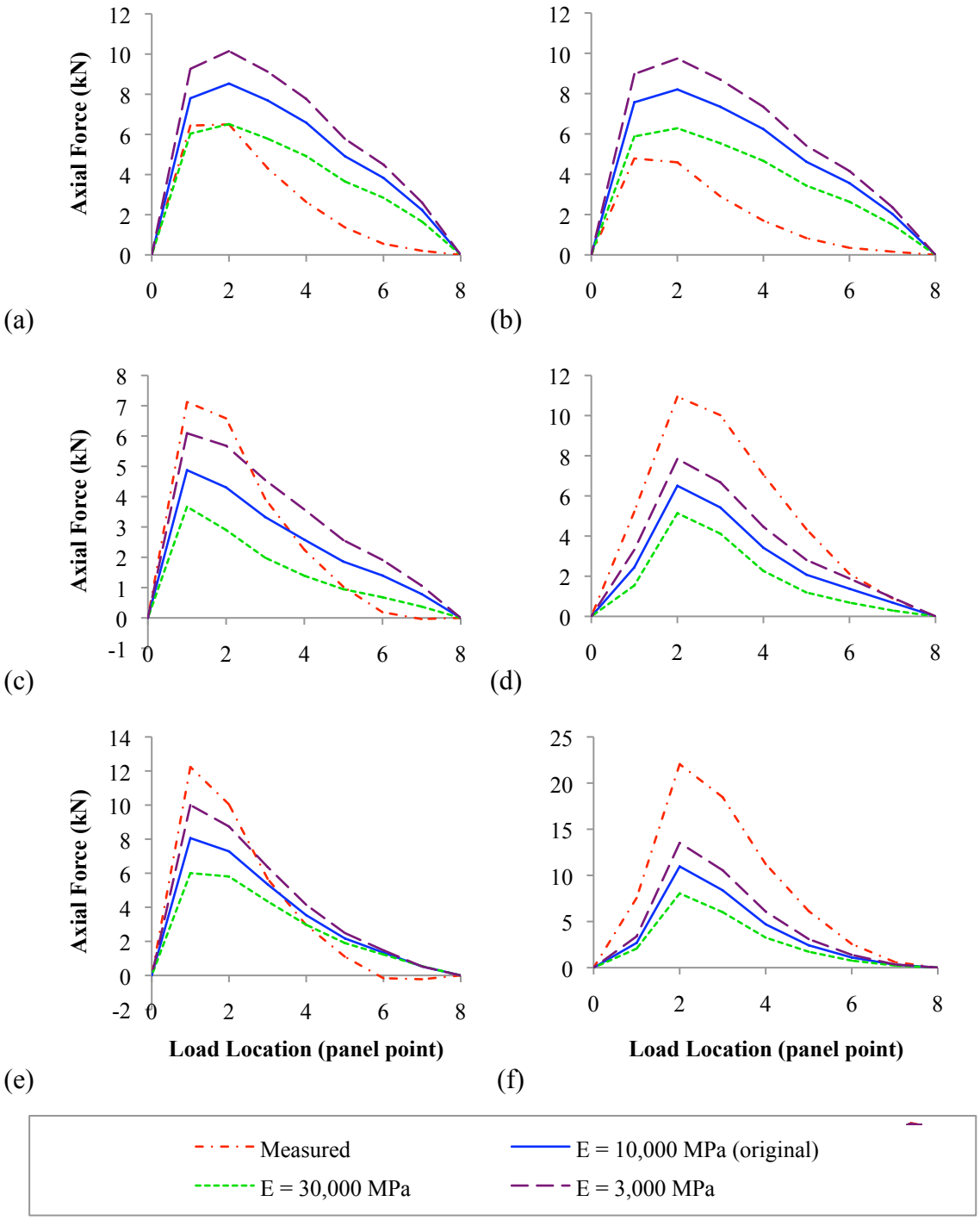

Figure 5.15. Bottom chord forces predicted by models with varying deck modulus of elasticity (*E*) and those measured vs. load location for the southbound controlled static loading scenario: (a) Member L0L1-B_d; (b) Member L0L1-C_d; (c) Member L1L2-C_d; (d) Member L2L3-C_d; (e) Member L0L1-C_u; (f) Member L2L3-C_u.

Table 5.7 lists the difference between the measured and modelled bottom chord axial forces. The trend common to most bottom chord members was that as the deck stiffness decreased, the difference decreased, providing a more accurate model. However, this trend did not occur for member L0L1-B_d and L0L1-C_d for the southbound controlled loading scenario, and for member L0L1-C_u for the northbound controlled loading scenario. This trend reversal occurred only within the end panel bottom chord members, and could indicate the presence of an alternate load path.

Table 5.7. Difference between measured and modelled bottom chord axial forces. The deck stiffness was modified from the original modulus of elasticity of 10 GPa, to 30 GPa and 3 GPa.

	Difference					
	Northbound			Southbound		
Member	E = 30 GPa	E = 10 GPa	E = 3 GPa	E = 30 GPa	E = 10 GPa	E = 3 GPa
L0L1-B_d	49%	31%	16%	43%	74%	100%
L0L1-C_d	38%	20%	21%	77%	126%	163%
L1L2-C_d	77%	60%	43%	51%	34%	30%
L2L3-C_d	60%	48%	37%	60%	46%	32%
L0L1-C_u	20%	29%	47%	46%	32%	22%
L2L3-C_u	68%	57%	48%	67%	54%	42%
Avg. Diff.	*52%*	*41%*	*35%*	*57%*	*61%*	*65%*

In summary, an increase in deck stiffness drew more axial load from the bottom chord members, resulting in an increased deck tensile stress. For the final model, the deck modulus of elasticity of 10 GPa was used because that was deemed to be a more realistic value, and because a change in the modulus from this value did not consistently increase the correlation to the measured results.

5.3.2.5 Modifications to Floor Beam Stiffness

Another possible factor affecting the redundancy associated with the deck structure could be the lateral stiffness of the floor beams. The stiffer the floor beams are in their lateral (weak axis) direction, the better the chance of tensile forces being transferred from the bottom chords through the floor beams, to other deck elements, such as the car joists, stringers, and deck (see Figure 4.4 for a diagram of the general arrangement of deck members). The nominal moment of inertia about the vertical axis was assumed to be the upper bound on the stiffness; however, since the floor beam is a deep member, approximately 750 mm in height, and attached to the truss near its bottom

flange, but to other deck members at the level of its top flange, the full cross-section may not be fully effective in resisting horizontal forces applied at the top flange. Therefore, a range of lateral moment of inertia values for the floor beams were considered to investigate their influence on truss bottom chord forces.

As the weak axis moment of inertia about the centroidal vertical axis was decreased in the FE model, the bottom chord axial forces increased, while the forces carried by floor joists and stringers decreased. This trend is shown in Figure 5.16, for the bottom chord member L2L3-C_d. The trend was similar for all bottom chord members. The lateral stiffness values plotted here represent the percentage of the nominal moment of inertia about the vertical axis. In general, it was found that, in the end panel, the stringers and joists closest to the bottom chord members sustained the greatest tensile forces in the FE model, reducing to negligible tensile forces sustained by the middle joists. The end panel stringers closest to the bottom chords (edge joist) produced a maximum-modelled axial tensile force approximately 50% greater than those in the adjacent car joist. The closest member to the bottom chord members carried a greater share of the tensile loads because the forces will find the stiffest path to the supports, as predicted by the FE model. However, based on visual observations, it was not anticipated that the edge joists would carry axial forces due to the deterioration of the edge joists. The instrumented floor joists were located closer to the centre of the deck, where the tensile forces predicted by the model were found to be negligible. This behaviour appeared to be consistent with the low measured levels of axial tension in these instrumented joists.

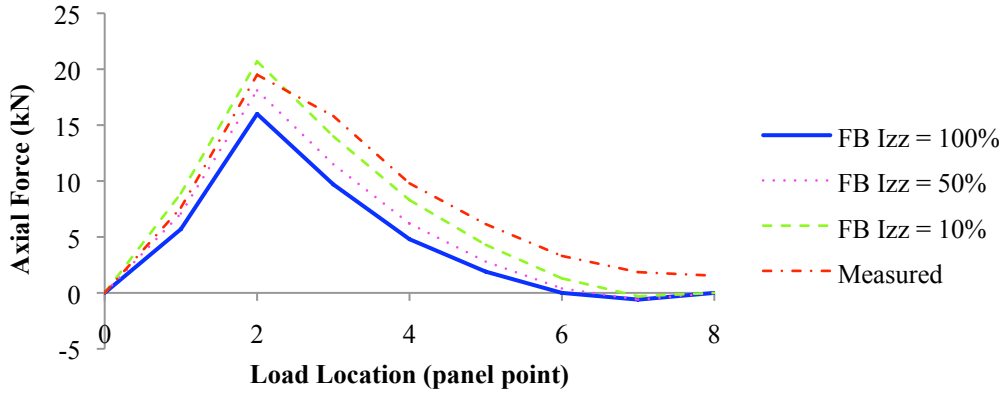

Figure 5.16. Bottom chord member L2L3-C_d axial load vs. load location for varying lateral stiffness (Izz) in the floor beam (FB) members.

There was not one specific moment of inertia about the vertical axis of the floor beam that provided a significantly greater correlation to the measured results, although stiffness values ranging between 10%-50% of the full, calculated value seemed to produce adequate agreement (see Figure 5.16). A moment of inertia about the vertical axis of 50% of the actual value was therefore used for the final model since it produced lower magnitude tensile forces in the car joists and stringers, while not entirely eliminating the alternate load paths for tensile forces. Also, the value was reasonable from a practical point of view, since the floor beam was relatively tall and slender and connected to the deck elements at the level of the top flange, suggesting that something in the order of half of its entire stiffness could be effectively engaged to transfer the loads laterally. With a reduction in the modelled moment of inertia about the weak axis of 50% the nominal value, the modelled bottom chord forces increased, on average, to 115% of the value calculated using the original model.

5.3.2.6 Modifications to Bottom Chord Member Properties

To test the effects of possible redundant load paths at the bottom chord and deck level, the bottom chord members were damaged one member at a time. The modulus of elasticity, shear modulus, and density were reduced by a common factor for the full length of the member to simulate damage. As described in Chapter 4, the material properties were reduced by 10%, 20%, 30%, 40%, 50%, 60% and 75% of the original

properties. In a purely determinate system, these changes would not affect the distribution of truss forces. However, the existence of alternate load paths would result in changing member forces with changes in member stiffness.

It was found that a reduction in material properties of one bottom chord member did not substantially affect the axial load carried in the other bottom chord members. The most significant change in axial load was in the altered member, with a reduction in axial force that was approximately proportional to the reduction in member properties. This is demonstrated in Figure 5.17, which illustrates the modelled axial force in various bottom chord members for the case with damage to member L1L2-C_d (for member designations, see Section 3.2.1 and the corresponding Figures 3.4 and 3.5). Figure 5.17 (c) displays that the altered member is affected most significantly. The bottom chord members just to the south of the altered member, L0L1-B_d (Figure 5.17 (a)) and L0L1-C_d (Figure 5.17 (b)) and just to the north of the altered member, L2L3-C_d (Figure 5.17 (d)), also experienced a reduction in axial forces, but to a lesser extent. A change in stiffness of 10% resulted in a change in axial forces of the adjacent members (L0L1-B_d, L0L1-C_d) of approximately 1-2%. The upstream bottom chord members (L2L3-C_d and L2L3-C_u) experienced a slight (0-1%) increase in axial forces with the reduction in stiffness of a downstream bottom chord member. Since all bottom chord members experienced some level of change in force with damage, the model demonstrated a degree of redundancy of the 3D truss at the bottom chord level. This modelled response was typical of all cases involving damaged bottom chord members.

Since the bottom chord members are composed of four angles bolted together, an FE model was constructed to replicate the behaviour should one of the four angles experience a reduction in member properties. As the modulus of elasticity was reduced for one of the four parallel members, it was found that each of the undamaged components of that member sustained the same axial load as it had carried prior to the modification of the material properties in the damaged components. However, the member with the reduced modulus of elasticity experienced a reduction in axial force that was approximately proportional to the reduction in the modulus of elasticity. If the model is an accurate representation of the structural system of the Traffic Bridge, this indicates that the load is not strictly being shared at a local member scale, since the

undamaged parallel components' axial forces did not increase when the damaged component axial force decreased. Instead, the portion of the force shed from the damaged component appeared to be picked up by other members, such as the deck. Since the strain measurements in parallel components appear to be insensitive to damage experienced by one of the components, the detection and localization of damage using strain gauges attached to every component may not be possible. Had the parallel components relieved the damaged component of the axial load, the detection of damage in this way would have been feasible.

There is some uncertainty as to the accuracy of the model, for, in the field, the parallel members are bolted together at regular intervals between the truss nodes while parallel members in the FE model were not connected, except at the joints. However, should the parallel components act as a fully composite member, there would not be differential strain readings between the various components, unless the member was subject to bending, which the strain-time history described in Section 5.2.3 illustrated was not the case.

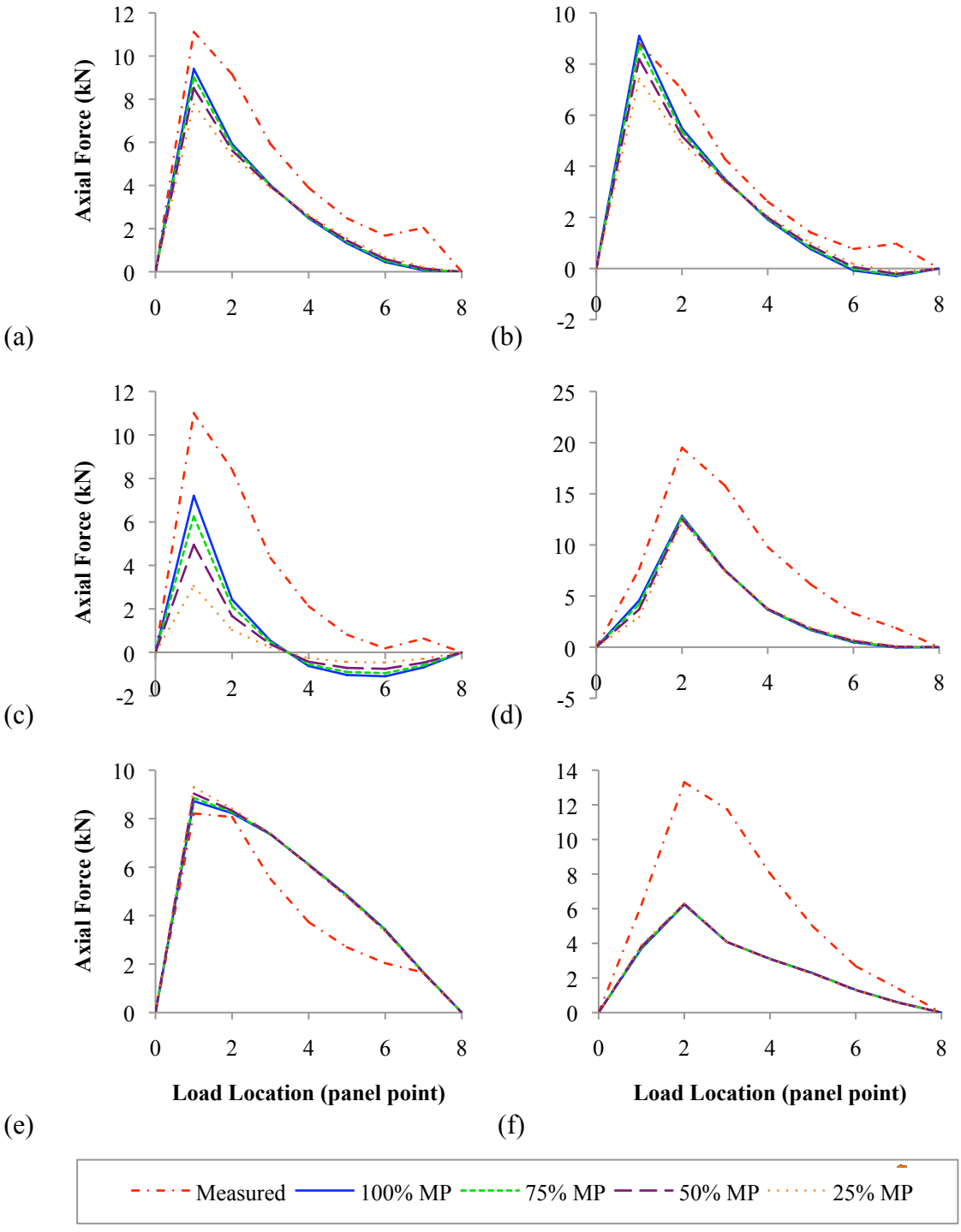

Figure 5.17. Modelled bottom chord axial load vs. load location for various levels of damage to member L1L2-C_d damage: (a) Member L0L1-B_d; (b) Member L0L1-C_d; (c) Member L1L2-C_d; (d) Member L2L3-C_d; (e) Member L0L1-C_u; (f) Member L2L3-C_u (see Figures 3.3 and 3.4 for member locations).

All upper truss members, including the end post, top chord members, verticals and diagonals, experienced no change in axial forces with changes in the material properties of any truss member. This indicates that there is negligible structural redundancy at this level. Therefore, should a member experience a reduced stiffness, it still must carry the same loads.

5.3.3 Model Parameter Modification Summary

It was found that all modelling parameter modifications resulted in negligible changes in the modelled axial forces sustained by the upper truss members (end post, top chord, vertical and diagonal members). Only the bottom chord members and deck elements experienced a change in forces as a result of altering the modelling parameters (discussed in previous sections).

Based on the observations made from all of the model iterations, a final FE model was selected that consisted of the following alterations to the original FE model:

- a 20% reduction in the modulus of elasticity for all bottom chord members due to the softening from deterioration (160,000 MPa); and
- a floor beam lateral stiffness reduction of 50%, which was accomplished by reducing the moment of inertia about the vertical (weak) axis.

The following modelling parameters for the final FE model remained the same as for the original FE model:

- pinned truss joint connections throughout;
- pinned/roller support conditions;
- deck members that were modelled at the same geometric centroid elevation as the bottom chord members; and
- a deck modulus of elasticity of 10,000 MPa.

It was found that this final model provided the most consistent correlation with trends observed in the measured strain data. Table 5.8 displays the difference between the pristine measured and the modelled axial forces for the static load cases, with the rear axle at panel points one through seven.

The major remaining differences between the final FE model and the measured results occur with peak axial forces in the bottom chord members in the first two panels. For a given member, the final model may match the northbound measured results well,

while differing from the southbound results, or vice versa. The modelled axial force in the bottom chord members matched the measured axial force most closely in the second (L1L2) and third (L2L3) panels.

Although the steel truss bridge in question is a relatively simple structure, the attempts to reduce bottom chord member properties so that calculated axial forces matched the measured results proved to be largely unsuccessful. Every alteration that was investigated provided inconsistent results, with some members having a higher correlation to the measured axial force while others had a lower correlation.

Table 5.8. Average difference between the pristine measured and the modelled bottom chord axial forces for the static controlled load scenarios, with panel points one through seven loaded.

Model:	Final		Fixed TC & BC		Spring Support		Raised Deck	
Member	Northb.	Southb.	Northb.	Southb.	Northb.	Southb.	Northb.	Southb.
L0L1-B_d	25%	79%	47%	146%	54%	63%	60%	183%
L0L1-C_d	33%	130%	75%	130%	47%	268%	92%	268%
L1L2-C_d	40%	24%	47%	24%	75%	134%	60%	134%
L2L3-C_d	25%	15%	27%	15%	55%	64%	37%	64%
L0L1-C_u	43%	28%	76%	28%	17%	65%	108%	65%
L2L3-C_u	41%	40%	24%	40%	66%	21%	31%	21%
Avg. Diff.	*34%*	*53%*	*49%*	*64%*	*52%*	*102%*	*65%*	*122%*

Due to the variability in the comparison results, estimating the net remaining cross-sectional area for the individual bottom chord members based on the modelled results also proved to be difficult. By comparing the final FE model axial forces to the forces inferred from measured strains for the controlled loading scenarios, an attempt was made to estimate a modification factor (MF) that could be applied to measured results to account for member damage and other uncertainties. An MF factor for a particular bottom chord member was calculated by dividing the peak modelled force in that member by the peak-measured force, based on pristine section properties. For example, for member L0L1-B_d, the maximum force was sustained when the truck was located at panel point L1. The MF for this member was therefore calculated as the ratio of modelled to measured forces when the load was applied at this panel point. Separate MF factors were calculated for northbound and southbound loading scenarios. The peak forces were used for this calculation to reduce the error associated with low amplitude responses.

The MF's for the northbound and southbound loading directions, as well as the average of the two for each bottom chord member, are listed in Table 5.9. Also listed are the rms differences between the modelled and modified measured forces, considering the response when the truck was at the seven interior panel points, calculated using Equation 5.5. The COV listed corresponds to the variation of the simple difference between the modelled and modified measured forces, again considering the response when the load was applied at the seven interior panel points.

Table 5.9. Bottom chord member axial force modification factors (MF) with corresponding rms difference between modelled and modified measured forces, and coefficient of variation (COV) of the difference.

	Northbound			Southbound			Average		
Member	MF_N	Diff.	COV	MF_E	Diff.	COV	MF_A	Diff.	COV
L0L1-B_d	1.1	32%	65%	1.45	35%	68%	1.28	41%	47%
L0L1-C_d	1.3	30%	42%	1.9	35%	64%	1.60	42%	35%
L1L2-C_d	1	40%	43%	1.05	21%	72%	1.03	35%	235%
L2L3-C_d	0.92	22%	56%	0.9	6%	75%	0.91	19%	123%
L0L1-C_u	1.25	20%	73%	0.9	31%	48%	1.08	30%	85%
L2L3-C_u	0.62	15%	110%	0.6	4%	51%	0.61	9%	148%
Average	*1.03*	*27%*	*65%*	*1.13*	*22%*	*63%*	*1.08*	*29%*	*112%*

The MF values should conceptually be less than one to account for the loss of section from deterioration. However, four of the six instrumented bottom chord members were found to require MF values greater than one. This usually occurred when the truck was located in the opposite lane, relative to the bottom chord with the elevated MF. This result could not be adequately explained, and occurred predominantly for the bottom chord members between panel points L0 (the support) and L1 for both the upstream and downstream trusses. This could be attributed to a stiffness value for the modelled deck members that was too high in the first panel, effectively increasing the modelled axial force carried by the deck assembly, and decreasing the axial force received by the bottom chord members in the end panel. Further modelling alterations to force MF values to remain below unity were not attempted, because the iteration possibilities were infinite. It was deemed that the final FE model possessed realistic properties, and could be suitable, paired with the MF values, given the level of uncertainty involved.

Figures 5.18 and 5.19 compare the axial forces in the bottom chord members for the final model, raised deck model, spring support (bearing stiffening) model, fixed top and bottom chord model, measured based on pristine section properties and the MF_A-modified measured values. The FE models incorporating the raised deck and fixed top and bottom chord connections produced significantly higher axial forces than those inferred from measured results, which can be explained as follows.

1. The fixed connections between truss members provide a significantly stiffer load transferring system than the deck system. Since loads tend to follow the stiffest path to the supports, the loads were resisted almost entirely by the truss system in this model.
2. The raised deck geometrically does not allow for load sharing between the truss members and the deck system. Again, since the truss system was stiffer than the deck system, the loads were primarily resisted by the truss system.

In reality, the remaining net section of the bottom chord members is less than 100% due to the deterioration. It can be concluded that the "pristine" measured axial forces represent an upper bound, since the full geometric cross sectional areas, with no deterioration, were used to calculate these forces. This suggests that the FE models incorporating the raised deck and fixed top and bottom chord connections provided less accurate representations of the measured data.

The final model, and sometimes the model with the springs at the bearings, however, appeared to be more viable options to model the axial load path of the members. Overall, the final FE model produced the highest correlation, based on the lowest error values relative to the MF-modified measured response. Even with this model, however, significant differences in force distributions remained relative to measured values.

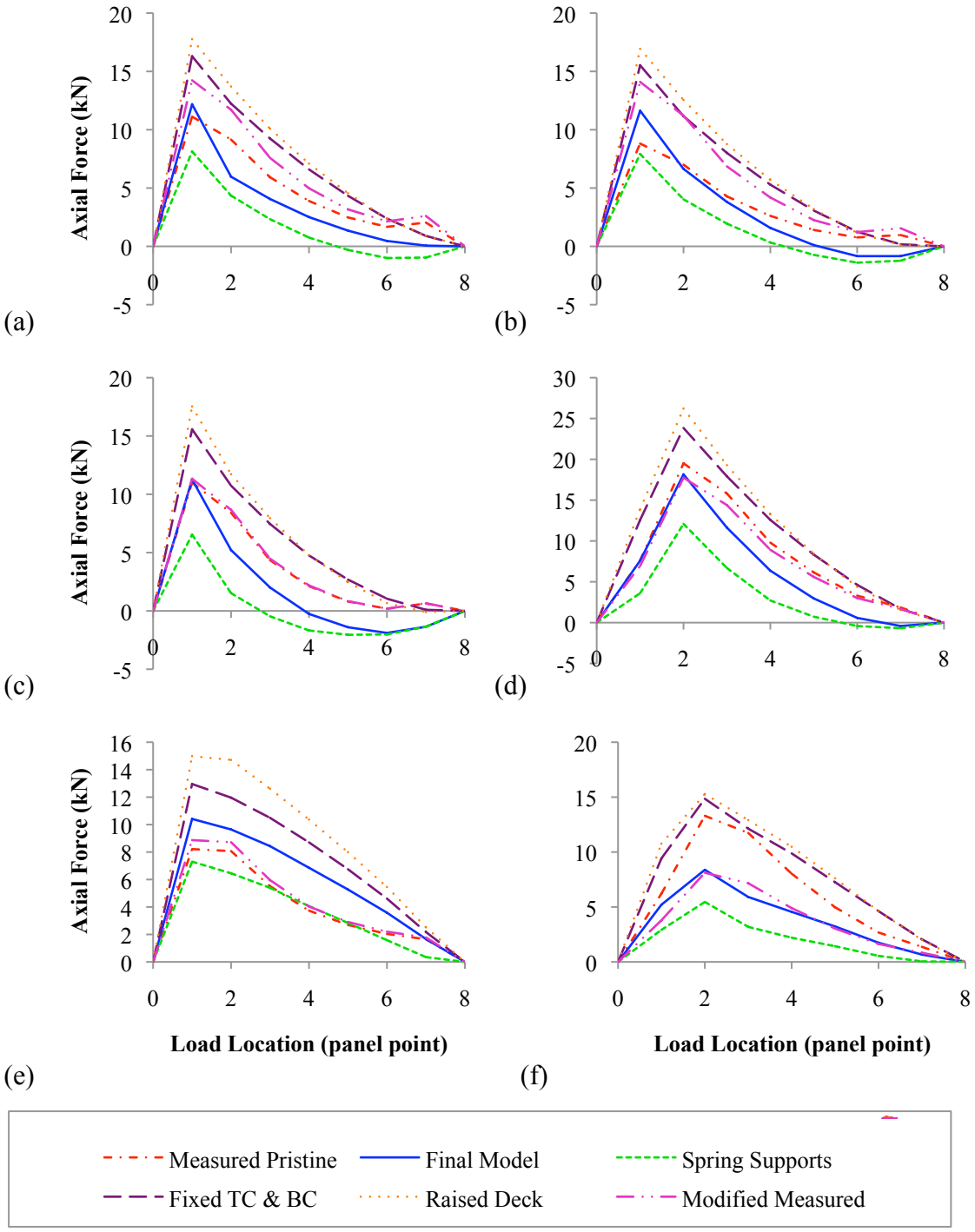

Figure 5.18. Northbound modelled vs. measured bottom chord axial loads: (a) Member L0L1-B_d; (b) Member L0L1-C_d; (c) Member L1L2-C_d; (d) Member L2L3-C_d; (e) Member L0L1-C_u; (f) Member L2L3-C_u.

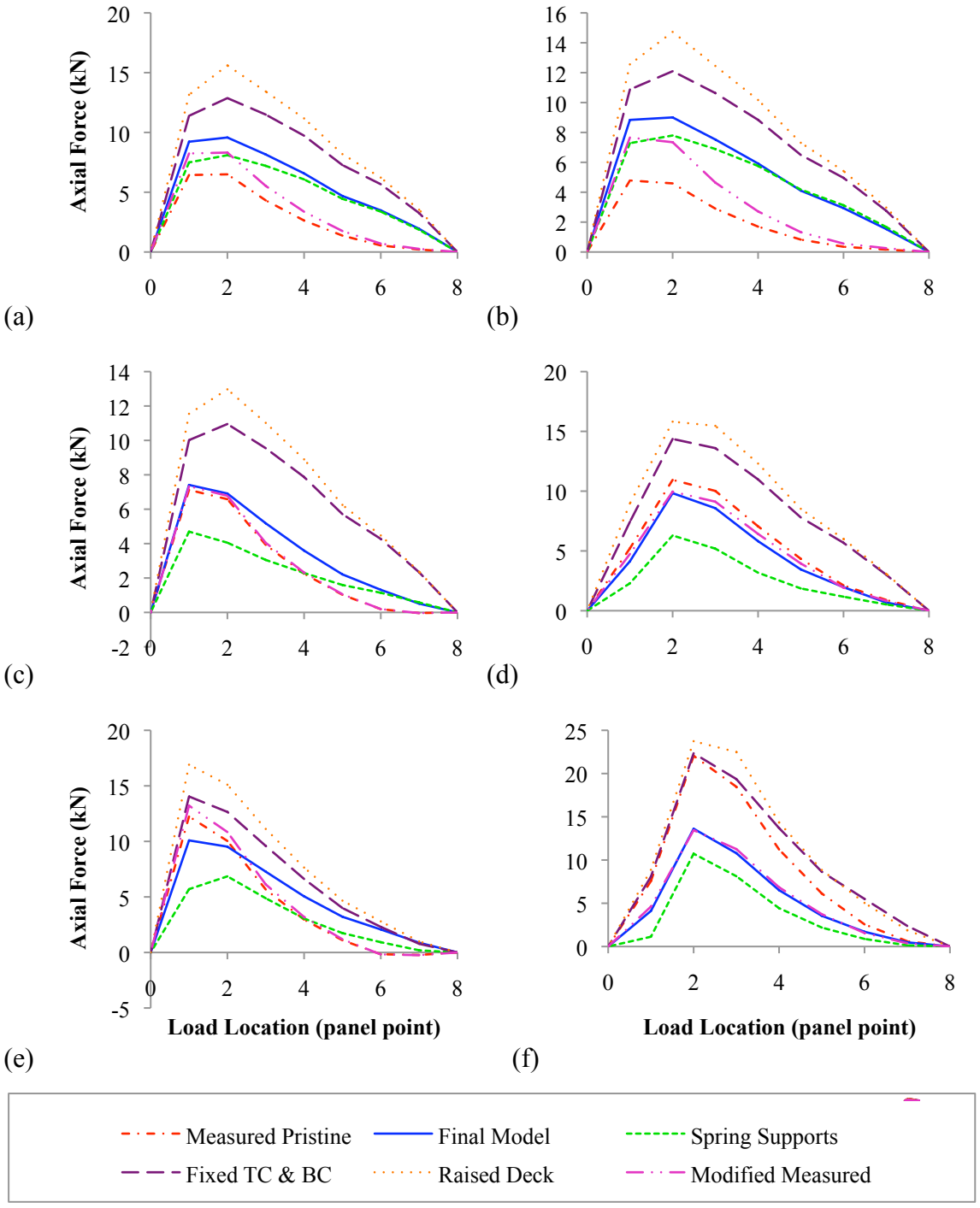

Figure 5.19. Southbound modelled vs. measured bottom chord axial loads: (a) Member L0L1-B_d; (b) Member L0L1-C_d; (c) Member L1L2-C_d; (d) Member L2L3-C_d; (e) Member L0L1-C_u; (f) Member L2L3-C_u.

Based on the final FE model, the distribution of tensile forces among the bottom chord members, deck, and joists are listed in Table 5.10 along with the corresponding coefficient of variation, calculated considering the distribution when loaded at the seven interior panel points. The force distribution, *FD*, was calculated at each panel point by taking the average ratio of axial forces carried by a particular member group, T_{MGp}, to the total axial force carried by all member groups combined, T_{Tp}, when the control load vehicle was located at each of the panel points:

$$FD = \frac{1}{n}\sum_{p=1}^{n}\left(\frac{T_{MG}}{T_T}\right)_p \qquad \{5.6\}$$

where *n* is the panel point number at which the load was located. For example, while the control load vehicle was located at the second panel point, the axial force distribution was calculated at the second panel point cross-section. This was done for each of the seven panel points and averaged.

From the distributions listed in the table, it appears that the tensile loads were relatively evenly distributed among the bottom chord members, the edge and regular joists and the deck. The bottom chords sustain approximately one-third of the tensile loads, while the deck, edge and regular joists sustain the rest. The car joists experience low levels of compressive force relative to the tensile forces in the other deck member (2% of the total). If the final FE model is accurate, this is a significant finding, because this would verify that the bottom chords only sustain approximately one-third of the anticipated axial tensile loads. However, further experimental verification that the edge and regular joists are contributing is necessary before making such a conclusion. Also, the final model simulates the lack of tensile forces in the car joists, which was verified by measurements (see Section 5.2.2.4).

Table 5.10. Tensile axial load distribution between bottom chord members and deck elements.

Member Group	Northbound Tensile Force Distribution, FD_N	COV	Southbound Tensile Force Distribution, FD_S	COV
Bottom Chord	31%	63%	35%	48%
Edge & Regular Joists	18%	67%	17%	64%
Car Joists	-2%	69%	-2%	65%
Deck	53%	60%	50%	60%

5.3.4 Post-Tensioning (PT) Effects

It was of interest to determine the effectiveness of the PT system used to reduce the tensile loads in the deteriorated bottom chord members. First, in this section, the estimated response of the bottom chord with and without PT was calculated using the FE model; it should be noted again that the strain gauges were installed after the PT system was in place, so these effects could not be observed directly.

For the study of the PT effects, the FEM was first manipulated by modifying the stiffness of the floor beams to represent the statically determinate response as closely as possible. The statically determinate response refers to the expected response of a two-dimensional, statically determinate truss. The purpose of building a model that represented two-dimensional, statically determinate behaviour was to demonstrate the redundancy that occurs at the deck level with a three-dimensional truss (to be verified in the following sections). To obtain the statically determinate forces in the bottom chord members, the floor beam stiffness in its lateral direction was reduced to 3% of its nominal value, and the deck stiffness was reduced to a value just above zero (100 Pa).

For this section, the focus is on the effects of the post-tensioning system. To understand these effects, a comparison was made between the statically determinate bottom chord forces (with and without the PT system in place), and those calculated using the *final model* that was used to compare with the measured strains. The modifications to the nominal member properties of the truss members for the *final model* are explained in the following sections.

Figure 5.20 displays the bottom chord axial loads in the upstream and downstream trusses calculated using the statically determinate model due to: (1) self-weight of the bridge prior to the PT installation (denoted as gravity loads only); (2) the effects of the PT installation without gravity loads; and (3) the resulting combination of the self-weight of the structure and the PT effects (denoted as gravity + PT). Notice that the axial forces in the bottom chord members resulting from the self-weight of the bridge are not identical for the upstream and downstream trusses due to presence of the walkway on the upstream side. This analysis was completed with the original FE model (described in Chapter 4) with the stiffness of the deck and floor beams reduced as described above.

Based on this analysis, although not identical, both the upstream and downstream bottom chord members appear to experience similar axial forces. The PT forces applied at the two trusses differed due to the added mass of the walkway for the upstream truss; 274 kN was applied for each downstream PT bar, and 297 kN for each upstream PT bar (see Chapter 4). The statically determinate axial forces in the bottom chord members due to self-weight only were all tensile, as expected. The highest axial forces occurred at the centre of the truss, and the lowest forces in the end bottom chord members, again as expected.

The statically determinate force distributions observed from the PT effects are as follows:

1. There is little to no force present due to the PT system in the bottom chord members from the support to the PT bulkhead (end panel);
2. The bottom chord PT force between bulkheads is relatively uniform; and
3. The modelled bottom chord members near supports experience non-zero, tensile forces from the PT system; therefore, since there is no net force in the cross section at this location, the deck must be experiencing compressive forces in the end panel to balance these forces. Although the forces in the bottom chord end panel before the bulkhead are relatively small, this is an indication of load sharing between the bottom chord members and the deck, despite the fact that the stiffness of deck elements was very small for this analysis.

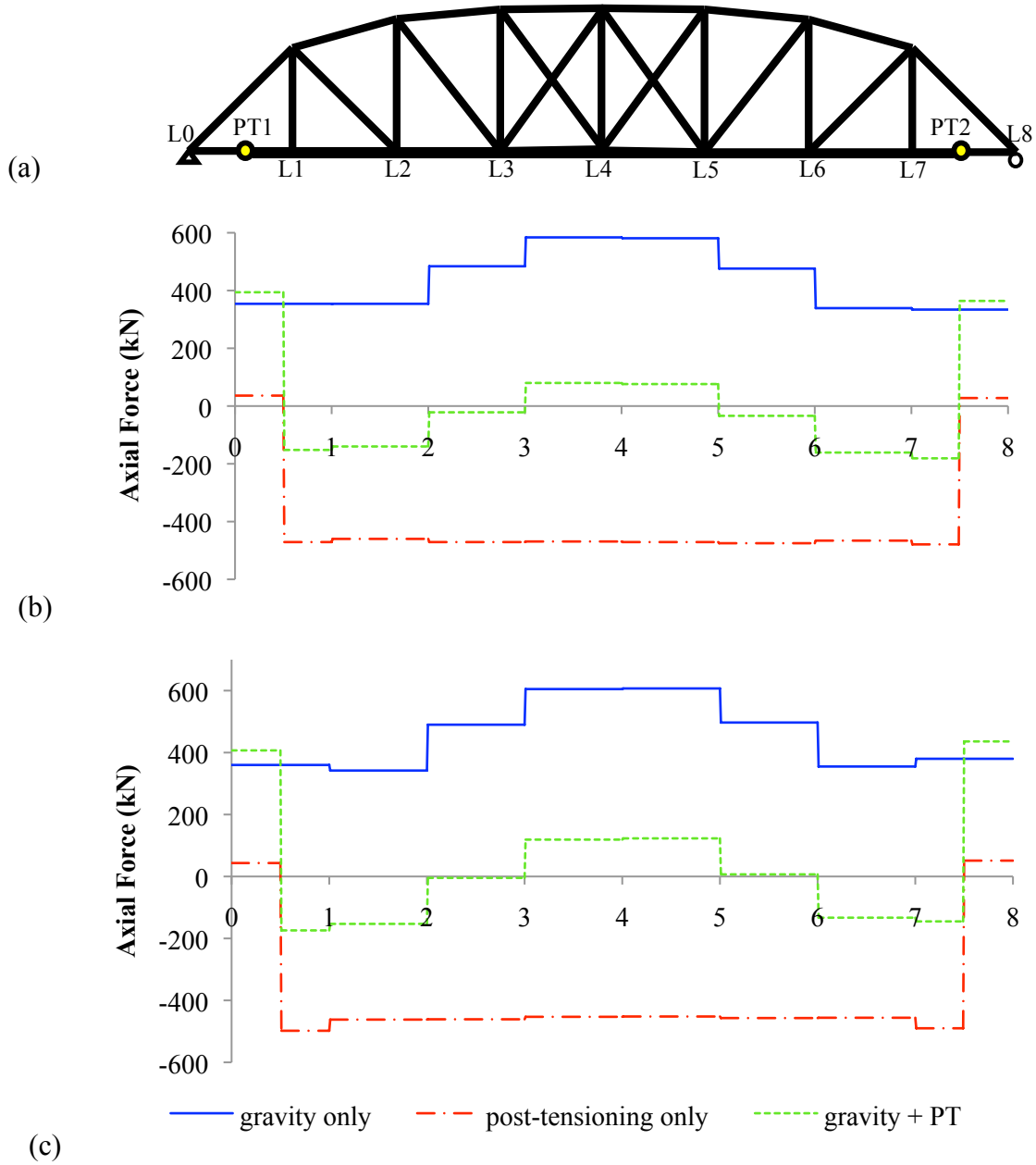

Figure 5.20. Statically determinate/modelled bottom chord force distribution due to gravity alone, post-tensioning (PT) alone, and gravity and PT combined: (a) bridge elevation; (b) downstream bottom chord; (c) upstream bottom chord.

The reductions in floor beam and deck properties used for the statically determinate analysis just described are unrealistic because the deck elements had an assumed zero-stiffness. The force distribution from self-weight and the PT system calculated using the final FE model (described in Chapter 4) is illustrated in Figure 5.21.

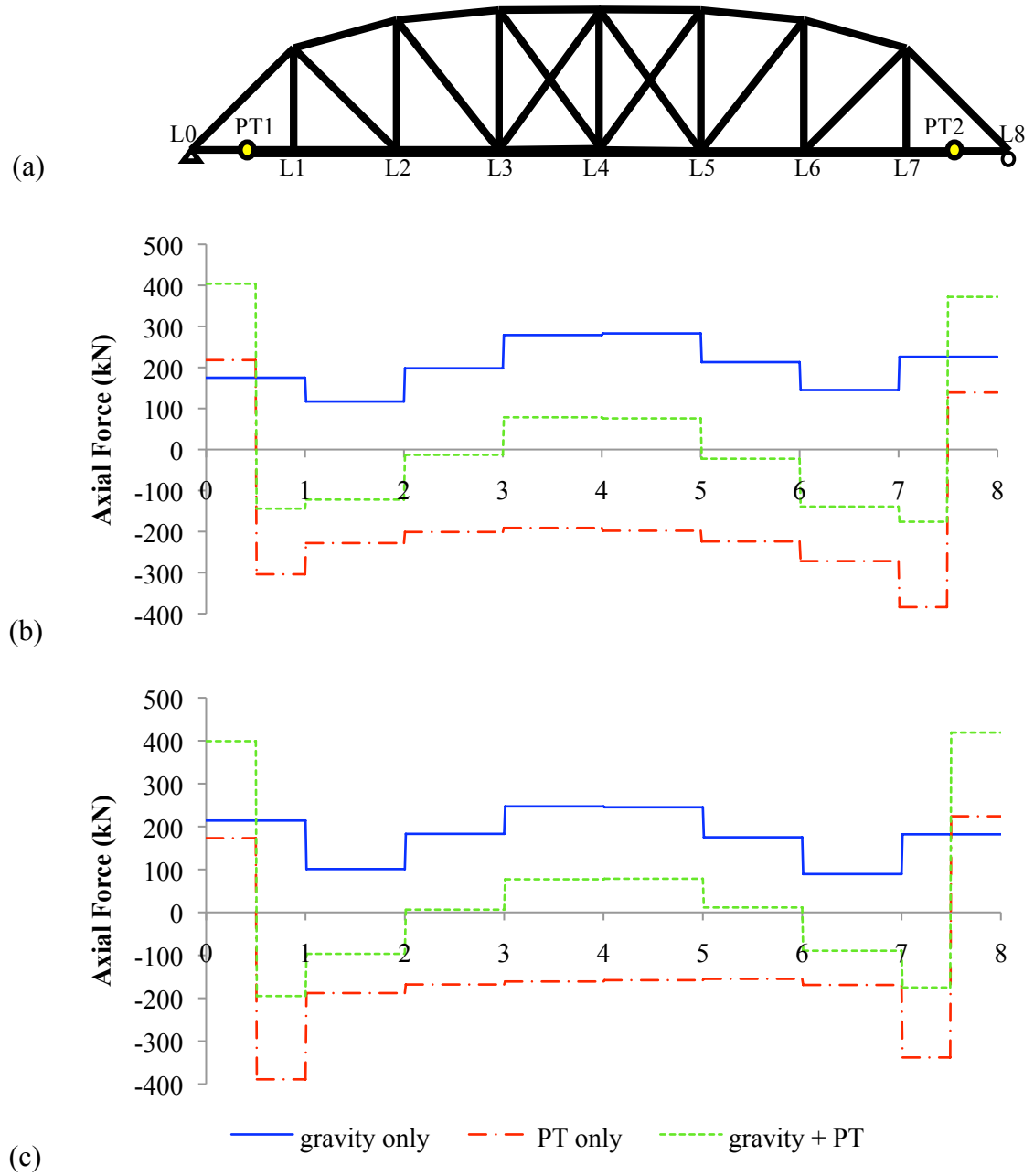

Figure 5.21. Final model axial forces resulting from self-weight, post-tensioning, and combined self-weight and post-tensioning: (a) bridge elevation; (b) downstream bottom chord; (c) upstream bottom chord.

Focusing on the statically determinate axial loads induced by the PT system only in Figure 5.20, it is apparent that the PT system is effective in inducing compressive forces in the bottom chord between the PT bulkheads. Between bottom chord members *L2* and *L7*, the PT induced compressive force remains consistent between 425 and 480 kN. However, it is interesting to note is that even with pin/roller supports, a deck

modulus of elasticity of 100 Pa, and a floor beam lateral moment of inertia of 3% its actual value, there is enough stiffness for the PT system to force the bottom chord into tension (between 37 and 66 kN) between the support and the PT bulkhead. This means that the bottom chord between the supports and the PT bulkheads endures a slightly higher tensile load due to the presence of the PT system. Also, under self-weight and the PT effects, the bottom chords are forced into as much as 181 kN of compression. The centre-two bottom chord members between panel points L3 and L5 remain in tension, with approximately an 80 to 87 percent reduction in axial forces relative to the gravity-only condition.

The *final* model, used to compare with the statically determinate model, used a deck modulus of elasticity of 10,000 MPa (10^8 times larger than the statically determinate model value), and a floor beam lateral moment of inertia of 50% the nominal value (17 times larger than the statically determinate model value). The choice of deck stiffness is explained in Section 5.3.2.4, and the choice of reduction in the floor beam lateral moment of inertia is explained in Section 5.3.2.5. As seen in Fig. 5.20, the *final* model produced an unexpected axial force distribution in the bottom chord due to self-weight without PT effects. Due to self-weight acting alone, the bottom chord members endure much lower axial forces in the middle panels than in the statically determinate model, suggesting that deck members are carrying a significant portion of the tension forces. On the other hand, the axial force in the end panel (L0L1) bottom chord members spikes to almost double the adjacent bottom chord member (L1L2). This spike in the end panel axial force suggests that tension forces being carried by the deck in the mid-span region are being transferred back into the bottom chord end panel member in order to reach the support locations.

In the *final* model, the PT system acting alone induces very large tensile forces in the bottom chord between the support and the bulkhead, with magnitudes ranging from 139 kN to 224 kN. This forces the bottom chord between the support and the bulkhead to sustain approximately double the original axial loads due to self-weight. The results from the gravity and PT effects combined indicate that only the bottom chords in the central panels remain in tension, with the axial loads reduced by approximately 70 percent compared to the self-weight only system. The other bottom chord members are

forced into compression, with magnitudes up to 95 kN. This verifies that the PT system is working to reduce the axial forces in the bottom chord members, but perhaps almost working "too well" by forcing some of the bottom chord members into compression.

The FE analysis demonstrates how the post-tensioning system reduces the axial forces in the bottom chords between the attachment locations. While it is not within the scope of this project to analyze the capacity of the bridge, it is worth noting that the post-tensioning system does appear to enable some bottom chord members to experience a lower tensile load from gravity effects than would otherwise be the case. However, the PT effects may also result in some net compressive forces in some bottom chord members that were originally designed to primarily withstand tension forces.

As another method used to establish how well the FEM represented the actual reduction in axial forces due to the PT system, the measured reduction factors in Table 5.11 were calculated for each constant speed load trial, *j*, by dividing the axial force experienced by the bottom chord member between the PT bulkhead and the first panel point (F_{B_L1}), by the axial force experienced by the bottom chord member between the support and the PT bulkhead (F_{L0_B}) at each panel point, *n*, as:

$$PT_{reduction} = \left(\frac{1}{n} \cdot \sum_{i=1}^{n} \frac{F_{B-L1}}{F_{L0-B}} \right)_i \qquad \{5.7\}$$

For each controlled loading scenario speed, the response was captured three times and averaged to compare with the modelled values. The measured force PT reduction factors ($PT_{reduction}$) indicate a reduction in axial forces of approximately 24% to 29%. Although the measured reduction factors have a high coefficient of variation for the static loading scenarios, the reduction factors are relatively uniform for all loading scenarios. Based on these PT reduction factors, it is evident that the PT system effectively reduces the forces caused by transient loading by 24% to 29%. It is not possible to determine from this measurement how effectively the PT system reduces the axial forces due to self-weight; however, it is clear that the PT system reduces the transient load effects by approximately one quarter.

Table 5.11. Average measured axial force reduction factor due to PT system and coefficient of variation (COV) corresponding to the variation among the three trials at each speed as well as the variation among the values obtained when the truck was at each panel point.

Trial	Northbound	COV	Southbound	COV	Average
Static	0.80	213%	0.73	107%	0.76
20 km/hr	0.73	5%	0.68	18%	0.71
30 km/hr	0.72	6%	0.71	10%	0.72
50 km/hr	0.72	6%	0.70	41%	0.71

The modelled reduction factors in Table 5.12, on the other hand, indicate a reduction ranging from 3% to 9% only. In the southbound load case, the original model experienced an *increase* in the axial force between the bulkhead and first panel point compared to the force experienced between the support and the PT bulkhead, with a factor of 1.42. The *final model* force reduction factors match the measured values slightly better, with reductions of 12% to 13%, but still only indicate a reduction in forces of about half of the measured force reductions.

Table 5.12. Modelled axial force reduction factor due to PT system and COV.

Model	Northbound	COV	Southbound	COV	Average
Original	0.94	51%	1.42	30%	1.18
Raised Deck	0.91	16%	0.93	2%	0.92
Spring Bearings	0.97	56%	0.96	1%	0.97
Fixed TC & BC	0.94	5%	0.92	1%	0.93
Final Model	0.87	55%	0.88	3%	0.88

The discrepancies between the measured PT reduction factors and the modelled PT reduction factors could be due to a slightly smaller remaining cross sectional area between the bulkhead and first panel point, resulting in an overestimation of the measured force and therefore a greater difference in forces before and after the PT bulkhead. The original model poorly replicates the PT reduction factor experienced from the measured forces, while the final model resembles the PT reduction factors the most closely among the different models, and still is off by approximately 16% of the measured values.

5.3.5 Upper Truss Member Correlation to the Measured Strain-Time History

The top chords, vertical members and diagonal member that were instrumented had axial forces that matched the modelled axial forces relatively well. All model types provided almost identical axial loads for the given loading scenarios. Unlike the bottom chord member results, there was not a significant discrepancy in axial force between the northbound and southbound loading scenarios. Table 5.13 provides the average MF and correlation of the final modelled axial forces to the measured axial forces for the loading scenarios.

After modifying the cross-sectional areas used to calculate the axial forces, the measured strains provided an accurate estimation of axial forces, using the modelled values as a basis for comparison. The original measured forces were typically smaller than corresponding modelled results, so the measured forces had to be increased by the MF factors listed in Table 5.13 to match the modelled axial forces. The modification factors brought the average difference between the final model and the measured force to 10%. The lower measured forces could be due to the strain gauges not picking up the full strain due to deformation of the adhesive between the gauge and the relatively stiff - weldable backing.

Figure 5.22 displays the modelled, measured, and modified measured axial forces as a function of load panel point location. It is apparent that the modified measured forces match the modelled forces consistently well, with the exception of three members: the measured force peaks do not reach the modelled values for members L0U1-Ab_d, L2U2-D_d, and U1L2-E_d. A very good correlation between the forces is found for the rest of the members.

It is unlikely that the measurements from the strain gauges for the upper truss members can be used for damage detection in the future. Since the modelled force values were not sensitive to changes elsewhere in the truss, any change measured in the axial force of these upper members could only be produced by damage at the location of the instrumentation. The apparently determinate behaviour of the upper truss members meant that deterioration at one location did not result in a noticeable change in the distribution of truss member forces.

Table 5.13. Upper truss member measured force modification factor (MF), and the corresponding difference between the final model and the modified measured values, and COV.

	Northbound			Southbound			Averaged		
Member	MF_N	diff.	COV	MF_S	diff.	COV	MF_A	diff.	COV
L0U1-A_d	1.2	11%	171%	1.15	5%	64%	1.18	11%	215%
L0U1-A_u	1.2	11%	126%	1.15	4%	79%	1.18	11%	194%
U2U3-A_d	1.1	7%	50%	0.90	4%	67%	1.00	12%	91%
U2U3-A_u	0.5	9%	49%	1.05	3%	95%	0.78	37%	46%
L1U1-D_d	1.36	18%	134%	1.36	11%	137%	1.36	17%	163%
L2U2-D_u	1.2	20%	134%	1.25	13%	79%	1.23	18%	131%
L0U1-E_u	1.2	14%	108%	1.25	16%	129%	1.23	14%	61%
Average	*1.11*	*13%*	*110%*	*1.10*	*8%*	*93%*	*1.10*	*10%*	*102%*

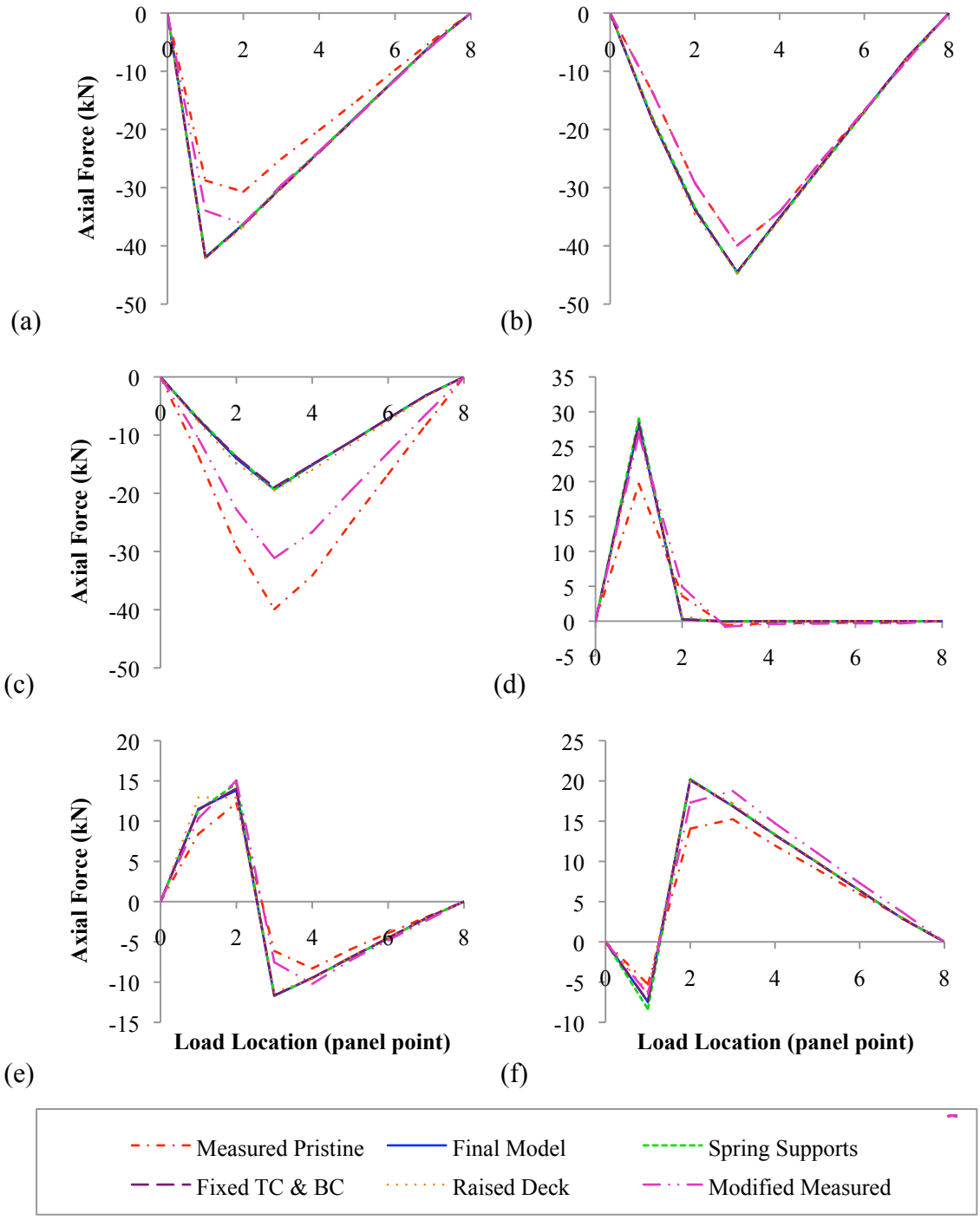

Figure 5.22: Northbound modelled axial load vs. measured axial forces for upper truss members: (a) Member L0U1-Ab_d; (b) Member U2U3-A_d; (c) Member U2U3-A_u; (d) Member L1U1-D_d; (e) Member L2U2-D_d; (f) Member U1L2-E_d.

5.4 DYNAMIC RESULTS

One form of model verification can be achieved by comparing the dynamic response of the model to the measured results. As described in detail in Chapter 3, eight accelerometers were used to capture the acceleration response at the lower truss panel points. Of the eight accelerometers, two were maintained at the same locations to act as reference points for constructing the mode shapes while the other six accelerometers were moved between the upstream truss and the downstream truss. The dynamic measurements were not used for vibration-based damage detection (VBDD), but only to confirm that the model was able to simulate the actual dynamic response of the bridge. The dynamic measurements were taken from random loading events using 29 trials (see Section 3.3.1).

A graphical representation of the two measured mode shapes is illustrated in Figure 5.23. The upstream truss is shown along the longitudinal axis while the downstream truss is shown starting at a lateral value of 6.4 m (21 ft). The first mode shape, with a frequency of 2.71 Hz, displays both trusses displacing almost symmetrically, indicating a predominantly flexural behaviour. The second mode shape, with a frequency of 5.34 Hz, displays a torsional movement, with the trusses moving in opposite vertical directions.

The final ANSYS model provided a good correlation to the measured results. The first mode shape, with a modelled frequency of 2.72 Hz, produced a modal assurance criterion (MAC) value of 0.9945 compared to the corresponding measured mode shape (for a description of the MAC, see Section 3.5.2). The second mode shape, with a frequency of 5.38 Hz, had a MAC value of 0.9922. A perfect match between the measured and modelled mode shapes would have given a MAC value of unity. These values indicate a good correlation. The modelled vs. measured mode shapes are plotted in Figure 5.24. The dynamic results appear to indicate that the FE model provides a reasonable approximation of the bridge's dynamic behaviour.

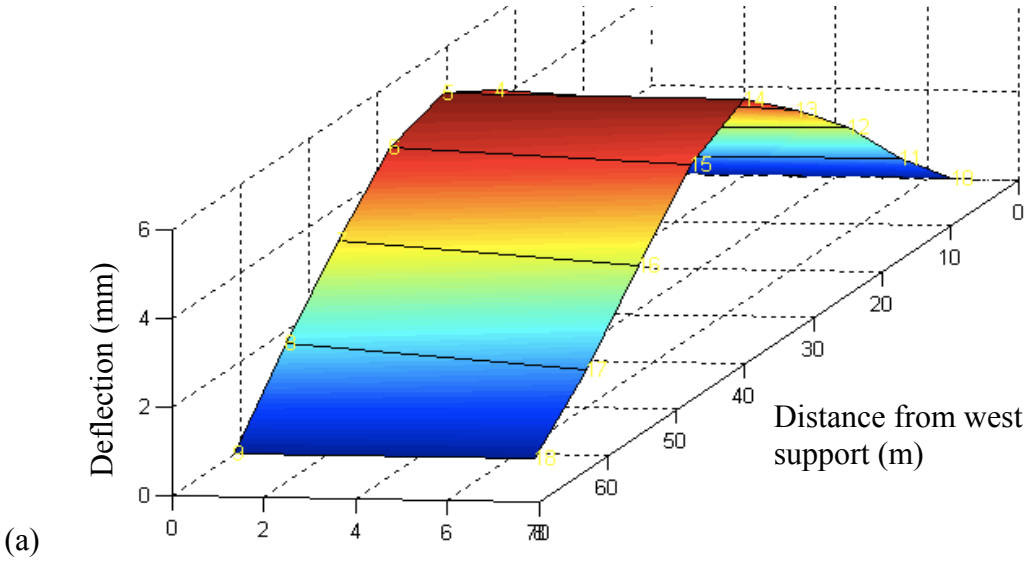

(a)

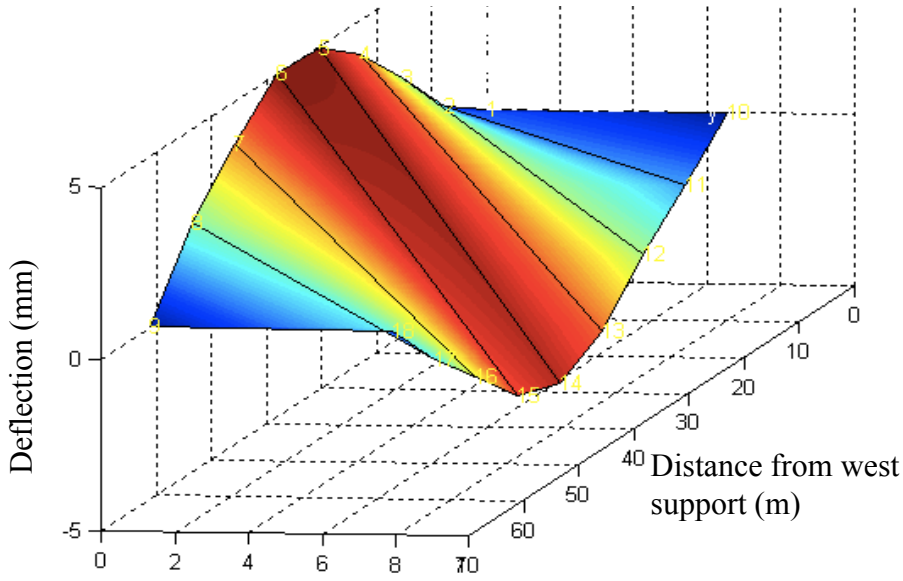

(b)

Figure 5.23. Graphical representation of the measured modes shapes of the instrumented Traffic Bridge span: (a) mode 1, (f_o = 2.71 Hz); and (b) mode 2, (f_o = 5.34 Hz).

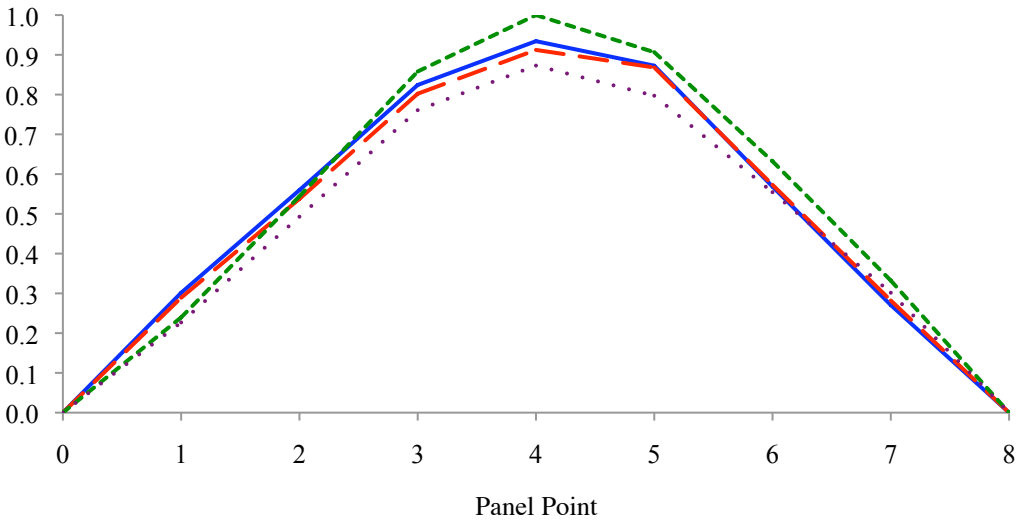

(a)

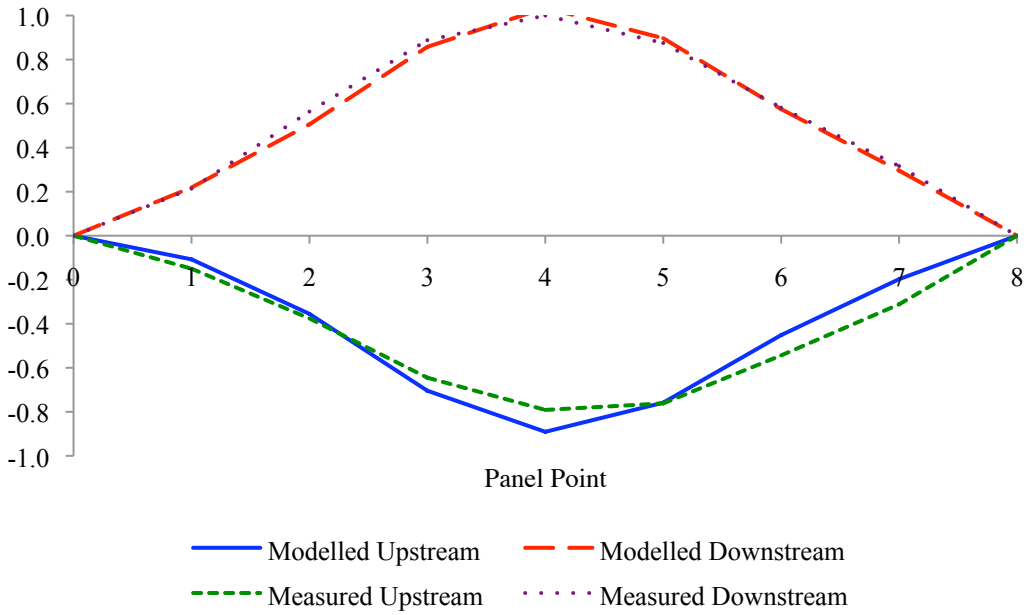

(b)

Figure 5.24. Modelled vs. measured mode shapes: (a) mode 1, (f_o =2.72 Hz, MAC =0.9945); (b) mode 2 (f_o =5.38 Hz, MAC = 0.9922).

6 SUMMARY AND CONCLUSIONS

6.1 SUMMARY

The Traffic Bridge, a 100-year old through-truss bridge spanning the South Saskatchewan River in Saskatoon, Saskatchewan, has sustained significant deterioration to its bottom chord and deck structural elements. The advanced state of deterioration, combined with the addition of a post-tensioning system along the bottom chord as well as a number of other alterations made over the last several decades, has resulted in a significant degree of uncertainty regarding the structural behaviour of the bridge, particularly with respect to how load is shared among the bottom chord and deck elements. This study focused on the use of strain gauge experimental data, in combination with an FE model, to (a) determine the load paths within the bridge, (b) identify the most appropriate FE modelling techniques, and (c) investigate ways to track ongoing deterioration using structural health monitoring. The first interior span from the south abutment of the bridge was instrumented. It was selected because of its larger span, which was expected to result in higher measureable forces, and because of its ease of access from the south riverbank for installation of the gauges.

In order to obtain an accurate representation of the load paths using strain gauge data, an estimate of the members' sectional properties must be known with a relatively high degree of certainty so that forces can be reliably determined. Unfortunately, the deteriorated members at the deck level which were of most interest in terms of potential alternate load paths within the truss-deck system happened to be the very members whose properties were known with the least certainty. As a result, the identification of actual load carrying mechanisms from the measured data proved to be challenging.

6.1.1 Experimental Data

Two types of experimental data were obtained: (a) strain-time histories obtained during controlled loading scenarios; and (b) the vertical acceleration response at panel points, obtained during ambient traffic loading. The strain-time histories were used primarily to determine the structural behaviour, and to refine the FE model. The

acceleration data were used only to refine the FE model; no attempt was made to use the acceleration data for damage detection.

The experimental strain data were gathered during controlled loading scenarios, with several loading trials conducted for each vehicle speed and direction considered, while the vehicle weight remained constant. The purpose of these controlled loading scenarios was to generate data that could be used to ascertain load paths, and provide a basis of comparison for FE simulations under identical loading scenarios.

Prior to comparing the measured results to those generated by FE modelling, the strain-time histories were analyzed to determine the type of forces that were present in the members; the truss members were anticipated to experience primarily axial forces, while the instrumented car joists were anticipated to experience primarily bending due to direct loading. However, the car joists, as part of the deck membrane system, were also suspected to provide an alternate load path for a portion of the tensile forces that the bottom chord members were designed to carry. The strain-time history data from the car joists were then used to track the neutral axis and curvature of these joists to determine whether axial forces were present, in addition to flexural effects. The presence of axial forces would indicate that the car joists were participating in providing an alternate load path for the tensile bottom chord truss forces.

6.1.2 FE Model

The results of the FE simulated loading scenarios were then compared against the strain-time history results. The challenge in this exercise was to estimate an accurate cross-sectional area for the instrumented bottom chord members, since it was impossible to measure the remaining net section accurately due to the significant deterioration. Pristine section properties were used in the initial analyses, and then altered during the refinement of the FE model based on comparisons with experimental data.

Using the force-time histories inferred from the strain measurements as a point of reference, the FE model was systematically altered in an attempt to match the measured forces. The modelling parameters that were modified included the support conditions, connection rotation fixity of the top and bottom chord members, deck member elevations, deck stiffness, floor beam stiffness, and finally, the stiffness of the bottom chord members, which were reduced to simulate damage.

The model was calibrated to best match the measured results, based on the modelling parameter modification analyses. This final model was then used as a basis of comparison to modify the measurement-inferred peak member forces through the use of scaling factors that accounted for section loss and other uncertainties. These scaled results can then be used as a baseline for possible future monitoring.

6.2 CONCLUSIONS

Using the experimental strain measurements alone and in combination with the numerical analyses, provided insight into the structural behaviour of the Traffic Bridge. It was found that the structure experienced little or no dynamic amplification, which corresponded well with previous studies on similar bridges (O'Connell and Dexter 2001, Laman et al. 1999).

During the controlled loading trials, once the control vehicle was past the instrumented span, the bottom chord members experienced non-zero strain readings. This suggests some level of structural redundancy at the deck level, with the deck participating in resisting some portion of the load, since it was only members at this level that deviated from the expected determinate behaviour. Again, this finding corresponded with previous a study (De Corte and Van Bogaert 2006). The FE model was not able to simulate this response, possibly since it did not consider the deck as a viscoelastic material that had the potential to slowly release the strain, once unloaded.

The level to which the floor joists participated with the bottom chords to resist the axial tensile loads remains uncertain. The neutral axis of the instrumented floor joists did not remain stationary during passage of the control vehicle, indicating that some level of axial forces was present in the joists. However, this shift in the neutral axis location could also have resulted from the deck participating in resisting bending moments through composite action when loaded directly, and that the degree of composite action may have varied in a nonlinear manner depending on such factors as the level of friction that could be mobilized between the joists and the deck.

There remains some uncertainty regarding the effectiveness of the post-tensioning (PT) system installed in 2006 to relieve the deteriorated bottom chord members of a portion of axial tensile forces. The PT system was designed to limit the amount of self-weight tensile forces directed through the bottom chord members, since this comprises

approximately 60-70% of the axial forces present in the truss members. Although the strain gauges were installed after the PT system was in place, it was believed that the difference between live load tensile forces in the bottom chord members on either side of the PT bulkhead would represent the portion of the axial force resisted by the PT system. The experimental results suggested an approximate force reduction of 28% in the bottom chord members due to the PT system under transient loading, while the numerical analysis estimated a 12% axial force reduction. The difference between the experimental and numerical analyses could simply be due to an inaccurate estimate of bottom chord cross-sectional areas used to convert measured strains into forces, or to the fact that the modelled stiffness of various elements along the load paths may not have been representative of the actual stiffness.

Although a truss bridge would seem to be a relatively simple structure, its response proved not to be so simple to simulate using FE analysis. Modifying the modelling parameters provided some insight as to how to more accurately model this seemingly simple structure. It was found that modifying the modelling parameters resulted in a negligible change in the axial loads in the top chord, diagonal, and vertical members. However, the modifications altered the simulated bottom chord axial forces significantly. The reason for the changes in the bottom chord axial forces with modelling variations was evidently that the FE model featured alternate load paths at the level of the deck.

It was found that support conditions were best represented by ideal pin/roller supports. The addition of springs installed at the supports to simulate the restraint caused by possible bearing seizure resulted in a greater difference between the modelled and measured axial forces. The springs limited the longitudinal movement of the bottom chord members, thereby reducing the tensile axial forces in the bottom chord members by inducing compression forces.

Although the top and bottom chord members are composed of relatively heavy structural members and rigid connections, modelling results indicated that very little, if any, moment transfer occurs at these connections. Modelling the top and bottom chord members with fixed connections elevated the axial forces of the bottom chord members well beyond the forces that were calculated using measured strains and assumed pristine

section properties. It is believed that an unreasonable increase in the stiffness of the top and bottom chord members was produced when fixed connections were assumed, limiting possible load redistribution to the deck and resulting in the bottom chord members taking the majority of the tensile forces. Although fixing the top and bottom chord member connections resulted in a less accurate model, the results indicated that there must be some form of redundancy at the deck level of the actual structure, since the measured "pristine" axial forces in bottom chord members were less than the modelled forces under these conditions.

Raising the elevation of the various deck elements to match their actual locations in the real structure also elevated the bottom chord axial forces well above those inferred from strain measurements assuming pristine section properties. The elements used to connect members at different elevations apparently did not provide realistic force transfer between the deck and the joists, and between the joists and the floor beams. This resulted in a modelled deck system that was not as stiff as the actual system. As a result, the bottom chord members resisted the majority of the tensile axial forces in this model.

Altering the deck membrane stiffness changed the distribution of forces in the bottom chord members. An increase in deck stiffness decreased the axial forces in the bottom chord members since the deck attracted a higher proportion of the force. The inversely proportional relationship was clearly represented by the FE model. However, matching the stiffness of the deck to accurately represent the actual structure was not an easy task. Changes to the stiffness did not consistently improve the correlation between the FE model and the measured results, so a final modulus of 10,000 MPa was used to represent the wood deck because it was deemed to be a realistic value.

It was found that the lateral stiffness of the floor beams running perpendicular to the main trusses also affected the effectiveness of alternate load paths present at the deck level. The greater the lateral stiffness of the floor beams, the greater the portion of the tensile force that was transferred from the bottom chord members to the stringers and deck. The stringers adjacent to the bottom chord members received the greatest proportion of the tensile forces, while the stringers near the centre of the deck received negligible axial forces. It was determined that an effective lateral stiffness of 50% of the

actual total section stiffness was a reasonable value to represent the behaviour; it was reasoned that, due to the slenderness of the floor beams, only half of the lateral stiffness could be effectively engaged to transfer forces laterally from the bottom chord to the stringers.

The final model that was deemed to most accurately represent the actual structural behaviour was composed of the following characteristics:

- pin/roller supports;
- pinned connections throughout;
- pristine member section properties for all members, with the exception of the bottom chord members, whose properties were reduced to of 80% the relative to pristine section properties (this bottom area reduction was an estimate only as the actual remaining net section remains unknown);
- floor beam lateral stiffness was modified to a value of 50% the pristine moment of inertia about the vertical axis;
- a deck modulus of elasticity of 10,000 MPa; and
- the deck members modelled at the same elevation as the bottom chord members.

It was found that the presence of redundant load paths at the deck level in the model influenced the possibility of using strain gauges for damage detection. When one bottom chord member was damaged in the model, the axial force decreased noticeably for the damaged member only, while the surrounding truss members experienced a negligible change in axial load. This result could not be verified during the experimental trials because the focus of this study was on non-destructive testing.

To summarize, the combination of experimental and numerical analyses contributed to a better understanding of the structural behaviour of the Traffic Bridge. The PT system was effective in reducing the bottom chord measured force by approximately 28%, although the FE model estimated a reduction of only 12% due to transient loading. It appears that the deck members assisted the bottom chord by providing an alternate load path for the tensile forces, but exactly which members participate, and to what extent, remains uncertain.

It is thought that the final model could be used as a baseline for future monitoring programs, potentially to detect damage by monitoring the strain distributions between the truss members, as well as between components of the built-up members. Unfortunately, the possibility of detecting a noticeable change in strain distribution is small, considering the low level of redundancy available and the considerable uncertainties that are involved in estimating both measured and modelled forces. However, there is still a potential to detect damage using strain gauges for a structure such as the Traffic Bridge, providing alternate load paths are available. Stain gauges would be best used to detect damage at the deck level, because that is the only location where redundancy has the potential to occur. Any change in the strain measurements in the elements of the deck assembly would indicate a change in stiffness, revealing locations where damage has occurred.

6.3 FUTURE RESEARCH

It would benefit the experimental program to measure, not just the response of the car joists, but also that of the edge deck stringers. The FE model predicted a significant level of axial force transfer from the bottom chord member, through the floor beam, to the edge stringers. By measuring the actual load distribution in the stringers, a better understanding of the actual participation of these elements in carrying bottom chord tension forces could be realized. In addition, a more accurate lateral floor beam stiffness and deck stiffness could be estimated, to create an FE model that represents the actual behaviour of the truss with greater certainty.

Perhaps during the decommissioning of the Traffic Bridge, destructive testing could be done to further understand the structural behaviour of this, and similar, structures. Monitoring the strains in the component members while causing damage to one of the components, or to an entire member, would help to clarify the possibility of detecting damage using the strain distributions. It would also help to determine more definitively, what members the forces are transferred to when damage occurs in the deck members. This could be accomplished by installing strain gauges on all of the car joists, edge and intermediate joists, as well as the bottom chord members, while systematically causing damage to deck members.

REFERENCES

Saskatoon Public Schools (http://olc.spsd.sk.ca/DE/resources/bridges/photogal.htm). Traffic Bridge Photos. Web May, 2009.

ANSYS Inc. 2007. ANSYS Release 9.0. Canonsburg, PA, USA.

AASHTO, 1990. Guide specifications for fatigue evaluation of existing steel bridges. AASHTO, Washington, D.C.

AASHTO, 1999. Standard specification for highway bridges, 16th Ed. With 1999 Interim Revisions. American Association of State Highway and Transportation Officials, AASHTO, Washington, D.C.

Alampalli, S., and Lund, R. 2006. Estimating fatigue life of bridge components using measured strains. ASCE Journal of Bridge Engineering, **11**(6): 725–736.

Allemang, R., 2003. The modal assurance criterion – twenty years of use and abuse. Proceedings from the 20th International Modal Analysis Conference, Los Angeles, CA, 14-21.

Azizinamini, A. 2002. Full scale testing of old steel truss bridge. Journal of Constructional Steel Research, **58**: 843-858.

Bakt, B., and Jaeger, L. 1990. Bridge testing – a surprise every time. Journal of Structural Engineering, **116**(5): 1370–1383.

Caglayan, B.O., Ozakgul, K., and Tezer, O. 2008. Fatigue life evaluation of a through-girder steel railway bridge. Engineering Failure Analysis, **16**(3): 765-774.

Cardini, A.J., and DeWolf, J. 2009. Long-term structural health monitoring of a multi-girder steel composite bridge using strain data. Structural Health Monitoring, An International Journal, **8**(1): 47-58.

Catbas F.N., Susoy, M., and Frangopol, D.M. 2008. Structural health monitoring and reliability estimation: Long span truss bridge application with environmental monitoring data. Journal of Engineering Structures, **30**: 2347-2359.

Chan, T.H.T., Li, Z.X., and Ko, J.M. 2001. Fatigue analysis and life prediction of bridges with structural health monitoring data – Part II: application. International Journal of Fatigue, **23**: 55-64.

City of Saskatoon. 2008. Traffic Characteristics Report.

De Corte, W., and Van Bogaert, P. 2006. The use of continuous high-frequency strain gage measurements for the assessment of the role of ballast in stress reduction on steel

railway bridge decks. Insight-non-destructive Testing & Condition Monitoring, **48**(6): 352-356.

DelGrego, M.R., Culmo, M.P., and DeWolf, J.T. 2008. Performance evaluation through field testing of century-old railroad truss bridge. ASCE Journal of Bridge Engineering, **13**(2): 132-138

Doebling, S.W., Farrar, C.R., and Prime, M.B. 1998. A summary review of vibration-based damage identification methods. Shock and Vibration Digest, **30**(2): 91-105.

Earthtech, 2003. Victoria Avenue Bridge – detailed inspection. City of Saskatoon, SK.

Enevoldsen, I., Pedersen, C., Axhag, F., Johansson, Ö., and Töyrä, B., 2002. Assessment and measurement of the Forsmo Bridge, Sweden. Structural Engineering International, **12**(4): 254-257.

Federal Highway Administration. 2001. Reliability of Visual Inspection for Highway Bridges, Volume I: Final Report, and Volume II: Appendices. Report Nos. FHWA-RD-01-020 and FHWA-RD-01-021, Washington, DC.

He, X., Yu, Z., and Chen, Z., 2008. Finite element model updating of existing steel bridge based on structural health monitoring. Journal of Central South University of Technology, **15**(3): 399-403.

Laman, J.A., Pechar, J.S., and Boothby, T.E. 1999. Dynamic load allowance for through-truss bridges. ASCE Journal of Bridge Engineering, **4**(4): 231-241

Li, Z.X., Chan, T.H.T., and Zheng, R. 2003. Statistical analysis of online strain response and its application in fatigue assessment of a long-span steel bridge. Engineering Structures, **25**: 1731-1741.

Liu, M., Frangopol, D.M., and Kim, S. 2009. Bridge system performance assessment from structural health monitoring: a case study. ASCE Journal of Structural Engineering, **135**(6): 733-742.

Matlab 2009. The Mathworks, Inc. 2009. MATLAB v7.8 R2009a Users Manual. Massachusetts, USA.

Nagavi, R.S., and Aktan, A.E. 2003. Nonlinear behavior of heavy class steel truss bridges. ASCE Journal of Structural Engineering, **129**(8): 1113-1121.

O'Connell, H.M., and Dexter, R.J. 2001. Response and analysis of steel trusses for fatigue truck loading. ASCE Journal of Bridge Engineering, **6**(6): 628-638.

Omenzetter, P., and Brownjohn, J.M.W., 2006. Application of time series analysis for bridge monitoring. Smart Materials and Structures, **15**: 129-138.

Peeters B., Maeck, J. and De Roeck, G. 2001. Vibration-based damage detection in civil engineering: excitation sources and temperature effects. Smart Materials and Structures, 10: 518-527

Penny, J.E.T., Friswell, M.I., and Garvey, S.D. 2003. Detecting aliased frequency components in discrete Fourier transforms. Mechanical Systems and Signal Processing, **17**(2): 473-481.

Stantec, 2005. Victoria Avenue Bridge – Detailed Inspection, City of Saskatoon, SK.

Van den Branden, B., Peeters, B., De Roeck G. 1999. Introduction to MACEC 2, Modal Analysis of Civil Engineering Constructions, Department of Civil Engineering. K.U. Leuvwen.

Wardrop, 2006. Victoria Avenue Bridge – Steel Inspection and Assessment Report, City of Saskatoon, SK.

APPENDIX A

TRAFFIC BRIDGE ORIGINAL DRAWINGS

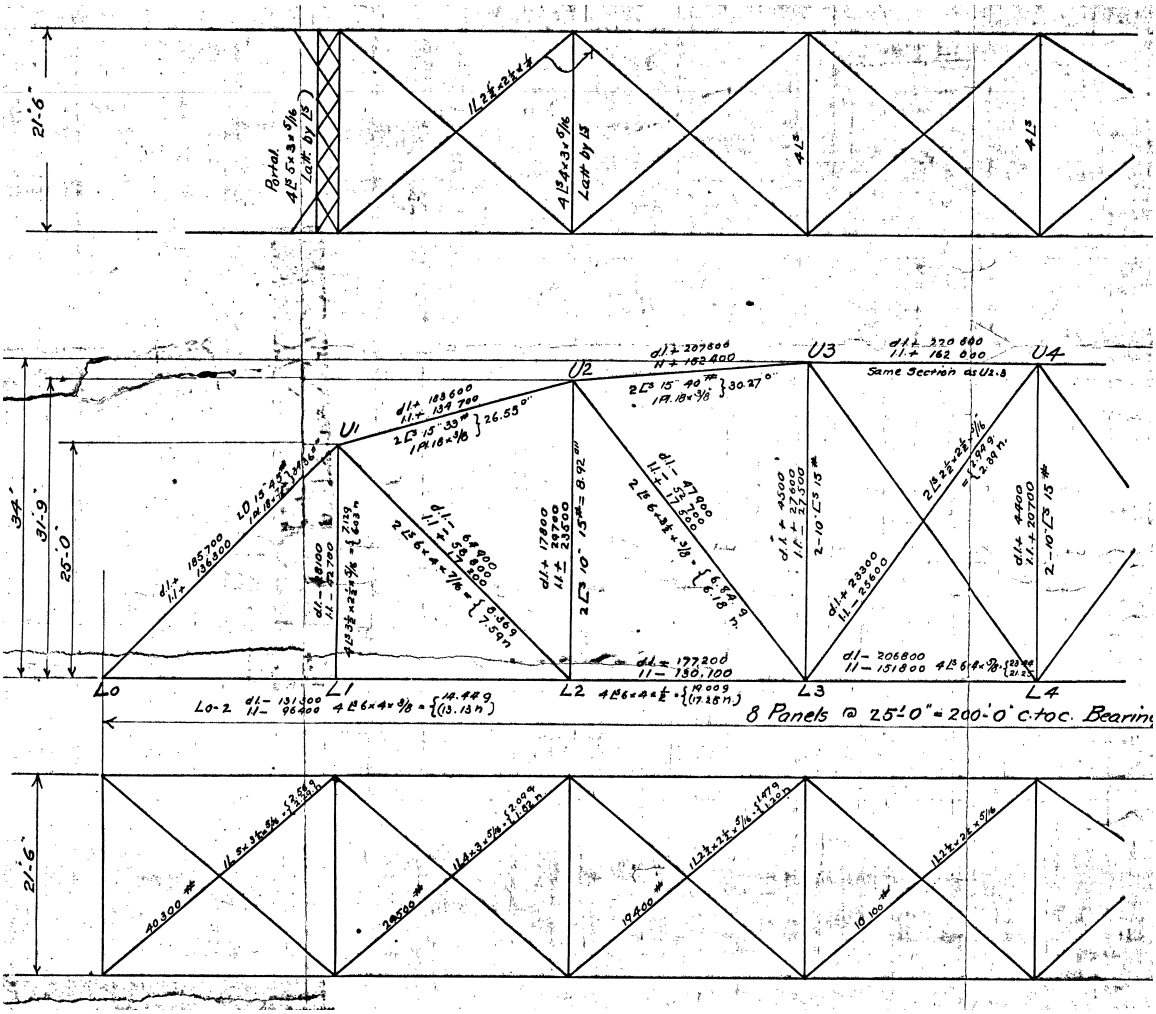

Figure A.1. Typical Plans and Elevations of the Traffic Bridge (Drawing 104-0201-004, 1906).

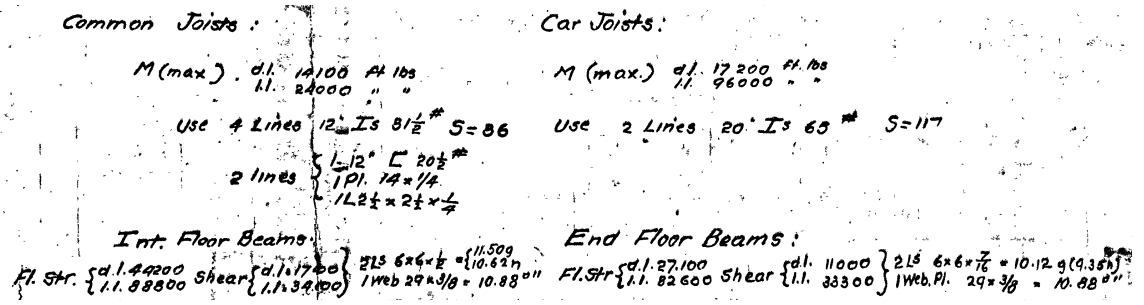

Figure A.2. Text on original drawings describing deck members (Drawing 104-0201-004, 1906).

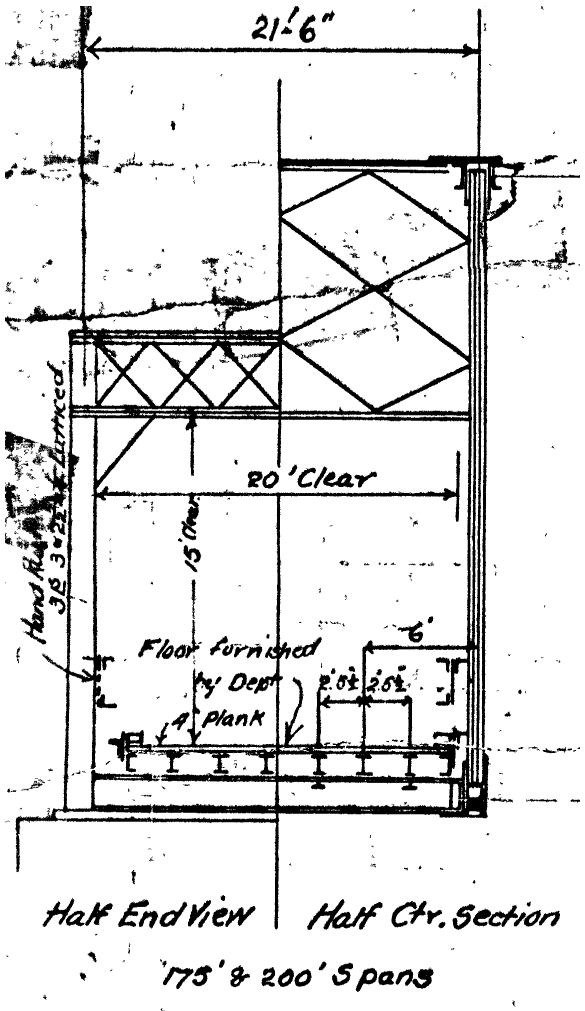

Figure A.3. Section of span (Drawing 104-0201-004, 1906).

APPENDIX B
EXPERIMENTAL INFORMATION

B.1 INTRODUCTION

This appendix lists the information related to the strain gauge installation, and controlled loading scenarios.

B.2 STRAIN GAUGE INSTALLATION

Table B.1 contains the installation data for the strain gauges. The bottom chord and top chord member location is measured from the outside edge of the member (members Aa, Ab, B, Ca, and Cb as shown in Figures 3.3 and 3.4). The car joist installed distance is measured from the midpoint between the top and bottom flanges.

Table B.1. Strain gauge installation information.

Member	Location	Description	Installed Dist. (mm)	Estimated Member thickness (mm)
L0L1	Aa	1	121	full
		2	centered	full
		3	centered	full
L0U1	Ab	1	121	full
		2	centered	full
		3	centered	full
U2U3	Aa	1	121	full
		2	centered	full
		3	centered	full
		1	121	full
		2	centered	full
		3	centered	full
L0U1	B	1	51	10
		2	51	10
		3	51	6
		4	76	10
		5	38	unknown
		6	38	unknown
		7	45	unknown
		8	51	unknown
L0L1	Ca	1	51	11
		2	51	9
		3	76	7
		4	67	9.5
L0L1	Cb	1	42	8.2
		2	51	9

		3	83	7
		4	51	4.8
L1L2	Ca	1	51	8
		2	51	8
		3	51	4
		4	51	7
L2L3	Ca	1	51	12
		2	51	11
		3	51	10
		4	51	9
L2L3	Cb	1	110	12
		2	51	11
		3	80	12
		4	51	10
L1U1	D	1	centered	full
		2	centered	full
		3	centered	full
		4	centered	full
L2U2	D	1	centered	full
		2	centered	full
U1L2	E	1	centered	full
		2	centered	full
L0L1	Fa	1	-152	full
		2	0	full
		3	152	full
L0L1	Fb	1	-152	full
		2	0	full
		3	152	full
L1L2	Fa	1	-152	full
		2	0	full
		3	152	full
L1L2	Fb	1	-152	full
		2	0	full
		3	152	full
L2L3	Fa	1	-152	full
		2	0	full
		3	152	full
L2L3	Fb	1	-152	full
		2	0	full
		3	152	full
Dummy2			centered	full
Dummy3			centered	full
Dummy4			centered	full
Dummy5			centered	full

B.3 CONTROL VEHICLE INFORMATION

There were two days in which the bridge was closed to permit controlled loading. The first day was July 8th, 2008 and the second was on May 2nd, 2009. The individual truck axle weights were measured on the first day, but only the total vehicle weight was measured on the second day. The same vehicle was used on both days, although the

loading of the vehicle varied slightly. For the July 8th measurements, axle weights were measured four separate times using the same scale. The measurements are listed in Table B.2. The total weight of the vehicle was distributed to the two axles: 33% of the total weight to the front axle (axle 1); and 67% of the total weight to the rear axle (axle 2).

Table B.2. Truck axle weights from July 8th, 2008.

Trial	Axle 1 (kg)	Axle 2 (kg)
1	2020	4170
2	1990	3880
3	1930	3830
4	1810	3750
average	1938	3908

Since the truck axles were not weighed individually for the vehicle that was used in the May 2nd, 2009 controlled load trials, the total weight of 5 tonnes (49 kN), measured by the City of Saskatoon, was split between the axles to the same distribution as what was measured on July 8th. The axle weights used in the model to simulate the measured results were 16 kN for the front axle, and 32.8 kN for the rear axle.

APPENDIX C

MATLAB ANALYSIS ROUTINES

C.1 MATLAB ROUTINE FOR READING STRAIN-TIME HISTORY

The strain data file consisted of a separate column for each strain gauge. The first four columns were the data from the four dummy gauges. Columns five to twelve were the data from the downstream bottom chord member between the first panel point and the post-tensioning bulkhead (L0L1_B). The data columns corresponding to the instrumented member location is listed in the routine below with the heading "% Individual Instrument locations". The last column (column 71) was the time that the measurement was taken, which was deleted from the data conditioning.

```
fs=500;            % sampling frequency
% Define raw data (linear regression?):

l=12900;
data_file=May2_30km_W3;
data_file(:,71)=[];                    % deletes the last column of data (time)

% Choose length over which to zero data:
zero_data=data_file;
zero_data(2*fs:l,:)=[];    % deleting but the first 10 s of the data

% Zero data (linear regression):

data_Z=data_file-ones(l,1)*mean(zero_data);

% Time length Plot:
t=1/fs:1/fs:(1/fs)*l;

% Lowpass filter to remove frequencies over 50Hz. 3rd order.
flp=50;
order=3
[a,b,c]=butter(order,flp/(0.5*fs),'low');
[sosl,gl]=zp2sos(a,b,c);
Hd_lp=dfilt.df2tsos(sosl,gl);

% Lowpass Filter Implementation:
data=filter(Hd_lp,data_Z);


% Individual Instrument locations:
DUMMYu=[data(:,1),data(:,2),data(:,3),data(:,4)];
```

```
L0L1_Bu=[data(:,5),data(:,6),data(:,7),data(:,8),data(:,9),data(:,10),data(:,11),data(:,12)];
L0L1_Cau=[data(:,13),data(:,14),data(:,16)]; % 3rd data flatlines
L0L1_Cbu=[data(:,17),data(:,18),data(:,19),data(:,20)];
L1L2_Cau=[data(:,21),data(:,22),data(:,23),data(:,24)];
L2L3_Cau=[data(:,25),data(:,26),data(:,27),data(:,28)];
L2L3_Cbu=[data(:,29),data(:,30),data(:,31),data(:,32)];
L0U1_Aau=[data(:,33),data(:,34),data(:,35)];
L0U1_Abu=[data(:,36),data(:,37),data(:,38)];
U2U3_Aau=[data(:,39),data(:,40),data(:,41)];
U2U3_Abu=[data(:,42),data(:,43),data(:,44)];
L1U1_Du=[data(:,45),data(:,46),data(:,47),data(:,48)];
L2U2_Du=[data(:,49),data(:,50)];
U1L2_Eu=[data(:,51),data(:,52)];
L0L1_Fau=[data(:,53),data(:,54),data(:,55)];
L0L1_Fbu=[data(:,56),data(:,57),data(:,58)];
L1L2_Fau=[data(:,59),data(:,60),data(:,61)];
L1L2_Fbu=[data(:,62),data(:,63),data(:,64)];
L2L3_Fau=[data(:,65),data(:,66),data(:,67)];
L2L3_Fbu=[data(:,68),data(:,69),data(:,70)];

% Decimating the data:
for i=1:1:70;
dec=100;
datam(:,i)=10^6*decimate(data_Z(:,i),dec);
end
% Time length Plot:
td=1/(fs/dec):1/(fs/dec):(1/(fs/dec))*(l/dec);

DUMMY=[datam(:,1),datam(:,2),datam(:,3),datam(:,4)];
L0L1_B=[datam(:,5),datam(:,6),datam(:,7),datam(:,8),datam(:,9),datam(:,10),datam(:,11),datam(
:,12)];
L0L1_Ca=[datam(:,13),datam(:,16)]; % 2nd data wonky & 3rd data flatlines
L0L1_Cb=[datam(:,17),datam(:,18),datam(:,19),datam(:,20)];
L1L2_Ca=[datam(:,21),datam(:,22),datam(:,23),datam(:,24)];
L2L3_Ca=[datam(:,25),datam(:,26),datam(:,27),datam(:,28)];
L2L3_Cb=[datam(:,29),datam(:,30),datam(:,31),datam(:,32)];
L0U1_Aa=[datam(:,33),datam(:,34),datam(:,35)];
L0U1_Ab=[datam(:,36),datam(:,37),datam(:,38)];
U2U3_Aa=[datam(:,39),datam(:,40),datam(:,41)];
U2U3_Ab=[datam(:,42),datam(:,43),datam(:,44)];
L1U1_D=[datam(:,45),datam(:,46),datam(:,47),datam(:,48)];
L2U2_D=[datam(:,49),datam(:,50)];
U1L2_E=[datam(:,51),datam(:,52)];
L0L1_Fa=[datam(:,53),datam(:,54),datam(:,55)];
L0L1_Fb=[datam(:,56),datam(:,57),datam(:,58)];
L1L2_Fa=[datam(:,59),datam(:,60),datam(:,61)];
L1L2_Fb=[datam(:,62),datam(:,63),datam(:,64)];
L2L3_Fa=[datam(:,65),datam(:,66),datam(:,67)];
L2L3_Fb=[datam(:,68),datam(:,69),datam(:,70)];
```

```
% Averaged Locations

DUM=sum(DUMMY,2)*(1/4);
B=sum(L0L1_B,2)*(1/8);
Ca1=sum(L0L1_Ca,2)*(1/2);
Cb1=sum(L0L1_Cb,2)*(1/4);
Ca2=sum(L1L2_Ca,2)*(1/4);
Ca3=sum(L2L3_Ca,2)*(1/4);
Cb3=sum(L2L3_Cb,2)*(1/4);
Aa1=sum(L0U1_Aa,2)*(1/3);
Ab1=sum(L0U1_Ab,2)*(1/3);
Aa3=sum(U2U3_Aa,2)*(1/3);
Ab3=sum(U2U3_Ab,2)*(1/3);

D1=sum(L1U1_D,2)*(1/4);
D2=sum(L2U2_D,2)*(1/2);
E=sum(U1L2_E,2)*(1/2);
Fa1=sum(L0L1_Fa,2)*(1/3);
Fb1=sum(L0L1_Fb,2)*(1/3);
Fa2=sum(L1L2_Fa,2)*(1/3);
Fb2=sum(L1L2_Fb,2)*(1/3);
Fa3=sum(L2L3_Fa,2)*(1/3);
Fb3=sum(L2L3_Fb,2)*(1/3);
BC=[B,Ca1,Ca2,Ca3];
FJ=[Fa1,Fb1,Fa2,Fb2];
V=[D1,D2,E];
```

C.2 MATLAB ROUTINE FOR LINEAR REGRESSION OF CAR-JOIST STRAIN GAUGES

The purpose of this routine was to track the location of the neutral axis with respect to time for the duration that the control vehicle was on the span. A change in location of the neutral axis could indicate that the car joists participate to resist forces other than that of bending due to direct loading.

```
% Linear Regression for: L0L1_Fa

% Define active data (strain data) (y-axis):
y1=data(:,53);
y2=data(:,54);
y3=data(:,55);

% height is from middle, the gauges are spaced 6" apart. (x-axis):
x1=450;
x2=300;
x3=150;

% Linear regression for 3 points:
for i=1:1:l;        % i = increment, dt = 0.02 for 500 Hz.
```

```
Sx2=(x1)^2+(x2)^2+(x3)^2;
Sx=x1+x2+x3;
Sy(i)=y1(i)+y2(i)+y3(i);
Sy2(i)=(y1(i))^2+(y2(i))^2+(y3(i))^2;
Sxy(i)=(x1*y1(i))+x2*y2(i)+(x3*y3(i));
n=3;

a1(i)=(Sx2*Sy(i)-Sx*Sxy(i))/(n*Sx2-(Sx)^2);
b1(i)=(n*Sxy(i)-Sx*Sy(i))/(n*Sx2-(Sx)^2);

na1(i,:)=-a1(i)/b1(i);
% Strain distribution based on neutral axis (na1) and slope (b):

e1_1(i)=a1(i)+b1(i)*x1;
e2_1(i)=a1(i)+b1(i)*x2;
e3_1(i)=a1(i)+b1(i)*x3;

% determine distance from neutral axis of each gauge wr to time:

xe1_1(i)=-(na1(i)-x1);
xe2_1(i)=-(na1(i)-x2);
xe3_1(i)=-(na1(i)-x3);

% Determine variance:

error1_1(i)=y1(i)-a1(i)-b1(i)*x1;
error2_1(i)=y2(i)-a1(i)-b1(i)*x2;
error3_1(i)=y3(i)-a1(i)-b1(i)*x3;

variance_1(i)=error1_1(i)^2+error2_1(i)^2+error3_1(i)^2;

% Standard deviation (sd):
sd_1(i)=(variance_1(i))^(1/2);

% Mean (ybar):
ybar_1(i)=abs((e1_1(i)+e2_1(i)+e3_1(i))/3);

% Coefficient of Variation (COV):
COV_1(i)=100*sd_1(i)/ybar_1(i);

COV_tot_1=mean(COV_1);

% Determine instantaneous correlation coefficient:
r1(i)=(n*Sxy(i)-Sx*Sy(i))/(((n*Sx2-Sx^2)*(n*Sy2(i)-(Sy(i))^2))^(1/2));  % equation (16-7) in
text
r1_before=r1;
r1_before(2.5*fs:l)=[];
r1_before_m=mean(r1_before);

r1_panel=r1;
```

```
r1_panel(4.5*fs:l)=[];
r1_panel(1:2.5*fs)=[];
r1_panel_m=mean(r1_panel);

r1_span=r1;
r1_span(11.4*fs:l)=[];
r1_span(1:2.5*fs)=[];
r1_span_m=mean(r1_span);

r1_after=r1;
r1_after(1:11.4*fs)=[];
r1_after_m=mean(r1_after);

end
```

APPENDIX D

SAMPLE ANALYSIS DATA

The analysis data in this appendix provides sample values used to determine the difference between measured and modelled axial forces. Listed in Tables D.1 through D.6 are the member axial forces for when the northbound control vehicles' rear axle was situated above the specified panel point, for panel points 1 to 7 (excluding the end panel points). Tables D.7 to D.12 contain the member axial forces for the southbound controlled loading scenarios. The measured axial force was calculated using Equation 3.4.

To obtain the modified measured (MF) values, the measured values were multiplied by a common factor, for each bottom chord member in order to match the peak axial force. Separate MF values were calculated for both the northbound and southbound trials, and then used to obtain average MF values specific to each bottom chord member.

Table D.1. Measured axial force for the northbound controlled loading scenario based on pristine member properties.

Northbound	Axial Force (kN)						
Panel point	*1*	*2*	*3*	*4*	*5*	*6*	*7*
LOL1-B	11.1	9.2	5.9	3.9	2.5	1.7	2.0
L0L1-Ca	8.8	7.0	4.3	2.6	1.4	0.8	1.0
L1L2-Ca	11.0	8.4	4.3	2.1	0.8	0.2	0.6
L2L3-Ca	7.6	19.5	15.8	9.8	6.2	3.3	1.9
L0L1-Cb	8.2	8.1	5.5	3.7	2.7	2.0	1.6
L2L3-Cb	6.2	13.3	11.7	8.0	5.0	2.7	1.4
L0U1-Aa	-28.8	-30.7	-25.0	-20.1	-15.1	-9.8	-4.7
L0U1-Ab	-28.8	-30.7	-25.0	-20.1	-15.1	-9.8	-4.7
U2U3-Aa	-13.6	-29.2	-39.9	-34.2	-25.2	-16.7	-8.2
U2U3-Ab	-7.5	-15.7	-21.7	-18.9	-14.0	-9.2	-4.5
L1U1-D	19.7	3.6	-0.6	-0.3	-0.3	-0.2	-0.2
L2U2-D	8.4	12.2	-6.1	-8.3	-5.9	-3.9	-1.9
U1L2-E	-5.3	14.1	15.2	12.0	9.0	5.9	3.0

Table D.2. Original FE member axial force for the northbound controlled loading scenario.

	Axial Force (kN)						
Panel point	1	2	3	4	5	6	7
LOL1-B	9.5	6.0	4.1	2.5	1.3	0.5	0.1
L0L1-Ca	9.2	5.5	3.5	1.9	0.8	-0.1	-0.3

L1L2-Ca	7.3	2.5	0.6	-0.6	-1.0	-1.1	-0.7
L2L3-Ca	4.3	13.0	7.7	3.7	1.7	0.5	0.0
L0L1-Cb	8.7	8.2	7.4	6.1	4.9	3.5	1.7
L2L3-Cb	3.6	6.3	4.1	3.1	2.3	1.3	0.6
L0U1-Aa	-41.9	-36.2	-29.9	-23.8	-17.6	-11.4	-5.2
L0U1-Ab	-41.5	-35.6	-29.3	-23.2	-17.2	-11.1	-5.2
U2U3-Aa	-18.0	-33.4	-44.7	-35.4	-26.2	-17.1	-7.9
U2U3-Ab	-7.2	-13.8	-19.3	-15.1	-11.2	-7.2	-3.3
L1U1-D	29.0	0.3	0.0	0.0	0.0	0.0	0.0
L2U2-D	11.4	14.7	-11.7	-9.5	-7.0	-4.6	-2.1
U1L2-E	-8.3	20.2	16.9	13.4	9.9	6.4	3.0

Table D.3. Spring support FE member axial force for the northbound controlled loading scenario.

	Axial Force (kN)						
Panel point	1	2	3	4	5	6	7
LOL1-B	8.1	4.4	2.3	0.8	-0.3	-1.0	-1.0
L0L1-Ca	7.9	4.0	1.9	0.3	-0.7	-1.4	-1.2
L1L2-Ca	6.5	1.5	-0.5	-1.7	-2.0	-2.0	-1.4
L2L3-Ca	3.6	12.1	6.7	2.7	0.7	-0.4	-0.7
L0L1-Cb	7.3	6.5	5.4	4.1	2.8	1.6	0.3
L2L3-Cb	2.9	5.5	3.2	2.2	1.4	0.5	0.0
L0U1-Aa	-41.9	-36.2	-29.9	-23.7	-17.6	-11.3	-5.2
L0U1-Ab	-41.5	-35.6	-29.3	-23.2	-17.2	-11.1	-5.1
U2U3-Aa	-18.0	-33.4	-44.7	-35.4	-26.2	-17.1	-7.9
U2U3-Ab	-7.1	-13.7	-19.3	-15.1	-11.2	-7.2	-3.2
L1U1-D	29.0	0.3	0.0	0.0	0.0	0.0	0.0
L2U2-D	11.4	14.7	-11.7	-9.5	-7.0	-4.5	-2.1
U1L2-E	-8.3	20.2	16.9	13.3	9.9	6.4	3.0

Table D.4. Fixed top chord and bottom chord FE member axial force for the northbound controlled loading scenario.

	Axial Force (kN)						
Panel point	1	2	3	4	5	6	7
LOL1-B	16.3	12.2	9.2	6.6	4.3	2.4	0.9
L0L1-Ca	15.5	11.2	8.0	5.3	3.1	1.3	0.2
L1L2-Ca	15.6	10.7	7.5	4.8	2.7	1.0	0.1
L2L3-Ca	12.6	23.8	17.9	12.6	8.3	4.6	1.7
L0L1-Cb	13.0	12.0	10.5	8.7	6.7	4.6	2.2
L2L3-Cb	9.4	14.9	12.1	9.9	7.3	4.6	2.1
L0U1-Aa	-42.1	-36.4	-30.1	-23.9	-17.7	-11.5	-5.2
L0U1-Ab	-41.6	-35.7	-29.3	-23.2	-17.2	-11.1	-5.1
U2U3-Aa	-18.4	-33.8	-44.5	-35.2	-26.0	-16.9	-7.7
U2U3-Ab	-7.3	-13.8	-19.0	-15.0	-11.2	-7.1	-3.2
L1U1-D	28.4	0.3	-0.1	0.0	0.0	0.0	0.0
L2U2-D	11.4	14.1	-11.7	-9.5	-6.9	-4.5	-2.1
U1L2-E	-7.4	20.1	16.9	13.3	9.8	6.4	2.9

Table D.5. Raised deck FE member axial force for the northbound controlled loading scenario.

	Axial Force (kN)						
Panel point	1	2	3	4	5	6	7
LOL1-B	17.8	13.7	10.1	7.1	4.6	2.4	0.9
L0L1-Ca	16.9	12.6	8.8	5.7	3.2	1.2	0.1
L1L2-Ca	17.5	11.7	8.0	4.8	2.5	0.7	-0.1
L2L3-Ca	13.9	26.2	19.3	13.3	8.4	4.4	1.5
L0L1-Cb	15.0	14.7	12.6	10.4	8.0	5.5	2.5
L2L3-Cb	10.8	15.3	12.9	10.5	7.6	4.6	2.0
L0U1-Aa	-42.1	-36.7	-30.2	-24.0	-17.8	-11.5	-5.3
L0U1-Ab	-41.6	-36.1	-29.4	-23.3	-17.3	-11.2	-5.1
U2U3-Aa	-18.4	-34.6	-44.6	-35.4	-26.1	-17.0	-7.7
U2U3-Ab	-7.7	-14.9	-19.4	-16.0	-11.7	-7.6	-3.4
L1U1-D	27.1	0.7	-0.3	0.0	0.0	0.0	0.0
L2U2-D	12.9	12.9	-11.3	-9.6	-6.9	-4.5	-2.1
U1L2-E	-6.2	19.9	17.2	13.4	9.9	6.4	2.9

Table D.6. Final Model member axial force for the northbound controlled loading scenario.

	Axial Force (kN)						
Panel point	1	2	3	4	5	6	7
LOL1-B	12.2	7.4	4.7	2.6	1.1	0.1	-0.2
L0L1-Ca	11.6	6.6	3.8	1.6	0.1	-0.8	-0.8
L1L2-Ca	11.3	5.2	2.0	-0.3	-1.4	-1.9	-1.4
L2L3-Ca	7.6	18.2	11.6	6.4	3.0	0.6	-0.4
L0L1-Cb	10.4	9.6	8.4	6.9	5.3	3.6	1.7
L2L3-Cb	5.2	8.4	5.9	4.6	3.2	1.7	0.7
L0U1-Aa	-41.9	-36.2	-30.0	-23.8	-17.6	-11.4	-5.2
L0U1-Ab	-41.5	-35.6	-29.3	-23.2	-17.1	-11.1	-5.1
U2U3-Aa	-18.4	-33.8	-44.5	-35.1	-26.0	-16.9	-7.7
U2U3-Ab	-7.4	-14.0	-19.3	-15.1	-11.2	-7.1	-3.2
L1U1-D	28.2	0.3	0.0	0.0	0.0	0.0	0.0
L2U2-D	11.5	13.8	-11.7	-9.5	-7.0	-4.5	-2.1
U1L2-E	-7.5	20.2	16.9	13.3	9.9	6.4	2.9

Table D.7. Measured axial force for the southbound controlled loading scenario based on pristine member properties.

	Axial Force (kN)						
panel point	7	6	5	4	3	2	1
LOL1-B	0.2	0.5	1.4	2.6	4.3	6.5	6.4
L0L1-Ca	0.2	0.4	0.8	1.7	2.9	4.6	4.8
L1L2-Ca	0.0	0.2	1.0	2.2	3.9	6.6	7.1
L2L3-Ca	0.9	2.1	4.3	7.1	10.0	10.9	5.2
L0L1-Cb	-0.2	-0.2	1.1	3.0	5.7	10.0	12.2
L2L3-Cb	0.6	2.6	6.1	11.2	18.5	22.0	7.6
L0U1-Aa	-2.4	-4.4	-6.6	-8.8	-10.8	-13.1	-11.6

L0U1-Ab	-2.4	-4.4	-6.6	-8.8	-10.8	-13.1	-11.6
U2U3-Aa	-4.7	-9.1	-13.9	-18.5	-19.7	-13.6	-6.0
U2U3-Ab	-10.1	-19.0	-27.7	-36.6	-41.7	-28.0	-12.4
L1U1-D	0.1	0.1	0.0	-0.1	-0.2	2.5	8.0
L2U2-D	-1.0	-1.9	-2.9	-3.9	-1.9	5.2	3.5
U1L2-E	1.4	2.8	4.3	5.7	7.0	5.2	-2.2

Table D.8. Original FE member axial force for the southbound controlled loading scenario.

	Axial Force (kN)						
panel point	7	6	5	4	3	2	1
LOL1-B	2.2	3.8	5.2	6.6	7.7	8.5	7.8
L0L1-Ca	2.0	3.5	4.9	6.2	7.3	8.2	7.6
L1L2-Ca	0.8	1.4	2.0	2.6	3.3	4.3	4.9
L2L3-Ca	0.7	1.4	2.2	3.4	5.4	6.5	2.4
L0L1-Cb	0.5	1.3	2.3	3.5	5.3	7.3	8.1
L2L3-Cb	0.3	1.1	2.6	4.7	8.4	11.0	2.7
L0U1-Aa	-2.8	-5.1	-7.3	-9.6	-12.2	-14.4	-13.9
L0U1-Ab	-2.8	-5.2	-7.6	-10.0	-12.5	-14.7	-14.0
U2U3-Aa	-4.4	-8.4	-12.4	-16.4	-18.0	-11.8	-5.3
U2U3-Ab	-10.7	-19.9	-28.9	-37.9	-43.4	-28.6	-13.3
L1U1-D	0.0	0.0	-0.1	-0.1	-0.1	2.3	11.3
L2U2-D	-1.2	-2.2	-3.3	-4.4	-2.5	6.8	3.4
U1L2-E	1.6	3.1	4.5	6.0	7.4	6.0	-4.5

Table D.9. Spring support FE member axial force for the southbound controlled loading scenario.

	Axial Force (kN)						
panel point	7	6	5	4	3	2	1
LOL1-B	1.9	3.4	4.4	6.1	7.2	8.1	7.5
L0L1-Ca	1.7	3.1	4.2	5.8	6.9	7.8	7.3
L1L2-Ca	0.6	1.1	1.6	2.3	3.1	4.1	4.7
L2L3-Ca	0.5	1.2	1.9	3.2	5.2	6.3	2.3
L0L1-Cb	0.2	0.9	1.7	3.1	4.9	6.9	5.7
L2L3-Cb	0.1	0.9	2.2	4.4	8.1	10.7	1.1
L0U1-Aa	-2.8	-5.1	-6.8	-9.6	-12.2	-14.4	-14.0
L0U1-Ab	-2.9	-5.3	-7.1	-10.0	-12.5	-14.7	-14.0
U2U3-Aa	-4.5	-8.5	-11.6	-16.4	-18.0	-11.8	-4.8
U2U3-Ab	-11.0	-20.2	-27.1	-37.9	-43.3	-28.6	-12.0
L1U1-D	0.0	0.0	-0.1	-0.1	-0.1	2.3	3.4
L2U2-D	-1.2	-2.3	-3.1	-4.4	-2.5	6.8	3.4
U1L2-E	1.7	3.1	4.2	6.0	7.4	6.0	-2.6

Table D.10. Fixed top chord and bottom chord FE member axial force for the southbound controlled loading scenario.

	Axial Force (kN)						
panel	7	6	5	4	3	2	1

point							
LOL1-B	3.3	5.7	7.3	9.7	11.5	12.9	11.4
L0L1-Ca	2.8	5.0	6.5	8.8	10.6	12.1	10.9
L1L2-Ca	2.3	4.3	5.7	7.9	9.5	11.0	10.0
L2L3-Ca	3.0	5.7	7.8	11.0	13.6	14.4	7.4
L0L1-Cb	0.8	2.3	4.0	6.6	9.6	12.7	14.0
L2L3-Cb	2.4	5.5	8.6	13.7	19.4	22.3	8.1
L0U1-Aa	-2.6	-4.9	-6.6	-9.4	-11.9	-14.1	-13.7
L0U1-Ab	-2.8	-5.2	-7.0	-9.9	-12.3	-14.5	-13.8
U2U3-Aa	-4.5	-8.4	-11.6	-16.3	-17.9	-11.7	-5.2
U2U3-Ab	-11.0	-20.2	-27.2	-38.2	-43.5	-28.8	-13.5
L1U1-D	0.0	0.0	0.0	0.0	-0.1	2.2	11.3
L2U2-D	-1.2	-2.2	-2.9	-4.2	-2.4	7.0	3.3
U1L2-E	1.6	3.0	4.1	5.8	7.2	5.9	-4.5

Table D.11. Raised deck FE member axial force for the southbound controlled loading scenario.

	Axial Force (kN)						
panel point	7	6	5	4	3	2	1
LOL1-B	3.5	6.2	8.2	11.2	13.4	15.6	13.1
L0L1-Ca	3.0	5.4	7.3	10.2	12.5	14.7	12.6
L1L2-Ca	2.4	4.5	6.3	8.9	11.0	13.0	11.5
L2L3-Ca	3.1	6.0	8.5	12.3	15.5	15.8	9.0
L0L1-Cb	1.0	2.8	4.7	7.6	11.1	15.1	16.9
L2L3-Cb	1.9	5.0	8.9	14.3	22.5	23.7	8.9
L0U1-Aa	-2.7	-5.0	-6.7	-9.6	-12.1	-14.9	-13.2
L0U1-Ab	-2.8	-5.3	-7.1	-10.1	-12.5	-15.3	-13.3
U2U3-Aa	-4.5	-8.5	-11.7	-16.8	-17.7	-11.9	-5.2
U2U3-Ab	-11.4	-20.8	-27.7	-39.5	-44.0	-29.6	-13.8
L1U1-D	0.0	0.0	0.0	-0.1	-0.5	3.6	10.1
L2U2-D	-1.1	-2.1	-2.9	-4.6	-1.4	6.2	3.9
U1L2-E	1.6	3.1	4.2	5.9	7.8	4.9	-3.5

Table D.12. Final Model member axial force for the southbound controlled loading scenario.

	Axial Force (kN)						
panel point	7	6	5	4	3	2	1
LOL1-B	1.9	3.5	4.7	6.6	8.2	9.6	9.2
L0L1-Ca	1.5	2.9	4.1	5.9	7.5	9.0	8.8
L1L2-Ca	0.5	1.3	2.2	3.6	5.2	6.9	7.4
L2L3-Ca	0.7	2.0	3.5	5.8	8.6	9.8	4.1
L0L1-Cb	0.9	2.1	3.2	5.1	7.3	9.5	10.1
L2L3-Cb	0.5	1.7	3.6	6.5	10.8	13.6	4.1
L0U1-Aa	-2.8	-5.1	-6.8	-9.6	-12.1	-14.4	-13.9
L0U1-Ab	-2.9	-5.3	-7.1	-10.0	-12.5	-14.7	-13.9
U2U3-Aa	-4.5	-8.4	-11.6	-16.4	-18.0	-11.7	-5.3
U2U3-Ab	-11.0	-20.3	-27.2	-38.1	-43.5	-28.8	-13.4
L1U1-D	0.0	0.0	-0.1	-0.1	-0.1	2.2	11.3

L2U2-D	-1.2	-2.3	-3.1	-4.4	-2.5	6.8	3.4
U1L2-E	1.7	3.1	4.2	5.9	7.4	6.0	-4.5

Table D.13 lists the values used to calculate the difference and coefficient of variation (COV) for the bottom chord member L0L1-B_d. Equation 5.5 was used to calculate the difference between the measured and modelled axial forces.

Table D.13. Sample steps in calculating the difference between measured and modelled axial forces for bottom chord member L0L1-B_d.

Member L0L1-B_d	Axial Force (kN)						
Panel Point	**1**	**2**	**3**	**4**	**5**	**6**	**7**
Measured	11.12	9.15	5.93	3.89	2.48	1.67	2.04
measured^2	123.7	83.8	35.1	15.1	6.1	2.8	4.1
rms measured	6.22						
Original	**9.50**	**5.97**	**4.06**	**2.51**	**1.35**	**0.46**	**0.06**
difference	1.63	3.18	1.86	1.38	1.13	1.21	1.97
difference^2	2.64	10.12	3.47	1.91	1.28	1.47	3.89
rms difference	1.88						
mean difference	1.77						
standard deviation	0.70						
COV	40%						
Overall Difference	30%						
Spring	**8.14**	**4.35**	**2.33**	**0.75**	**-0.31**	**-1.00**	**-0.96**
difference	2.99	4.80	3.60	3.14	2.79	2.67	2.99
difference^2	8.92	23.07	12.93	9.85	7.76	7.15	8.97
rms difference	3.35						
mean difference	3.28						
standard deviation	0.73						
COV	22%						
Overall Difference	54%						
Fixed	**16.30**	**12.24**	**9.25**	**6.60**	**4.34**	**2.38**	**0.90**
difference	5.18	3.08	3.32	2.71	1.86	0.71	1.14
difference^2	26.78	9.49	11.03	7.32	3.45	0.50	1.30
rms difference	2.92						
mean difference	2.57						
standard deviation	1.51						
COV	59%						
Overall Difference	47%						
Final	**12.19**	**7.44**	**4.75**	**2.60**	**1.13**	**0.11**	**-0.20**
difference	1.06	1.71	1.18	1.29	1.35	1.56	2.24
difference^2	1.13	2.94	1.39	1.67	1.82	2.44	5.00
rms difference	1.53						
mean difference	1.49						
standard deviation	0.40						
COV	27%						
Overall Difference	24%						

APPENDIX E

SAMPLE MEASURED DATA

The analysis data in this appendix provides sample strain values obtained from each controlled loading trial. Tables E.1 to E.8 list the strain values while the control load vehicle's rear axle was located at panel points 1 to 7, and the averaged strain between the identical loading trials. The axial forces can be found in Tables E.9 to E.10 calculated from the average strain, and the pristine member properties.

Table E.1. Static strain values for the northbound static controlled loading scenario.

		microstrain (με)						
Trial	Member	1	2	3	4	5	6	7
Static N1	LOL1-B	6.3	4.6	3.1	1.8	0.9	0.5	0.7
	L0L1-Ca	4.9	3.6	2.7	1.8	1.2	1.0	1.3
	L1L2-Ca	6.3	4.3	2.7	1.6	0.9	0.6	1.0
	L2L3-Ca	3.4	8.4	6.3	4.2	2.9	1.6	1.1
	L0L1-Cb	4.2	4.0	2.8	2.0	1.5	1.1	0.9
	L2L3-Cb	2.6	5.7	5.1	3.3	2.0	1.2	0.4
	L0U1-Aa	-5.3	-4.4	-3.3	-2.5	-1.7	-0.5	0.5
	L0U1-Ab	-7.1	-6.1	-4.6	-3.6	-2.6	-1.3	-0.2
	U2U3-Aa	-3.7	-7.3	-9.8	-8.0	-5.7	-3.3	-1.1
	U2U3-Ab	-2.0	-4.1	-5.9	-4.5	-3.2	-2.3	-0.7
	L1U1-D	20.8	-1.6	-3.9	-3.7	-3.7	-3.7	-3.5
	L2U2-D	7.3	9.3	-8.2	-8.1	-5.9	-4.2	-2.4
	U1L2-E	-4.1	15.7	14.5	11.7	9.1	6.1	3.4
Static N2	LOL1-B	5.7	3.4	1.8	0.6	-0.3	-0.8	-0.4
	L0L1-Ca	4.3	2.3	1.1	0.2	-0.4	-0.5	-0.3
	L1L2-Ca	5.8	3.1	1.2	-0.1	-0.7	-0.9	-0.5
	L2L3-Ca	3.0	8.1	5.3	3.1	1.8	0.8	0.3
	L0L1-Cb	4.4	3.6	2.0	1.0	0.6	0.3	0.0
	L2L3-Cb	2.6	5.1	4.1	2.7	1.5	0.6	0.1
	L0U1-Aa	-6.4	-5.8	-4.7	-3.7	-3.0	-2.1	-0.8
	L0U1-Ab	-7.5	-6.8	-5.5	-4.5	-3.5	-2.1	-0.9
	U2U3-Aa	-4.0	-8.0	-10.3	-8.5	-6.6	-4.2	-1.7
	U2U3-Ab	-2.0	-4.2	-5.6	-4.6	-3.3	-2.0	-0.9
	L1U1-D	24.9	1.5	0.4	0.3	0.1	0.3	0.2
	L2U2-D	9.2	10.5	-6.8	-6.7	-5.1	-3.1	-1.2
	U1L2-E	-4.8	16.1	13.7	10.8	8.2	5.2	2.2
Static N3	LOL1-B	6.1	3.7	1.9	0.5	-0.1	-0.5	-0.4
	L0L1-Ca	5.2	3.2	1.8	0.7	0.1	-0.2	-0.2
	L1L2-Ca	5.6	2.7	1.0	-0.1	-0.6	-0.8	-0.5
	L2L3-Ca	3.2	8.3	5.7	3.4	1.7	0.6	0.1
	L0L1-Cb	4.4	3.7	2.4	1.4	0.7	0.2	0.0
	L2L3-Cb	2.7	5.1	3.9	2.3	1.3	0.5	0.1

	L0U1-Aa	-5.9	-5.4	-4.6	-3.7	-2.4	-1.4	-0.5
	L0U1-Ab	-6.8	-6.5	-5.4	-4.5	-3.1	-1.9	-0.7
	U2U3-Aa	-3.7	-8.0	-10.3	-8.2	-5.8	-3.6	-1.5
	U2U3-Ab	-1.6	-3.6	-4.7	-3.8	-2.7	-1.7	-0.5
	L1U1-D	24.5	1.0	0.0	0.3	0.2	0.3	0.1
	L2U2-D	10.1	10.8	-6.5	-6.3	-4.4	-2.5	-1.0
	U1L2-E	-5.1	15.9	14.0	10.8	7.7	4.8	2.0
Average Static N	*LOL1-B*	*6.1*	*3.9*	*2.3*	*1.0*	*0.2*	*-0.2*	*-0.1*
	L0L1-Ca	*4.8*	*3.0*	*1.8*	*0.9*	*0.3*	*0.1*	*0.3*
	L1L2-Ca	*5.9*	*3.4*	*1.6*	*0.5*	*-0.2*	*-0.4*	*0.0*
	L2L3-Ca	*3.2*	*8.3*	*5.8*	*3.6*	*2.1*	*1.0*	*0.5*
	L0L1-Cb	*4.3*	*3.8*	*2.4*	*1.5*	*0.9*	*0.5*	*0.3*
	L2L3-Cb	*2.6*	*5.3*	*4.4*	*2.8*	*1.6*	*0.8*	*0.2*
	L0U1-Aa	*-5.9*	*-5.2*	*-4.2*	*-3.3*	*-2.4*	*-1.3*	*-0.3*
	L0U1-Ab	*-7.1*	*-6.5*	*-5.2*	*-4.2*	*-3.1*	*-1.8*	*-0.6*
	U2U3-Aa	*-3.8*	*-7.8*	*-10.1*	*-8.2*	*-6.0*	*-3.7*	*-1.4*
	U2U3-Ab	*-1.8*	*-3.9*	*-5.4*	*-4.3*	*-3.0*	*-2.0*	*-0.7*
	L1U1-D	*23.4*	*0.3*	*-1.2*	*-1.0*	*-1.1*	*-1.0*	*-1.1*
	L2U2-D	*8.9*	*10.2*	*-7.2*	*-7.0*	*-5.1*	*-3.3*	*-1.5*
	U1L2-E	*-4.7*	*15.9*	*14.1*	*11.1*	*8.3*	*5.4*	*2.5*

Table E.2. Measured strain for the 20 km/hr northbound controlled loading scenarios.

		microstrain (με)						
Trial	Member	1	2	3	4	5	6	7
Northbound 20 km/hr T1	LOL1-B	6.2	5.5	3.5	2.3	1.4	0.9	0.9
	L0L1-Ca	4.8	4.0	2.4	1.6	0.9	0.5	0.7
	L1L2-Ca	5.8	4.9	2.6	1.4	0.7	0.3	0.5
	L2L3-Ca	2.9	7.6	6.5	4.4	2.8	1.7	1.2
	L0L1-Cb	4.0	4.4	2.9	2.1	1.5	1.2	1.1
	L2L3-Cb	2.1	5.6	5.1	3.4	2.2	1.2	0.6
	L0U1-Aa	-5.0	-5.3	-4.3	-3.6	-2.7	-1.7	-0.7
	L0U1-Ab	-6.4	-6.8	-5.7	-4.7	-3.7	-2.5	-1.3
	U2U3-Aa	-3.1	-6.8	-9.8	-8.6	-6.5	-4.3	-2.2
	U2U3-Ab	-1.6	-4.1	-6.0	-5.3	-3.7	-2.4	-1.3
	L1U1-D	21.4	4.7	-0.5	-0.1	0.0	0.2	0.2
	L2U2-D	6.5	10.6	-4.8	-6.9	-5.0	-3.3	-1.4
	U1L2-E	-5.7	11.6	13.5	11.1	8.5	5.7	3.0
Northbound 20 km/hr T2	LOL1-B	6.3	6.0	3.7	2.5	1.7	1.2	1.2
	L0L1-Ca	4.7	4.4	2.6	1.9	1.3	0.9	1.1
	L1L2-Ca	5.8	5.5	2.8	1.6	0.8	0.4	0.7
	L2L3-Ca	2.6	7.8	6.8	4.1	2.5	1.2	0.7
	L0L1-Cb	4.6	4.9	3.5	2.4	1.8	1.5	1.5
	L2L3-Cb	2.5	5.5	5.1	3.6	2.2	1.1	0.6
	L0U1-Aa	-4.8	-5.7	-4.8	-3.6	-2.5	-1.5	-0.7
	L0U1-Ab	-5.5	-6.9	-5.6	-4.4	-3.2	-2.0	-0.9
	U2U3-Aa	-2.9	-7.1	-10.3	-8.9	-6.3	-4.3	-2.2
	U2U3-Ab	-1.8	-4.0	-5.7	-5.2	-3.7	-2.3	-1.1

	L1U1-D	20.5	6.4	-0.3	0.1	0.2	0.2	0.3
	L2U2-D	5.6	11.6	-4.5	-7.0	-4.7	-3.2	-1.4
	U1L2-E	-6.0	11.2	14.1	10.9	7.7	5.2	2.6
Northbound 20 km/hr T3	LOL1-B	7.4	5.3	3.5	2.2	1.4	1.0	1.2
	L0L1-Ca	5.5	3.8	2.5	1.5	1.0	0.7	0.8
	L1L2-Ca	6.9	4.3	2.5	1.3	0.6	0.4	0.7
	L2L3-Ca	3.9	8.6	6.3	3.8	2.4	1.6	1.0
	L0L1-Cb	5.1	4.3	3.0	2.3	1.7	1.4	1.2
	L2L3-Cb	3.0	5.6	4.5	3.0	2.0	1.2	0.6
	L0U1-Aa	-6.1	-5.7	-4.7	-3.7	-2.8	-1.8	-0.8
	L0U1-Ab	-7.6	-7.1	-5.8	-4.4	-3.3	-2.2	-0.9
	U2U3-Aa	-4.3	-8.3	-10.9	-8.5	-6.5	-4.4	-2.0
	U2U3-Ab	-2.2	-4.2	-5.5	-4.4	-3.5	-2.4	-1.1
	L1U1-D	23.0	1.4	-0.3	0.0	0.0	0.1	0.0
	L2U2-D	8.2	9.9	-7.7	-6.8	-4.9	-3.1	-1.4
	U1L2-E	-4.4	15.4	13.9	10.4	8.0	5.2	2.5
Averaged Northbound 20 km/hr	*LOL1-B*	*6.6*	*5.6*	*3.6*	*2.4*	*1.5*	*1.0*	*1.1*
	L0L1-Ca	*5.0*	*4.1*	*2.5*	*1.6*	*1.1*	*0.7*	*0.8*
	L1L2-Ca	*6.2*	*4.9*	*2.6*	*1.4*	*0.7*	*0.4*	*0.6*
	L2L3-Ca	*3.2*	*8.0*	*6.5*	*4.1*	*2.6*	*1.5*	*1.0*
	L0L1-Cb	*4.6*	*4.6*	*3.1*	*2.3*	*1.7*	*1.4*	*1.3*
	L2L3-Cb	*2.5*	*5.6*	*4.9*	*3.3*	*2.1*	*1.2*	*0.6*
	L0U1-Aa	*-5.3*	*-5.6*	*-4.6*	*-3.7*	*-2.7*	*-1.7*	*-0.7*
	L0U1-Ab	*-6.5*	*-7.0*	*-5.7*	*-4.5*	*-3.4*	*-2.2*	*-1.0*
	U2U3-Aa	*-3.4*	*-7.4*	*-10.3*	*-8.7*	*-6.4*	*-4.3*	*-2.2*
	U2U3-Ab	*-1.9*	*-4.1*	*-5.7*	*-5.0*	*-3.6*	*-2.4*	*-1.2*
	L1U1-D	*21.6*	*4.2*	*-0.4*	*0.0*	*0.1*	*0.2*	*0.1*
	L2U2-D	*6.8*	*10.7*	*-5.7*	*-6.9*	*-4.9*	*-3.2*	*-1.4*
	U1L2-E	*-5.4*	*12.7*	*13.8*	*10.8*	*8.1*	*5.4*	*2.7*

Table E.3. Measured strain for the 30 km/hr northbound controlled loading scenarios.

		microstrain (με)						
Trial	Member	1	2	3	4	5	6	7
Northbound 30 km/hr T1	LOL1-B	5.4	5.8	3.3	1.9	1.1	0.4	0.5
	L0L1-Ca	4.0	4.2	2.4	1.4	0.8	0.4	0.5
	L1L2-Ca	4.9	5.3	2.5	1.2	0.6	0.1	0.4
	L2L3-Ca	2.0	7.2	6.6	4.0	2.4	1.2	0.6
	L0L1-Cb	3.9	4.7	3.1	2.3	1.6	1.3	1.0
	L2L3-Cb	2.0	5.5	5.0	3.3	2.0	0.9	0.4
	L0U1-Aa	-4.0	-5.6	-4.4	-3.6	-2.7	-1.9	-0.8
	L0U1-Ab	-4.9	-7.1	-5.8	-4.6	-3.6	-2.5	-1.2
	U2U3-Aa	-2.5	-6.6	-10.1	-8.8	-6.5	-4.5	-2.0
	U2U3-Ab	-1.7	-4.0	-5.7	-4.9	-3.7	-2.4	-1.1
	L1U1-D	18.5	7.9	-0.5	-0.1	0.1	0.1	0.2
	L2U2-D	4.8	11.6	-4.0	-7.3	-5.1	-3.4	-1.6
	U1L2-E	-5.6	10.0	14.2	11.0	8.2	5.5	2.5
Northbound 30 km/hr T2	LOL1-B	6.6	5.7	3.5	2.3	1.5	0.8	1.1
	L0L1-Ca	4.9	4.0	2.5	1.6	1.1	0.5	0.6
	L1L2-Ca	6.0	5.0	2.5	1.3	0.7	0.3	0.5
	L2L3-Ca	2.8	8.2	6.6	3.8	2.3	1.5	0.8
	L0L1-Cb	4.6	4.6	3.2	2.0	1.3	1.3	1.1
	L2L3-Cb	2.6	5.7	5.2	3.7	2.5	1.6	1.1
	L0U1-Aa	-5.2	-5.9	-4.8	-3.7	-2.7	-2.0	-0.8
	L0U1-Ab	-6.4	-7.3	-6.0	-4.7	-3.5	-2.5	-1.2
	U2U3-Aa	-3.3	-7.5	-10.6	-8.5	-6.3	-4.5	-1.9
	U2U3-Ab	-2.0	-4.3	-5.9	-5.1	-3.9	-2.6	-1.3
	L1U1-D	21.3	4.2	-0.4	-0.1	-0.1	-0.1	-0.2
	L2U2-D	6.3	11.0	-6.1	-7.0	-5.0	-3.4	-1.5
	U1L2-E	-5.9	12.8	14.1	10.5	7.6	5.0	1.7
Northbound 30 km/hr T3	LOL1-B	6.3	6.2	3.8	2.5	1.7	1.1	1.1
	L0L1-Ca	4.6	4.4	2.5	1.5	1.0	0.6	0.6
	L1L2-Ca	5.8	5.8	2.9	1.7	1.0	0.5	0.6
	L2L3-Ca	2.6	7.8	7.1	4.3	2.7	1.4	0.8
	L0L1-Cb	4.2	4.9	3.3	2.5	1.9	1.4	1.5
	L2L3-Cb	2.1	5.2	4.9	3.6	2.5	1.6	1.0
	L0U1-Aa	-4.7	-6.0	-4.5	-3.5	-2.7	-1.7	-0.9
	L0U1-Ab	-6.0	-7.7	-6.1	-4.9	-3.7	-2.4	-1.5
	U2U3-Aa	-2.9	-7.1	-10.3	-9.3	-6.9	-4.6	-2.6
	U2U3-Ab	-1.7	-3.7	-5.2	-5.0	-3.9	-2.7	-1.6
	L1U1-D	21.1	7.9	-0.3	0.2	0.2	0.3	0.3
	L2U2-D	5.7	12.3	-3.2	-7.4	-5.2	-3.4	-1.8
	U1L2-E	-6.4	10.8	14.7	11.5	8.6	5.7	3.2
Northbound 30 km/hr T4	LOL1-B	6.4	5.6	3.5	2.2	1.3	0.6	0.7
	L0L1-Ca	4.7	4.1	2.6	1.5	0.9	0.4	0.5
	L1L2-Ca	6.0	5.2	2.8	1.5	0.8	0.3	0.5
	L2L3-Ca	2.9	7.9	7.0	4.0	2.6	1.4	0.8
	L0L1-Cb	4.2	4.4	3.1	2.1	1.4	1.2	0.8
	L2L3-Cb	2.2	5.2	4.9	3.3	2.0	1.1	0.6

	L0U1-Aa	-5.1	-5.8	-4.8	-3.7	-2.9	-2.0	-1.0
	L0U1-Ab	-6.4	-7.3	-6.1	-4.5	-3.5	-2.5	-1.4
	U2U3-Aa	-3.2	-7.2	-10.5	-8.9	-6.7	-4.7	-2.5
	U2U3-Ab	-1.6	-3.8	-5.4	-4.7	-3.6	-2.4	-1.4
	L1U1-D	21.9	5.6	-0.4	0.1	0.1	0.1	0.2
	L2U2-D	6.5	11.5	-4.7	-7.4	-5.3	-3.6	-2.0
	U1L2-E	-6.2	11.8	14.4	10.9	8.2	5.5	2.9
Northbound 30 km/hr T5	LOL1-B	5.4	5.9	3.4	2.2	1.2	0.6	1.1
	L0L1-Ca	4.0	4.3	2.4	1.4	0.8	0.3	0.8
	L1L2-Ca	4.9	5.4	2.6	1.3	0.6	0.2	0.8
	L2L3-Ca	2.3	7.1	6.8	3.9	2.5	1.4	0.8
	L0L1-Cb	4.1	4.9	3.2	2.1	1.6	1.4	1.0
	L2L3-Cb	1.9	5.3	5.0	3.4	2.0	1.0	0.5
	L0U1-Aa	-4.3	-5.8	-4.6	-3.6	-2.8	-1.9	-0.7
	L0U1-Ab	-5.1	-7.2	-5.8	-4.6	-3.5	-2.3	-0.8
	U2U3-Aa	-2.5	-6.6	-9.7	-8.6	-6.3	-4.3	-1.6
	U2U3-Ab	-1.5	-3.7	-5.6	-5.0	-3.8	-2.4	-0.8
	L1U1-D	18.5	8.8	-0.3	0.1	0.2	0.1	0.0
	L2U2-D	4.8	11.4	-2.9	-7.1	-4.8	-3.1	-1.2
	U1L2-E	-5.6	8.8	13.9	10.6	7.8	5.1	1.8
Averaged Northbound 30 km/hr	*LOL1-B*	*6.0*	*5.8*	*3.5*	*2.2*	*1.4*	*0.7*	*0.9*
	L0L1-Ca	*4.4*	*4.2*	*2.5*	*1.5*	*0.9*	*0.4*	*0.6*
	L1L2-Ca	*5.5*	*5.4*	*2.6*	*1.4*	*0.7*	*0.3*	*0.6*
	L2L3-Ca	*2.5*	*7.6*	*6.8*	*4.0*	*2.5*	*1.4*	*0.8*
	L0L1-Cb	*4.2*	*4.7*	*3.2*	*2.2*	*1.6*	*1.3*	*1.1*
	L2L3-Cb	*2.2*	*5.4*	*5.0*	*3.5*	*2.2*	*1.2*	*0.7*
	L0U1-Aa	*-4.6*	*-5.8*	*-4.6*	*-3.6*	*-2.8*	*-1.9*	*-0.8*
	L0U1-Ab	*-5.8*	*-7.3*	*-6.0*	*-4.7*	*-3.5*	*-2.4*	*-1.2*
	U2U3-Aa	*-2.9*	*-7.0*	*-10.2*	*-8.8*	*-6.6*	*-4.5*	*-2.1*
	U2U3-Ab	*-1.7*	*-3.9*	*-5.5*	*-4.9*	*-3.8*	*-2.5*	*-1.2*
	L1U1-D	*20.3*	*6.9*	*-0.4*	*0.0*	*0.1*	*0.1*	*0.1*
	L2U2-D	*5.6*	*11.6*	*-4.2*	*-7.3*	*-5.1*	*-3.4*	*-1.6*
	U1L2-E	*-5.9*	*10.8*	*14.3*	*10.9*	*8.1*	*5.4*	*2.4*

Table E.4. Measured strain for the 50 km/hr northbound controlled loading scenarios.

		microstrain (με)						
Trial	Member	1	2	3	4	5	6	7
Northbound 50 km/hr T1	LOL1-B	5.4	5.7	3.6	2.1	1.5	1.0	1.0
	L0L1-Ca	4.1	4.1	2.5	1.4	1.0	0.7	0.8
	L1L2-Ca	5.1	5.2	2.7	1.6	0.8	0.5	0.7
	L2L3-Ca	2.1	6.8	6.4	4.2	2.5	1.2	0.8
	L0L1-Cb	4.5	5.0	3.2	2.4	1.5	1.2	1.1
	L2L3-Cb	2.0	5.7	5.3	3.2	2.2	1.2	0.8
	L0U1-Aa	-4.1	-5.3	-4.2	-3.6	-2.8	-1.8	-1.1
	L0U1-Ab	-5.0	-6.6	-5.4	-4.5	-3.4	-2.2	-1.2
	U2U3-Aa	-2.6	-6.3	-9.5	-8.6	-6.6	-4.3	-2.5
	U2U3-Ab	-1.8	-4.3	-6.1	-5.3	-4.1	-2.6	-1.6
	L1U1-D	18.0	7.4	-0.5	0.1	0.1	0.1	0.1
	L2U2-D	4.9	10.3	-3.2	-7.1	-5.1	-3.1	-1.8
	U1L2-E	-5.5	8.7	13.2	10.3	7.7	4.9	2.7
Northbound 50 km/hr T2	LOL1-B	6.1	4.8	2.8	1.9	1.5	0.5	1.1
	L0L1-Ca	4.6	3.4	1.9	1.2	1.0	0.3	0.7
	L1L2-Ca	5.8	4.0	2.1	1.1	0.6	0.0	0.4
	L2L3-Ca	3.5	7.6	5.9	3.6	2.1	0.8	0.6
	L0L1-Cb	4.9	4.0	2.8	2.0	1.0	0.8	0.9
	L2L3-Cb	3.0	6.0	4.5	3.3	2.3	0.9	0.9
	L0U1-Aa	-5.0	-4.9	-4.2	-3.3	-2.5	-1.4	-0.8
	L0U1-Ab	-6.3	-6.2	-5.3	-4.4	-3.3	-2.0	-1.1
	U2U3-Aa	-3.6	-7.3	-9.8	-8.2	-6.1	-3.8	-2.1
	U2U3-Ab	-2.4	-4.7	-5.7	-5.1	-4.0	-2.2	-1.4
	L1U1-D	19.6	2.2	-0.1	0.2	0.3	0.1	0.2
	L2U2-D	7.2	9.0	-6.3	-6.5	-4.6	-2.9	-1.3
	U1L2-E	-4.0	12.7	12.4	9.7	7.1	4.2	2.2
Average Northbound 50 km/hr	*LOL1-B*	*5.8*	*5.3*	*3.2*	*2.0*	*1.5*	*0.8*	*1.0*
	L0L1-Ca	*4.3*	*3.7*	*2.2*	*1.3*	*1.0*	*0.5*	*0.7*
	L1L2-Ca	*5.5*	*4.6*	*2.4*	*1.4*	*0.7*	*0.2*	*0.5*
	L2L3-Ca	*2.8*	*7.2*	*6.2*	*3.9*	*2.3*	*1.0*	*0.7*
	L0L1-Cb	*4.7*	*4.5*	*3.0*	*2.2*	*1.3*	*1.0*	*1.0*
	L2L3-Cb	*2.5*	*5.9*	*4.9*	*3.3*	*2.3*	*1.1*	*0.8*
	L0U1-Aa	*-4.5*	*-5.1*	*-4.2*	*-3.5*	*-2.6*	*-1.6*	*-0.9*
	L0U1-Ab	*-5.7*	*-6.4*	*-5.4*	*-4.5*	*-3.3*	*-2.1*	*-1.1*
	U2U3-Aa	*-3.1*	*-6.8*	*-9.6*	*-8.4*	*-6.3*	*-4.0*	*-2.3*
	U2U3-Ab	*-2.1*	*-4.5*	*-5.9*	*-5.2*	*-4.0*	*-2.4*	*-1.5*
	L1U1-D	*18.8*	*4.8*	*-0.3*	*0.2*	*0.2*	*0.1*	*0.1*
	L2U2-D	*6.1*	*9.7*	*-4.8*	*-6.8*	*-4.9*	*-3.0*	*-1.5*
	U1L2-E	*-4.8*	*10.7*	*12.8*	*10.0*	*7.4*	*4.5*	*2.5*

Table E.5. Static strain values for the southbound static controlled loading scenario.

		microstrain (με)						
Trial	Member	7	6	5	4	3	2	1
Static Southbound T1	LOL1-B	-0.5	0.0	1.2	2.0	3.5	3.2	0.4
	L0L1-Ca	-0.7	-0.4	0.5	1.1	2.4	2.5	0.5
	L1L2-Ca	-0.4	0.1	1.1	2.0	3.8	4.0	0.5
	L2L3-Ca	0.5	1.5	2.8	4.0	4.5	1.8	-0.1
	L0L1-Cb	0.3	0.8	1.9	3.3	6.1	6.5	0.6
	L2L3-Cb	1.0	2.1	4.8	7.8	8.8	2.3	0.0
	L0U1-Aa	-0.6	-1.0	-1.7	-2.2	-2.7	-2.2	0.2
	L0U1-Ab	-0.8	-1.2	-2.2	-2.3	-3.1	-2.6	0.2
	U2U3-Aa	-2.1	-3.2	-5.0	-5.1	-3.2	-1.2	0.5
	U2U3-Ab	-5.2	-7.0	-9.7	-11.0	-6.8	-2.4	0.6
	L1U1-D	0.9	0.8	0.2	0.0	3.0	9.3	0.0
	L2U2-D	-0.6	-1.6	-2.9	-1.4	5.2	3.0	0.1
	U1L2-E	3.1	4.1	5.5	6.4	4.5	-3.0	-0.7
Static Southbound T2	LOL1-B	0.4	0.8	1.4	2.1	3.3	3.0	0.0
	L0L1-Ca	0.4	0.6	0.9	1.5	2.3	2.2	0.0
	L1L2-Ca	0.2	0.6	1.2	2.0	3.4	3.4	0.0
	L2L3-Ca	0.8	1.6	2.6	3.8	4.2	1.6	-0.1
	L0L1-Cb	-0.1	0.4	1.3	2.7	5.1	6.0	0.1
	L2L3-Cb	0.8	2.2	4.3	7.2	8.7	2.0	-0.2
	L0U1-Aa	-1.3	-1.6	-1.8	-2.1	-2.6	-2.0	0.1
	L0U1-Ab	-1.2	-1.7	-2.2	-2.6	-3.1	-2.4	0.1
	U2U3-Aa	-2.6	-3.8	-4.7	-4.9	-3.2	-1.2	0.3
	U2U3-Ab	-5.4	-7.4	-9.7	-11.0	-7.1	-2.5	0.6
	L1U1-D	-0.2	-0.2	-0.2	-0.3	2.7	8.2	-0.1
	L2U2-D	-2.3	-3.0	-3.6	-1.8	4.6	2.5	0.1
	U1L2-E	2.4	3.7	4.9	6.2	4.4	-2.7	-0.2
Static Southbound T3	LOL1-B	-0.1	0.7	1.1	2.3	3.6	3.3	-0.1
	L0L1-Ca	0.6	0.9	1.2	1.9	2.8	2.6	-0.1
	L1L2-Ca	-0.1	0.5	1.1	2.0	3.5	3.6	-0.1
	L2L3-Ca	0.7	1.7	2.7	3.9	4.4	1.8	-0.1
	L0L1-Cb	-0.4	0.3	1.1	2.6	4.7	5.7	0.0
	L2L3-Cb	1.1	2.8	4.4	7.8	9.1	2.5	-0.3
	L0U1-Aa	-1.2	-1.3	-1.7	-2.0	-2.4	-2.1	0.1
	L0U1-Ab	-0.5	-1.2	-1.7	-2.3	-2.8	-2.4	0.1
	U2U3-Aa	-2.3	-3.6	-4.6	-4.9	-3.4	-1.3	0.2
	U2U3-Ab	-5.2	-7.6	-9.3	-10.5	-6.8	-2.7	0.5
	L1U1-D	-0.1	0.0	0.0	0.0	3.1	9.9	0.0
	L2U2-D	-1.8	-2.6	-3.3	-1.3	5.5	3.2	0.1
	U1L2-E	2.1	3.5	4.9	6.3	4.9	-2.9	-0.3
Averaged Static Southbound	*LOL1-B*	*-0.1*	*0.5*	*1.2*	*2.2*	*3.5*	*3.2*	*0.1*
	L0L1-Ca	*0.1*	*0.4*	*0.9*	*1.5*	*2.5*	*2.4*	*0.1*
	L1L2-Ca	*-0.1*	*0.4*	*1.1*	*2.0*	*3.5*	*3.7*	*0.1*
	L2L3-Ca	*0.7*	*1.6*	*2.7*	*3.9*	*4.4*	*1.7*	*-0.1*
	L0L1-Cb	*-0.1*	*0.5*	*1.4*	*2.9*	*5.3*	*6.1*	*0.2*
	L2L3-Cb	*1.0*	*2.4*	*4.5*	*7.6*	*8.8*	*2.3*	*-0.2*

	L0U1-Aa	*-1.1*	*-1.3*	*-1.7*	*-2.1*	*-2.6*	*-2.1*	*0.1*
	L0U1-Ab	*-0.9*	*-1.4*	*-2.0*	*-2.4*	*-3.0*	*-2.4*	*0.1*
	U2U3-Aa	*-2.3*	*-3.5*	*-4.7*	*-5.0*	*-3.3*	*-1.2*	*0.3*
	U2U3-Ab	*-5.3*	*-7.3*	*-9.6*	*-10.8*	*-6.9*	*-2.5*	*0.5*
	L1U1-D	*0.2*	*0.2*	*0.0*	*-0.1*	*2.9*	*9.1*	*0.0*
	L2U2-D	*-1.6*	*-2.4*	*-3.3*	*-1.5*	*5.1*	*2.9*	*0.1*
	U1L2-E	*2.5*	*3.8*	*5.1*	*6.3*	*4.6*	*-2.9*	*-0.4*

Table E.6. Measured strain for the 20 km/hr southbound controlled loading scenarios.

		microstrain (με)						
Trial	Member	7	6	5	4	3	2	1
Southbound 20 km/hr T1	LOL1-B	0.3	0.3	0.6	1.3	2.3	3.3	3.4
	L0L1-Ca	0.2	0.1	0.3	0.7	1.5	2.3	2.5
	L1L2-Ca	-0.1	0.1	0.6	1.1	2.1	3.4	4.0
	L2L3-Ca	0.2	0.8	2.1	3.3	4.6	4.6	2.4
	L0L1-Cb	-0.6	-0.2	0.7	1.8	3.2	5.3	6.6
	L2L3-Cb	0.3	1.0	2.4	4.4	7.2	8.7	2.6
	L0U1-Aa	-0.5	-0.9	-1.3	-1.7	-2.2	-2.4	-2.2
	L0U1-Ab	-0.6	-1.2	-1.7	-2.1	-2.9	-3.2	-3.1
	U2U3-Aa	-1.3	-2.5	-3.8	-5.0	-5.4	-3.6	-1.6
	U2U3-Ab	-2.3	-4.6	-7.0	-9.0	-10.1	-7.0	-2.9
	L1U1-D	0.0	0.0	0.0	-0.2	-0.3	2.6	9.5
	L2U2-D	-1.2	-2.1	-2.9	-3.8	-1.6	4.5	3.1
	U1L2-E	1.5	3.1	4.5	5.9	7.3	5.2	-2.1
Southbound 20 km/hr T2	LOL1-B	0.6	1.0	1.2	1.9	2.7	3.7	2.6
	L0L1-Ca	0.4	0.6	0.6	1.1	1.7	2.5	1.9
	L1L2-Ca	0.2	0.3	0.6	1.4	2.5	3.9	2.8
	L2L3-Ca	0.5	0.9	1.8	3.1	4.7	4.2	1.6
	L0L1-Cb	-0.2	-0.5	0.3	1.6	3.7	6.6	5.6
	L2L3-Cb	0.1	0.8	2.4	4.8	8.4	6.9	1.7
	L0U1-Aa	-0.3	-0.6	-1.1	-1.5	-2.0	-2.2	-1.2
	L0U1-Ab	-0.5	-1.0	-1.5	-1.9	-2.6	-3.1	-1.8
	U2U3-Aa	-1.0	-2.2	-3.5	-4.7	-4.8	-2.9	-1.1
	U2U3-Ab	-2.0	-4.3	-6.6	-9.3	-9.9	-5.7	-1.9
	L1U1-D	-0.1	-0.1	-0.1	-0.2	0.2	5.5	6.8
	L2U2-D	-0.6	-1.4	-2.4	-3.1	0.2	4.6	2.1
	U1L2-E	1.1	2.8	4.2	5.6	7.0	2.7	-1.5
Southbound 20 km/hr T3	LOL1-B	-0.1	0.1	0.7	1.3	2.1	3.5	3.9
	L0L1-Ca	-0.1	0.0	0.5	0.8	1.5	2.3	2.8
	L1L2-Ca	0.1	0.0	0.6	1.2	2.0	3.5	4.2
	L2L3-Ca	0.6	0.7	1.6	2.5	4.0	4.8	2.6
	L0L1-Cb	0.6	0.3	0.9	1.8	3.2	5.3	7.5
	L2L3-Cb	0.4	1.0	2.5	4.4	7.2	10.1	4.8
	L0U1-Aa	-0.3	-0.5	-1.0	-1.2	-1.7	-2.2	-2.0
	L0U1-Ab	-0.3	-0.8	-1.3	-1.6	-2.3	-2.9	-2.6
	U2U3-Aa	-0.7	-1.8	-3.0	-4.2	-5.0	-4.0	-1.8
	U2U3-Ab	-1.8	-4.0	-6.4	-8.6	-10.9	-8.0	-4.3
	L1U1-D	0.2	0.2	0.1	0.0	-0.1	2.0	8.7

	L2U2-D	-0.4	-1.3	-2.1	-3.1	-2.6	4.0	3.4
	U1L2-E	1.0	2.2	3.5	4.7	6.3	6.0	-1.2
Averaged Southbound 20 km/hr	*LOL1-B*	*0.3*	*0.5*	*0.8*	*1.5*	*2.4*	*3.5*	*3.3*
	L0L1-Ca	*0.1*	*0.2*	*0.5*	*0.9*	*1.5*	*2.4*	*2.4*
	L1L2-Ca	*0.1*	*0.1*	*0.6*	*1.2*	*2.2*	*3.6*	*3.6*
	L2L3-Ca	*0.4*	*0.8*	*1.8*	*3.0*	*4.4*	*4.5*	*2.2*
	L0L1-Cb	*0.0*	*-0.1*	*0.6*	*1.8*	*3.4*	*5.8*	*6.6*
	L2L3-Cb	*0.3*	*0.9*	*2.4*	*4.5*	*7.6*	*8.6*	*3.0*
	L0U1-Aa	*-0.4*	*-0.7*	*-1.1*	*-1.5*	*-2.0*	*-2.2*	*-1.8*
	L0U1-Ab	*-0.5*	*-1.0*	*-1.5*	*-1.9*	*-2.6*	*-3.1*	*-2.5*
	U2U3-Aa	*-1.0*	*-2.1*	*-3.4*	*-4.6*	*-5.1*	*-3.5*	*-1.5*
	U2U3-Ab	*-2.0*	*-4.3*	*-6.7*	*-9.0*	*-10.3*	*-6.9*	*-3.1*
	L1U1-D	*0.1*	*0.0*	*0.0*	*-0.1*	*-0.1*	*3.3*	*8.3*
	L2U2-D	*-0.7*	*-1.6*	*-2.5*	*-3.3*	*-1.4*	*4.4*	*2.9*
	U1L2-E	*1.2*	*2.7*	*4.1*	*5.4*	*6.9*	*4.6*	*-1.6*

Table E.7. Measured strain for the 30 km/hr southbound controlled loading scenarios.

		microstrain (με)						
Trial	Member	7	6	5	4	3	2	1
Southbound 30 km/hr T1	LOL1-B	0.4	0.6	0.8	1.2	1.9	3.0	3.8
	L0L1-Ca	0.3	0.5	0.5	0.9	1.4	2.2	2.9
	L1L2-Ca	0.3	0.3	0.6	1.2	1.8	3.1	4.4
	L2L3-Ca	0.4	0.7	1.3	2.4	3.5	4.4	3.1
	L0L1-Cb	-0.3	-0.5	0.0	1.0	2.3	4.5	7.2
	L2L3-Cb	0.3	0.9	2.0	3.9	6.2	9.8	5.3
	L0U1-Aa	-0.5	-0.8	-1.1	-1.5	-1.7	-2.1	-2.3
	L0U1-Ab	-0.4	-0.6	-1.2	-1.7	-1.9	-2.5	-3.0
	U2U3-Aa	-0.8	-2.0	-3.1	-4.3	-4.7	-3.8	-2.3
	U2U3-Ab	-1.7	-4.0	-6.0	-8.4	-10.5	-8.6	-4.6
	L1U1-D	-0.3	-0.3	-0.3	-0.5	-0.8	0.6	7.5
	L2U2-D	-0.7	-1.4	-2.3	-3.2	-3.1	2.6	3.6
	U1L2-E	0.6	1.7	3.1	4.4	5.4	5.6	-0.8
Southbound 30 km/hr T2	LOL1-B	0.4	0.6	0.9	1.3	2.2	3.3	3.7
	L0L1-Ca	0.3	0.3	0.5	0.7	1.4	2.3	2.6
	L1L2-Ca	0.3	0.3	0.6	1.1	1.9	3.2	4.0
	L2L3-Ca	0.4	0.6	1.4	2.6	3.8	4.2	2.4
	L0L1-Cb	0.2	-0.3	0.1	1.4	2.6	4.8	7.2
	L2L3-Cb	0.4	0.7	2.0	4.1	6.8	9.7	3.9
	L0U1-Aa	-0.1	-0.5	-0.9	-1.3	-1.8	-2.0	-1.8
	L0U1-Ab	-0.2	-0.7	-1.1	-1.8	-2.1	-2.4	-2.3
	U2U3-Aa	-0.7	-1.8	-2.9	-4.4	-5.1	-3.6	-1.7
	U2U3-Ab	-1.6	-4.1	-6.3	-8.8	-11.1	-7.9	-3.8
	L1U1-D	-0.1	-0.1	-0.1	-0.2	-0.3	1.3	7.6
	L2U2-D	-0.7	-1.5	-2.3	-3.5	-3.0	3.0	2.6
	U1L2-E	0.7	1.9	3.2	5.0	6.4	5.3	-1.3
km/hr T3	LOL1-B	0.5	0.7	0.7	1.4	2.0	3.3	3.8
	L0L1-Ca	0.4	0.5	0.4	1.0	1.4	2.3	2.8

	L1L2-Ca	0.3	0.3	0.4	1.0	1.8	3.2	4.1
	L2L3-Ca	0.5	0.8	1.5	2.5	3.9	4.7	2.8
	L0L1-Cb	0.0	-0.3	0.1	1.1	2.5	4.6	6.9
	L2L3-Cb	0.2	0.7	1.9	4.1	6.3	9.2	4.5
	L0U1-Aa	-0.4	-0.7	-1.1	-1.4	-1.9	-2.4	-2.4
	L0U1-Ab	-0.4	-0.9	-1.5	-2.0	-2.5	-3.0	-3.2
	U2U3-Aa	-0.7	-1.8	-3.0	-4.3	-5.0	-3.8	-2.0
	U2U3-Ab	-1.7	-4.0	-6.2	-8.7	-10.4	-8.1	-4.4
	L1U1-D	0.2	0.1	0.1	0.1	-0.1	1.6	8.6
	L2U2-D	-0.5	-1.3	-2.1	-3.1	-2.5	3.7	3.9
	U1L2-E	0.7	1.9	3.3	4.8	6.5	5.9	-0.9
Southbound 30 km/hr T4	LOL1-B	0.1	0.2	0.5	1.0	2.2	3.1	3.6
	L0L1-Ca	0.0	-0.1	0.2	0.5	1.4	2.1	2.6
	L1L2-Ca	-0.2	-0.2	0.2	0.8	1.7	3.0	4.0
	L2L3-Ca	0.1	0.6	1.5	2.5	3.7	4.3	2.5
	L0L1-Cb	-0.6	-0.5	0.1	1.2	2.6	4.7	6.9
	L2L3-Cb	0.0	0.6	2.0	3.8	7.0	9.2	3.9
	L0U1-Aa	-0.4	-0.7	-1.1	-1.4	-1.7	-2.1	-2.3
	L0U1-Ab	-0.7	-1.3	-1.6	-2.1	-2.6	-2.9	-3.1
	U2U3-Aa	-1.1	-2.3	-3.5	-4.6	-5.5	-3.8	-2.0
	U2U3-Ab	-2.2	-4.4	-6.7	-8.7	-11.3	-7.9	-4.3
	L1U1-D	0.0	0.1	-0.1	-0.1	-0.2	1.7	9.5
	L2U2-D	-0.8	-1.7	-2.5	-3.4	-2.5	4.1	3.7
	U1L2-E	1.3	2.7	4.0	5.3	6.9	5.8	-1.4
Southbound 30 km/hr T5	LOL1-B	0.6	0.6	1.0	1.9	2.7	3.8	3.5
	L0L1-Ca	0.3	0.4	0.5	1.2	2.0	2.7	2.7
	L1L2-Ca	0.3	0.3	0.7	1.5	2.5	3.8	3.8
	L2L3-Ca	0.5	1.2	2.0	3.3	4.3	4.3	1.9
	L0L1-Cb	-0.2	0.1	0.9	1.9	3.6	6.0	6.4
	L2L3-Cb	0.5	1.2	2.8	5.1	8.3	8.4	2.8
	L0U1-Aa	-0.6	-1.0	-1.3	-1.7	-2.0	-2.3	-1.8
	L0U1-Ab	-0.5	-1.1	-1.6	-2.1	-2.7	-3.0	-2.5
	U2U3-Aa	-1.3	-2.6	-3.7	-5.0	-5.0	-3.1	-1.5
	U2U3-Ab	-2.5	-4.9	-7.1	-9.7	-10.4	-6.5	-2.8
	L1U1-D	-0.1	-0.1	-0.2	-0.3	-0.3	3.6	8.4
	L2U2-D	-1.0	-2.0	-2.9	-3.6	-1.0	4.5	2.4
	U1L2-E	1.2	2.8	4.0	5.6	6.8	3.7	-2.3
Averaged Southbound 30 km/hr	*LOL1-B*	*0.4*	*0.5*	*0.8*	*1.4*	*2.2*	*3.3*	*3.7*
	L0L1-Ca	*0.3*	*0.3*	*0.4*	*0.9*	*1.5*	*2.3*	*2.7*
	L1L2-Ca	*0.2*	*0.2*	*0.5*	*1.1*	*2.0*	*3.3*	*4.0*
	L2L3-Ca	*0.4*	*0.8*	*1.5*	*2.7*	*3.8*	*4.4*	*2.5*
	L0L1-Cb	*-0.2*	*-0.3*	*0.3*	*1.3*	*2.7*	*4.9*	*6.9*
	L2L3-Cb	*0.3*	*0.8*	*2.2*	*4.2*	*6.9*	*9.3*	*4.1*
	L0U1-Aa	*-0.4*	*-0.7*	*-1.1*	*-1.5*	*-1.8*	*-2.2*	*-2.1*
	L0U1-Ab	*-0.4*	*-0.9*	*-1.4*	*-1.9*	*-2.4*	*-2.8*	*-2.8*
	U2U3-Aa	*-0.9*	*-2.1*	*-3.3*	*-4.5*	*-5.1*	*-3.6*	*-1.9*
	U2U3-Ab	*-1.9*	*-4.3*	*-6.5*	*-8.9*	*-10.7*	*-7.8*	*-4.0*
	L1U1-D	*-0.1*	*-0.1*	*-0.1*	*-0.2*	*-0.3*	*1.8*	*8.3*

	L2U2-D	*-0.7*	*-1.6*	*-2.4*	*-3.4*	*-2.4*	*3.6*	*3.2*
	U1L2-E	*0.9*	*2.2*	*3.5*	*5.0*	*6.4*	*5.3*	*-1.3*

Table E.8. Measured strain for the 50 km/hr southbound controlled loading scenarios.

		microstrain (με)						
Trial	Member	7	6	5	4	3	2	1
Southbound 50 km/hr T1	LOL1-B	-0.1	0.0	0.8	1.5	2.3	3.5	3.1
	L0L1-Ca	0.0	-0.1	0.5	1.1	1.7	2.6	2.4
	L1L2-Ca	-0.1	-0.1	0.5	1.1	2.0	3.4	3.2
	L2L3-Ca	0.4	0.9	1.7	2.9	4.1	4.2	1.5
	L0L1-Cb	-0.2	-0.2	0.2	1.1	2.8	5.6	5.9
	L2L3-Cb	0.2	0.8	2.4	4.5	7.5	8.9	2.6
	L0U1-Aa	-0.4	-0.7	-1.2	-1.6	-1.9	-2.3	-1.6
	L0U1-Ab	-0.5	-0.9	-1.4	-2.0	-2.3	-2.8	-2.1
	U2U3-Aa	-1.3	-2.4	-3.9	-5.1	-5.1	-3.6	-1.3
	U2U3-Ab	-2.5	-4.6	-6.9	-9.3	-10.6	-7.2	-2.9
	L1U1-D	0.0	-0.2	-0.2	-0.3	-0.3	3.2	8.0
	L2U2-D	-0.9	-1.6	-2.6	-3.5	-1.2	4.7	2.7
	U1L2-E	1.5	2.8	4.4	6.0	6.8	4.5	-2.2
Southbound 50 km/hr T2	LOL1-B	-0.4	0.0	0.4	1.0	1.9	3.1	2.9
	L0L1-Ca	-0.3	0.0	0.2	0.7	1.2	2.1	2.2
	L1L2-Ca	-0.1	0.0	0.3	1.0	1.9	3.3	3.3
	L2L3-Ca	0.4	0.8	1.7	2.8	4.2	4.3	1.7
	L0L1-Cb	-0.3	-0.8	-0.1	0.9	2.7	5.1	6.0
	L2L3-Cb	0.0	0.6	2.1	4.1	7.1	8.8	2.8
	L0U1-Aa	-0.3	-0.7	-1.2	-1.5	-2.0	-2.4	-1.8
	L0U1-Ab	-0.4	-0.9	-1.4	-1.9	-2.3	-2.8	-2.1
	U2U3-Aa	-1.1	-2.3	-3.6	-4.7	-5.1	-3.5	-1.4
	U2U3-Ab	-2.0	-4.5	-6.7	-9.0	-10.6	-7.1	-3.1
	L1U1-D	-0.1	-0.1	-0.2	-0.2	-0.2	2.9	7.8
	L2U2-D	-0.9	-1.7	-2.6	-3.5	-1.7	4.4	2.6
	U1L2-E	1.2	2.4	4.0	5.3	6.7	4.5	-2.0
Southbound 50 km/hr T3	LOL1-B	0.1	-0.3	0.5	1.3	1.8	2.9	3.3
	L0L1-Ca	0.0	-0.4	0.1	0.8	1.1	1.9	2.3
	L1L2-Ca	-0.1	-0.2	0.3	1.1	1.8	3.2	3.6
	L2L3-Ca	0.1	0.7	1.7	2.8	4.0	4.2	1.9
	L0L1-Cb	0.0	0.1	0.5	1.3	3.0	5.2	6.4
	L2L3-Cb	0.0	0.7	2.3	4.4	7.4	8.5	3.1
	L0U1-Aa	-0.3	-0.7	-1.1	-1.5	-1.8	-2.2	-1.8
	L0U1-Ab	-0.4	-0.9	-1.4	-1.8	-2.2	-2.9	-2.5
	U2U3-Aa	-1.2	-2.4	-3.6	-4.8	-4.8	-3.2	-1.5
	U2U3-Ab	-2.5	-4.8	-7.1	-9.4	-10.4	-6.9	-3.5
	L1U1-D	-0.3	-0.3	-0.3	-0.4	-0.4	2.7	8.3
	L2U2-D	-1.0	-1.9	-2.9	-3.6	-1.5	4.3	2.8
	U1L2-E	1.6	3.0	4.3	5.6	6.5	4.6	-1.8
Southbound 50 km/hr	*LOL1-B*	*-0.1*	*-0.1*	*0.6*	*1.3*	*2.0*	*3.2*	*3.1*
	L0L1-Ca	*-0.1*	*-0.2*	*0.3*	*0.9*	*1.3*	*2.2*	*2.3*
	L1L2-Ca	*-0.1*	*-0.1*	*0.4*	*1.0*	*1.9*	*3.3*	*3.4*

	L2L3-Ca	*0.3*	*0.8*	*1.7*	*2.8*	*4.1*	*4.3*	*1.7*
	L0L1-Cb	*-0.2*	*-0.3*	*0.2*	*1.1*	*2.8*	*5.3*	*6.1*
	L2L3-Cb	*0.1*	*0.7*	*2.3*	*4.3*	*7.3*	*8.8*	*2.8*
	L0U1-Aa	*-0.3*	*-0.7*	*-1.2*	*-1.5*	*-1.9*	*-2.3*	*-1.7*
	L0U1-Ab	*-0.5*	*-0.9*	*-1.4*	*-1.9*	*-2.3*	*-2.8*	*-2.2*
	U2U3-Aa	*-1.2*	*-2.4*	*-3.7*	*-4.9*	*-5.0*	*-3.4*	*-1.4*
	U2U3-Ab	*-2.4*	*-4.6*	*-6.9*	*-9.2*	*-10.5*	*-7.1*	*-3.2*
	L1U1-D	*-0.1*	*-0.2*	*-0.2*	*-0.3*	*-0.3*	*2.9*	*8.1*
	L2U2-D	*-0.9*	*-1.8*	*-2.7*	*-3.6*	*-1.5*	*4.4*	*2.7*
	U1L2-E	*1.4*	*2.7*	*4.3*	*5.7*	*6.7*	*4.5*	*-2.0*

Table E.9. Measured axial forces for the northbound controlled loading scenarios.

		Axial Force (kN)						
Trial	Member	7	6	5	4	3	2	1
Averaged Southbound Static	LOL1-B	11.3	7.3	4.2	1.8	0.3	-0.4	-0.1
	L0L1-Ca	8.9	5.6	3.4	1.7	0.6	0.2	0.5
	L1L2-Ca	11.0	6.3	3.0	0.8	-0.3	-0.7	0.0
	L2L3-Ca	7.9	20.3	14.2	8.8	5.3	2.5	1.2
	L0L1-Cb	8.0	7.0	4.5	2.7	1.7	1.0	0.5
	L2L3-Cb	6.5	13.0	10.7	6.8	3.9	1.9	0.6
	L0U1-Aa	-25.9	-23.1	-18.6	-14.6	-10.6	-5.9	-1.3
	L0U1-Ab	-31.6	-28.7	-22.8	-18.5	-13.6	-7.8	-2.7
	U2U3-Aa	-14.9	-30.5	-39.7	-32.2	-23.6	-14.5	-5.6
	U2U3-Ab	-7.2	-15.5	-21.2	-16.9	-11.9	-7.8	-2.7
	L1U1-D	21.5	0.3	-1.1	-1.0	-1.0	-0.9	-1.0
	L2U2-D	10.3	11.8	-8.3	-8.1	-6.0	-3.8	-1.8
	U1L2-E	-5.1	17.2	15.2	12.0	9.0	5.8	2.7
Averaged Southbound 20 km/hr	LOL1-B	12.3	10.4	6.6	4.4	2.8	1.9	2.1
	L0L1-Ca	9.3	7.6	4.7	3.1	2.0	1.3	1.6
	L1L2-Ca	11.5	9.1	4.8	2.7	1.3	0.7	1.2
	L2L3-Ca	7.8	19.7	16.0	10.0	6.3	3.6	2.4
	L0L1-Cb	8.5	8.5	5.9	4.2	3.1	2.6	2.3
	L2L3-Cb	6.2	13.7	11.9	8.2	5.2	2.8	1.5
	L0U1-Aa	-23.4	-24.7	-20.2	-16.2	-11.9	-7.5	-3.2
	L0U1-Ab	-28.8	-30.8	-25.3	-20.1	-14.9	-9.9	-4.6
	U2U3-Aa	-13.4	-29.0	-40.4	-34.0	-25.2	-16.9	-8.5
	U2U3-Ab	-7.3	-16.0	-22.3	-19.4	-14.2	-9.3	-4.6
	L1U1-D	19.9	3.8	-0.3	0.0	0.1	0.2	0.1
	L2U2-D	7.9	12.4	-6.6	-8.0	-5.6	-3.7	-1.6
	U1L2-E	-5.8	13.7	14.9	11.7	8.7	5.8	2.9
Averaged Southbound 30 km/hr	LOL1-B	11.2	10.9	6.5	4.1	2.5	1.3	1.7
	L0L1-Ca	8.3	7.8	4.6	2.8	1.7	0.8	1.2
	L1L2-Ca	10.3	10.0	4.9	2.6	1.3	0.5	1.0
	L2L3-Ca	6.2	18.7	16.7	9.9	6.1	3.4	1.8
	L0L1-Cb	7.8	8.8	5.9	4.1	2.9	2.4	2.0
	L2L3-Cb	5.3	13.2	12.3	8.5	5.4	3.0	1.7
	L0U1-Aa	-25.8	-20.5	-16.1	-12.3	-8.4	-3.7	-0.2

	L0U1-Ab	-32.3	-26.4	-20.7	-15.7	-10.8	-5.4	-0.7
	U2U3-Aa	-27.5	-40.1	-34.5	-25.7	-17.6	-8.3	-0.7
	U2U3-Ab	-15.3	-21.7	-19.3	-14.9	-9.8	-4.9	-0.5
	L1U1-D	6.3	-0.4	0.0	0.1	0.1	0.1	0.1
	L2U2-D	13.4	-4.8	-8.4	-5.9	-3.9	-1.9	-0.1
	U1L2-E	11.7	15.4	11.7	8.7	5.8	2.6	0.1
Averaged Southbound 50 km/hr	LOL1-B	10.8	9.9	6.0	3.7	2.8	1.4	1.9
	L0L1-Ca	8.1	7.0	4.2	2.5	1.8	0.9	1.4
	L1L2-Ca	10.2	8.6	4.5	2.5	1.3	0.4	1.0
	L2L3-Ca	6.9	17.6	15.1	9.6	5.7	2.4	1.6
	L0L1-Cb	8.7	8.4	5.6	4.1	2.4	1.8	1.9
	L2L3-Cb	6.2	14.4	12.1	8.0	5.6	2.7	2.1
	L0U1-Aa	-20.1	-22.6	-18.6	-15.3	-11.7	-7.2	-4.2
	L0U1-Ab	-25.2	-28.3	-23.8	-19.8	-14.7	-9.1	-4.9
	U2U3-Aa	-12.2	-26.7	-37.7	-32.8	-24.9	-15.8	-9.1
	U2U3-Ab	-8.1	-17.6	-23.2	-20.5	-15.8	-9.4	-5.8
	L1U1-D	17.3	4.4	-0.3	0.1	0.2	0.1	0.1
	L2U2-D	7.0	11.2	-5.5	-7.9	-5.6	-3.5	-1.8
	U1L2-E	-5.1	11.6	13.9	10.8	8.0	4.9	2.7

Table E.10. Measured axial forces for the southbound controlled loading scenarios.

		Axial Force (kN)						
Trial	Member	7	6	5	4	3	2	1
Averaged Southbound Static	LOL1-B	-0.6	-0.1	0.9	2.3	4.0	6.5	5.9
	L0L1-Ca	-0.1	0.2	0.7	1.6	2.8	4.7	4.5
	L1L2-Ca	-0.6	-0.2	0.8	2.1	3.7	6.6	6.8
	L2L3-Ca	0.2	1.7	3.9	6.6	9.6	10.7	4.2
	L0L1-Cb	-0.3	-0.1	0.9	2.7	5.3	9.9	11.3
	L2L3-Cb	0.3	2.4	5.8	11.1	18.7	21.7	5.6
	L0U1-Aa	-3.2	-4.7	-5.7	-7.7	-9.3	-11.3	-9.3
	L0U1-Ab	-2.1	-3.8	-6.1	-9.0	-10.6	-13.2	-10.8
	U2U3-Aa	-4.6	-9.1	-13.7	-18.5	-19.5	-12.9	-4.8
	U2U3-Ab	-11.1	-20.6	-28.7	-37.5	-42.4	-27.0	-9.9
	L1U1-D	0.1	0.2	0.2	0.0	-0.1	2.7	8.4
	L2U2-D	-0.9	-1.8	-2.8	-3.8	-1.7	5.9	3.3
	U1L2-E	1.2	2.7	4.1	5.5	6.8	4.9	-3.1
Averaged Southbound 20 km/hr	LOL1-B	0.5	0.9	1.5	2.8	4.4	6.5	6.2
	L0L1-Ca	0.3	0.4	0.8	1.6	2.9	4.5	4.5
	L1L2-Ca	0.2	0.3	1.1	2.3	4.1	6.7	6.8
	L2L3-Ca	1.0	2.0	4.5	7.2	10.9	11.1	5.4
	L0L1-Cb	-0.1	-0.3	1.2	3.3	6.3	10.7	12.2
	L2L3-Cb	0.6	2.3	6.0	11.1	18.6	21.0	7.4
	L0U1-Aa	-1.7	-3.1	-5.0	-6.4	-8.8	-9.9	-7.9
	L0U1-Ab	-2.2	-4.3	-6.7	-8.4	-11.5	-13.6	-11.2
	U2U3-Aa	-4.0	-8.4	-13.5	-18.0	-19.9	-13.7	-5.9
	U2U3-Ab	-7.9	-16.9	-26.1	-35.2	-40.3	-26.9	-12.0
	L1U1-D	0.1	0.0	0.0	-0.1	-0.1	3.1	7.7

	L2U2-D	-0.9	-1.8	-2.9	-3.9	-1.6	5.1	3.3
	U1L2-E	1.3	2.9	4.4	5.8	7.4	5.0	-1.7
Averaged Southbound 30 km/hr	LOL1-B	0.7	1.0	1.4	2.6	4.1	6.1	6.9
	L0L1-Ca	0.5	0.6	0.8	1.6	2.8	4.3	5.1
	L1L2-Ca	0.4	0.4	0.9	2.1	3.6	6.1	7.5
	L2L3-Ca	0.9	1.9	3.7	6.5	9.4	10.8	6.2
	L0L1-Cb	-0.3	-0.6	0.5	2.5	5.0	9.2	12.9
	L2L3-Cb	0.7	2.1	5.3	10.3	16.9	22.7	9.9
	L0U1-Aa	-1.8	-3.3	-4.9	-6.5	-8.0	-9.8	-9.4
	L0U1-Ab	-2.0	-4.1	-6.2	-8.5	-10.5	-12.3	-12.5
	U2U3-Aa	-3.6	-8.3	-12.8	-17.7	-19.8	-14.2	-7.5
	U2U3-Ab	-7.6	-16.8	-25.4	-34.7	-42.0	-30.6	-15.6
	L1U1-D	-0.1	-0.1	-0.1	-0.2	-0.3	1.6	7.6
	L2U2-D	-0.9	-1.8	-2.8	-3.9	-2.8	4.1	3.7
	U1L2-E	1.0	2.4	3.8	5.4	6.9	5.7	-1.4
Averaged Southbound 50 km/hr	LOL1-B	-0.2	-0.2	1.1	2.4	3.7	6.0	5.8
	L0L1-Ca	-0.2	-0.3	0.6	1.6	2.5	4.1	4.3
	L1L2-Ca	-0.2	-0.2	0.7	1.9	3.6	6.1	6.3
	L2L3-Ca	0.8	2.0	4.2	6.9	10.0	10.4	4.2
	L0L1-Cb	-0.3	-0.6	0.4	2.0	5.3	9.9	11.4
	L2L3-Cb	0.2	1.7	5.6	10.6	18.0	21.5	6.9
	L0U1-Aa	-1.5	-3.1	-5.2	-6.8	-8.4	-10.0	-7.6
	L0U1-Ab	-2.0	-4.0	-6.2	-8.4	-10.1	-12.6	-9.9
	U2U3-Aa	-4.8	-9.2	-14.5	-19.1	-19.7	-13.5	-5.5
	U2U3-Ab	-9.2	-18.1	-27.0	-36.1	-41.2	-27.8	-12.4
	L1U1-D	-0.1	-0.2	-0.2	-0.3	-0.3	2.7	7.4
	L2U2-D	-1.1	-2.0	-3.1	-4.1	-1.7	5.1	3.1
	U1L2-E	1.5	3.0	4.6	6.1	7.2	4.9	-2.2